Mathematical Modelling of Droplet Evaporation

PhD Thesis

Feargus G. H. Schofield

Continuum Mechanics and Industrial Mathematics

Department of Mathematics and Statistics

University of Strathclyde, Glasgow

February 16, 2021

This thesis is the result of the author's original research. It has been composed by the author and has not been previously submitted for examination which has led to the award of a degree.

Abstract

This thesis concerns the theoretical modelling and analysis of sessile droplets of liquids as they evaporate in different modes of evaporation. The thesis focuses on diffusion-limited evaporation in which the diffusion of vapour in the surrounding atmosphere governs the evaporation rate of the droplet.

First, we investigate the combined influences of the initial contact angle and the substrate conductivity on droplet evaporation. In particular we highlight that for droplets with large contact angles the lifetime of the droplet does not vary strongly with either the mode of evaporation or the conductivity of the substrate.

Next, we investigate the evaporation of thin sessile droplets on thin substrates in two situations in which the influence of the thermal properties of the system is strong. Specifically, we obtain closed form asymptotic solutions for the evolution of the droplet when the substrate has a high thermal resistance relative to the droplet, and when the saturation concentration of the vapour depends strongly on temperature.

Finally, we develop a model for the evaporation of thin two-dimensional sessile droplets evaporating either singly or as a pair. We find that in large domains the lifetime of the droplet depends logarithmically on the size of the domain, and more weakly on the mode of evaporation and the separation between the droplets. In particular, we quantify the shielding effect that the droplets have on each other, and how it extends the lifetime of the droplets.

Contents

Acknowledgements

The writing of this thesis and completion of my PhD studies would not have been possible without the ongoing support and encouragement from my all of my close friends and colleagues. I am grateful for all of their help.

The following people had a profound impact not only on the completion of this work, but also my years spent completing it, and undoubtedly many years to come.

My primary and secondary supervisors Prof. Stephen Wilson and Dr David Pritchard, whose Monday morning meetings were always an opportunity to learn something new, and a welcome start to every week. Through these meetings I developed the drive and confidence to present and publish all of my hard work. I am especially thankful for their support and understanding when times were particularly difficult.

My secondary supervisors Prof. Khellil Sefiane and Dr Alexander Wray, whose many useful insights and suggestions were the foundations for much of my work.

My close friends Joseph, Russell and Craig. Working (and living) alongside these three made life at Strathclyde every bit more enjoyable, and I wish them all the best on their future studies and careers.

My family, who have always shown enthusiasm in my work, and supported me in anyway they can.

Chapter 1

Introduction

1.1 Evaporation of sessile droplets

A sessile droplet (or drop) is a small volume of liquid which rests on a substrate. The liquid makes contact with the substrate along a droplet-substrate interface. The liquid makes contact with the atmosphere along an atmosphere-droplet interface (the free surface of the droplet). The angle which the free surface of the droplet makes with the substrate is called the contact angle, and the curve at which the atmosphere, droplet and substrate meet is called the contact line. The physics of sessile droplets, for example, droplet spreading, impact, and evaporation, have been the subject of a vast number of scientific investigations (see, for example, the recent reviews [20, 27, 59, 74, 81, 113, 125]) due to their important role in many industrial applications, health and medicine, as well as being of fundamental scientific interest. This thesis concerns the theoretical modelling and analysis of sessile droplets of liquids as they evaporate in different modes of evaporation.

In this chapter we describe various physical mechanisms that control the evaporation of a sessile droplet. We also describe several areas of active research involving droplet evaporation. Finally, we outline the contents of the thesis. A comprehensive discussion of various models for droplet evaporation is given in chapter 2.

1.2 Mathematical modelling of droplet evaporation

Mathematical modelling of liquid evaporation dates back at least as far as Maxwell [86], who determined the diffusivity coefficient of vapour through an atmosphere using the lifetime of an evaporating liquid. Maxwell [86] observed that the evaporation of a liquid is governed by the distribution of vapour in the atmosphere. In general, the evaporative flux depends on both the rate at which the liquid vaporises on the free surface of the liquid and the rate at which the vapour is transported away from the free surface. However, if the liquid vaporises much faster than the vapour can be transported away from the free surface then the surface will become saturated with vapour. In a quiescent atmosphere the difference between the high saturation concentration and the low ambient vapour concentration drives a diffusive flux of vapour away from the liquid. Since the evaporation rate is limited by the diffusion of vapour in the atmosphere, models built on the work of Maxwell [86] are called diffusion-limited models.

Building on the work of Maxwell, Picknett and Bexon [102] obtained theoretical approximate expressions for the evolution, and thus lifetimes, of evaporating droplets for a range of initial contact angles. Picknett and Bexon [102] compared their approximate expressions with the experimental results of methyl acetoacetate evaporating on a polytetrafluoroethylene (PTFE) substrate. They found at worst a 19.7% difference between the theoretical and experimental lifetimes. The model developed by Picknett and Bexon [102] assumes a constant vapour saturation concentration, but in practice this concentration can depend on the temperature of the free surface of the droplet, which varies in both space and time. Additionally, their model assumes a spherical-cap-shaped droplet, whereas their experimental droplets were not perfectly spherically shaped due to the effect of gravity. Picknett and Bexon [102] attribute the difference in the theoretical and experimental lifetime predictions to these two modelling assumptions. We discuss conditions in which droplets are approximately spherical in section 2.2.3 and conditions in which the vapour saturation concentration depends on the temperature of the free surface of the droplet in section 2.3.

Following Picknett and Bexon [102], Deegan *et al.* [37, 38, 39], Popov [105], Popov and Witten [106] and Stauber *et al.* [143, 144, 145] obtained exact expressions for the evolution and lifetime of an evaporating droplet using the exact solution to the equivalent problem in potential theory first reported by Lebedev [75, pp. 221-224]. The work of Deegan *et al.* [38] initiated an explosion of theoretical investigations into droplet evaporation, with Deegan *et al.* [38] receiving over 5211 citations according to Google Scholar as of April 2020. We discuss the evaporation of droplets of nanoparticle suspensions in more detail in section 1.7.

For situations in which the diffusion of vapour is not the governing mechanism for droplet evaporation, so-called "non-equilibrium models" are appropriate. We describe in brief a non-equilibrium model for droplet evaporation in section 2.7.

1.3 The effects of thermal properties on droplet evaporation

As highlighted by Picknett and Bexon [102], when a droplet evaporates the total heat energy decreases as the liquid vaporises. Therefore, there have been a considerable number of experimental and theoretical investigations into thermal effects during droplet evaporation. Hu and Larson [66] and Ristenpart *et al.* [112] both used the diffusion-limited model for evaporation to determine the temperature of the droplet, and hence study thermally-induced Marangoni, *i.e.* flow induced by large surface tension gradients on the free surface of the droplet.

While studying the evaporation of thin liquid films, Sultan *et al.* [147] noted that the saturation concentration of a vapour in the atmosphere is, in general, a function of the temperature of the free surface. Following Sultan *et al.* [147], Dunn *et al.* [50, 51, 52] and Sefiane *et al.* [120, 121] developed a diffusion-limited thermally-coupled model, hereafter refered to as "the Dunn model", for droplet evaporation by using an expression for saturation concentration which is a polynomial in temperature. However, these authors incorrectly assumed that the relatively low thermal conductivity of air produces

an isothermal atmosphere. Ait Saada *et al.* [3, 4, 5] and Lopes *et al.* [83] present a thermally-coupled model, hereafter referred to as "*the* thermally-coupled model", which uses the same polynomial expression for saturation concentration as that used by Dunn *et al.* [50], but also allows for a non-uniform atmospheric temperature. Singh *et al.* [133] used a variant of the thermally-coupled model which uses a different expression for saturation concentration which is exponential in temperature. All of these authors found that, in general, the lifetime of a droplet evaporating on a highly insulating substrate is longer than that of a droplet evaporating on a highly conducting substrate. Using the thermally-coupled model, Nguyen *et al.* [95] obtained expressions for lifetimes of droplets on an infinitely conducting substrate.

We give a full description of the Dunn model presented by Dunn *et al.* [50] and the thermally-coupled model presented by Ait Saada *et al.* [3], in chapter 2. Using the thermally-coupled model we obtain new solutions for the evolution, and hence lifetime, of droplets both numerically in chapter 3 and analytically in chapter 4.

1.4 Modes of evaporation

As a droplet evaporates, its volume reduces and so the contact radius $\hat{R} = \hat{R}(\hat{t})$ and/or the contact angle $\hat{\theta} = \hat{\theta}(\hat{t})$ must change. The manner in which the geometry of the droplet changes as it evaporates is called the mode of evaporation. It is necessary to understand the various modes of evaporation in order to determine the lifetime of a droplet. Picknett and Bexon [102] identified two "extreme" modes of evaporation for an axisymmetric droplet, namely the constant contact radius (CR) mode, and the constant contact angle (CA) mode. In the CR mode the contact radius of the droplet is fixed, $\hat{R} \equiv \hat{R}(0)$, and the contact angle $\hat{\theta}$ decreases from $\hat{\theta}(0)$ to 0. Conversely, in the CA mode the contact angle is fixed, $\hat{\theta} \equiv \hat{\theta}(0)$, and the contact radius of the droplet $\hat{R}$ decreases from $\hat{R}(0)$ to 0. Picknett and Bexon [102] found that the lifetime of the droplet depended on both the initial contact angle of the droplet and the mode in which the droplet evaporated. Table 1.1 provides many examples of experimental

investigations into droplets evaporating in the CR and CA modes in the contexts of thermal dynamics [21, 136, 149, 155], wetting dynamics [23, 130, 131, 135], evaporation rates [24, 31, 33, 55, 70, 107, 129], and pattern formation [26, 80, 97].

Nguyen and Nguyen [93, 94] described a compound mode of evaporation for axisymmetric droplets, namely the stick-slide (SS) mode, when investigating nano-particle effects on droplet lifetimes. In the SS mode the droplet initially evaporates in a CR phase with a fixed contact radius $\hat{R} \equiv \hat{R}(0)$ and a contact angle $\hat{\theta}$ that decreases from $\hat{\theta}(0)$ to a critical contact angle $\hat{\theta}^*$ $(0 < \hat{\theta}^* < \hat{\theta}(0))$, after which it evaporates in a CA phase with fixed contact angle $\hat{\theta} = \hat{\theta}^*$ and a contact radius $\hat{R}$ that decreases from $\hat{R}(0)$ to 0. Table 1.1 provides many examples of investigations into droplets evaporating in the SS mode in the contexts of wetting dynamics [13, 54, 103, 130, 131], pattern formation [22, 77, 80, 152, 154], evaporation rates [32, 34, 40, 47, 57, 58, 69, 76, 87, 92, 104, 124, 140, 141], and thermal dynamics [122, 123, 168].

Stauber *et al.* [143] gave an analysis of the CR, CA and SS modes of evaporation and found evaporation rates and lifetimes for droplets in each of these modes. Furthermore, Stauber [142, pp. 95-99] described a fourth mode of evaporation for axisymmetric droplets, namely the stick-jump (SJ) mode. In the SJ mode the droplet initially evaporates in a CR phase with a fixed contact radius $\hat{R} \equiv \hat{R}(0)$ and a contact angle $\hat{\theta}$ that decreases from $\hat{\theta}(0)$ to a critical angle $\hat{\theta}_{\min}$ $(0 < \hat{\theta}_{\min} < \hat{\theta}(0))$, at which moment the contact angle jumps instantaneously from $\hat{\theta}_{\min}$ to a second critical angle $\hat{\theta}_{\max}$ $(\hat{\theta}_{\max} > \hat{\theta}_{\min})$ and the contact radius jumps instantaneously to a new value $\hat{R} = \hat{R}_1$. The process of a CR phase followed by an instantaneous jump phase then repeats an infinite number of times until the droplet has finally evaporated. Table 1.1 provides many examples of investigations into droplets evaporating in the SJ mode in the contexts of pattern formation [2, 17, 18, 19, 78, 91, 98, 132], wetting dynamics [25, 71, 84, 96], thermal dynamics [110], and evaporation rates [88]. Figure 1.1 (reprinted with permission from Debuisson *et al.* [36]) shows experimental measurements of the contact angle θ and contact radius R of a water droplet as it evaporates in the SJ mode.

Mode of evaporation	Experimental investigations
CR and CA	[21, 23, 24, 26, 31, 33, 55, 70, 80, 97, 102, 103, 104, 107, 129, 130, 131, 135, 136, 140, 149, 155]
SS	[13, 22, 32, 34, 40, 47, 54, 57, 58, 69, 76, 77, 80, 87, 92, 93, 103, 104, 122, 123, 124, 130, 131, 140, 141, 152, 154, 168]
SJ	[2, 17, 18, 19, 25, 71, 78, 84, 88, 91, 96, 98, 110, 132]

Table 1.1: Examples of experimental investigations into droplets evaporating in the CR, CA, SS and SJ modes described in this section.

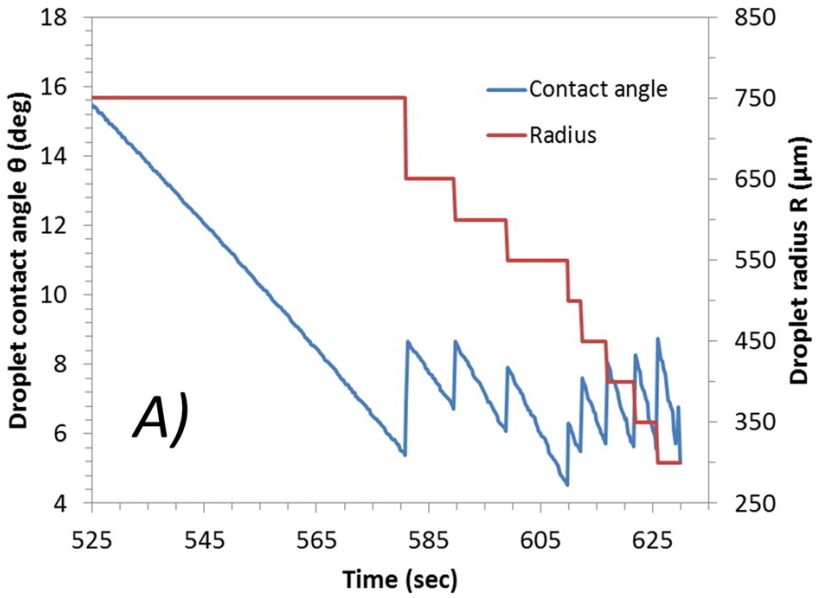

Figure 1.1: Experimental measurements of the contact angle θ and contact radius R of a water droplet as it evaporates in the SJ mode. Reprinted with permission from Debuisson *et al.* [36]. Copyright 2016 American Chemical Society.

1.5 The effects of neighbouring droplets on droplet evaporation

For a droplet evaporating in isolation, the only source of vapour is the droplet itself. However, droplets rarely evaporate in isolation. In particular, multiple droplets appear in many industrial applications such as ink-jet printing [35], fuel injection [114] and spray cooling [62]. Because of this, there is growing interest in investigating the influence that neighbouring droplets have on each other when evaporating in close proximity. In particular, there have been a number of experimental, numerical and analytical investigations into the so-called "shielding effect", in which neighbouring droplets increase the vapour concentration in the atmosphere between the droplets.

Early experimental work by Schäfle *et al.* [115] demonstrated that droplets evaporating in an array interact with each other through their vapour field, and hence influence the evaporation rate of their neighbours. Sokuler *et al.* [139] numerically and experimentally investigated the evaporation of droplets deposited in both 1D and 2D arrays. They observed that isolated droplets evaporated faster than droplets evaporating in an array. Sokuler *et al.* [139] observed experimentally that the vapour surrounding an isolated droplet maintains ambient conditions beyond a (finite) typical distance from the droplet. They also highlighted that the influence of neighbouring identical droplets on evaporation was negligible when the droplets were separated by more than that typical distance.

Recent experimental work by Shaikeea *et al.* [126, 127, 128] also highlights the shielding effect. Figure 1.2 (reprinted with permission from Shaikeea and Basu [128]) shows a side view of two water droplets evaporating on a PDMS substrate. Also shown is a sketch which illustrates the increased vapour concentration between the droplets, *i.e.* the shielding effect.

Castanet *et al.* [29] experimentally and numerically investigated the influence of droplet spacing on the evaporation rate and temperature of a uniform line of sessile fuel droplets, namely, isohexane, ethanol, n-decane and n-dodecane. Castanet *et al.* [29]

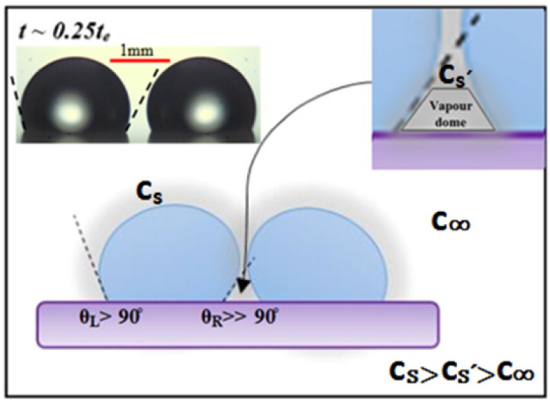

Figure 1.2: Side view of two water droplets evaporating on a polydimethylsiloxane (PDMS) substrate. Also shown is a sketch which illustrates the increased vapour concentration between the droplets, *i.e.* the shielding effect. Reprinted with permission from Shaikeea and Basu [128]. Copyright 2016 American Chemical Society

found that greater spacing between droplets leads to shorter droplet lifetimes. Carrier *et al.* [28] developed a rudimentary model for obtaining the lifetimes of non-uniform droplet clusters produced by spraying liquid onto a substrate. Hu *et al.* [67] theoretically investigated the deposition patterns produced by two neighbouring droplets containing suspended nanoparticles and found that the majority of the deposited mass is found near the point on the contact line which is furthest from the neighbouring droplet. Hu *et al.* [67] concluded that, due to the presence of a neighbouring droplet, the evaporative flux is most suppressed near the point on the contact line which is closest to the neighbouring droplet, and hence the suspended nanoparticles are convected towards the point with the highest evaporative flux (*i.e.* the point furthest from the neighbouring droplet).

Hatte *et al.* [64] experimentally investigated the evaporation of a line of uniformly spaced sessile water droplets. Hatte *et al.* [64] also found that greater spacing between the droplets leads to shorter droplet lifetimes, and that for sufficiently spaced droplets, the lifetime approaches that of a droplet evaporating in isolation.

Very recently, Wray *et al.* [161] obtained exact expressions for flux profiles, as well as evolutions and lifetimes, for multiple evaporating droplets. The approach of Wray *et al.* [161] captures the shielding effect, and, in particular, shows that the evaporative

flux from a pair of droplets is greatest at the point on the contact line that is furthest from the neighbouring evaporating droplet.

Analogous phenomena to the shielding effect have been studied in other physical contexts. Greenwood [61] examined the interaction of large numbers of microcontacts in electric contact theory, treating them as independent at leading order, and introducing an interaction term at higher order. Similar approaches have since been applied to elastic punches [60] and flow through pores [56], and have been put on a more rigorous asymptotic basis [14, 15, 16]. All these studies essentially considered problems equivalent to the evaporation of circular droplets in three dimensions.

1.6 Droplet composition

Although this thesis only concerns single component droplets, *e.g.* pure water or pure methanol, in general, droplets can consist of multiple components. Recent work has shown that the chemical makeup of a droplet influences its evaporation rate. Tan *et al.* [150, 151] experimentally and numerically investigated the evaporation of a droplet consisting of water, ethanol and anise oil. They found that this droplet evaporates in four distinct phases. During the first phase the ethanol quickly evaporates away from the droplet, resulting in strong Marangoni flows within the droplet. In the second phase the anise oil begins to nucleate into microdroplets within the droplet. In the third phase the anise oil microdroplets merge into a ring near the contact line of the droplet. During the second and third phases the water is continuously evaporating away from the droplet. Finally, in the fourth phase the water has completely evaporated, leaving behind a droplet of pure anise oil. This work shows that, throughout the evaporation process, a multicomponent droplet can experience strong internal flows, as well as distortions to the shape of its free surface. The work by Tan *et al.* [150, 151], and later Diddens *et al.* [41, 42, 43] and Li *et al.* [79] has shown that the evaporation of multicomponent droplets is far more complex than those of single component droplets.

1.7 The coffee-stain effect

Understanding droplet evaporation is an important part of understanding many industrial processes, for example, ink-jet printing and surface patterning [22, 80], as well as drug delivery systems [109] and the detection of hazardous chemicals [63]. For all of these processes it is important to know both the evolution and lifetime of the droplet, and the structure of any deposit of suspended particles left after the liquid has evaporated. When a droplet of liquid containing suspended particles is left to evaporate, the distribution of deposit left behind is often highly non-uniform. The deposition of particles in patterned formations is often refereed to as the "coffee-stain effect". One particular application of the coffee-stain effect in industry is the ink-jet printing of self-assembling electronics [46, 166].

Deegan *et al.* [38] pioneered the mathematical and experimental investigation into the coffee-stain effect by relating the movement of suspended particles within a droplet to the profile of the evaporative mass flux from the free surface of the droplet. In subsequent years there have been further investigations into the effects of many different mechanisms on deposition patterns such as: particle size [37], evaporation suppression [39, 67], electrostatic effects [160], and evaporative modes [162]. The contact angle plays a significant role in the coffee-stain effect [37, 38, 39, 105], as does the initial shape of the droplet-substrate interface [106, 148, 166].

Although this thesis is not directly concerned with the coffee-stain effect, Deegan *et al.* [38] have shown that to understand the coffee-stain effect it is necessary to understand the evaporation mechanisms of the droplet.

Dinh *et al.* [46] described a method of ink-jet printing carbon electrodes in which a line of liquid containing suspended carbon nanoparticles evaporates and leaves a deposit of carbon at the edge of the line. Their process involved depositing $100-140$ multi-walled carbon nanotube (MWCNT)-laden water droplets with radius ~ 0.1 mm in a straight line. The spacing between the droplets ranged from $0.06-0.11$ mm. The resulting deposits were liquid lines ~ 0.1 mm thick and ~ 10 mm long. Dinh *et al.* [46] found

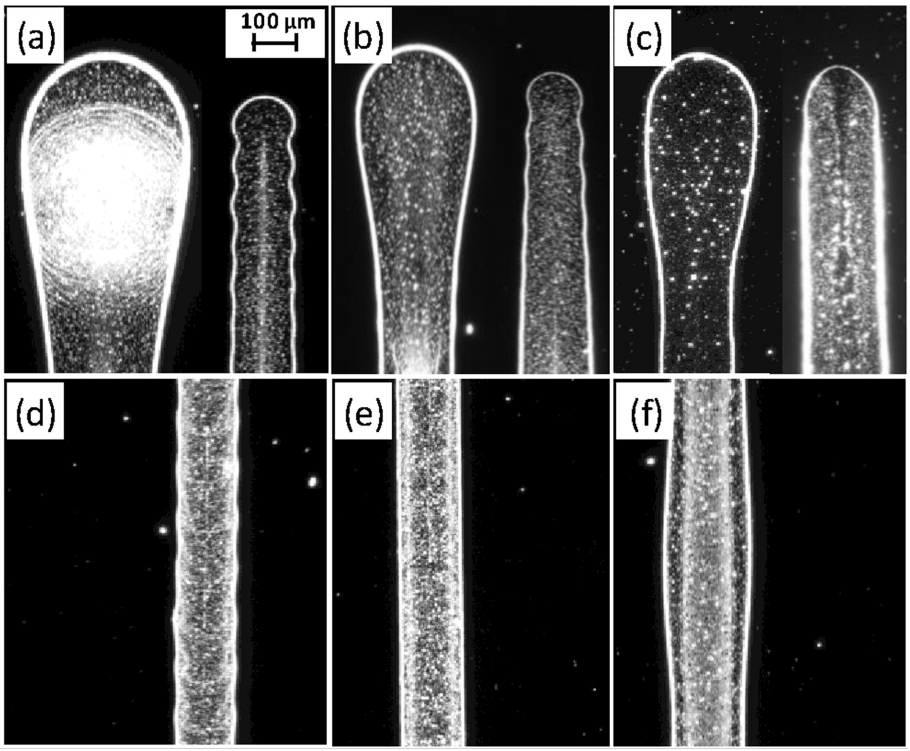

Figure 1.3: Top down photographs of (MWCNT)-laden water liquid lines. (a–c) show the head of the liquid line (left) and the tail of the liquid line (right) for droplets printed with a spacing of 90 μm onto a silicon substrate with temperature 35 °C, 50 °C and 60 °C, respectively. (d–f) show the middle part of a liquid line for droplets printed with a spacing of 110 μm, 90 μm and 60 μm, respectively onto a silicon substrate with temperature 60 °C. Reprinted with permission from Dinh *et al.* [46]. Copyright 2016 Elsevier.

that a spacing of 90 μm between individual droplets produced a liquid line that was, for the most part, uniform along its length. We shall hereafter refer to such uniform liquid lines as 2D droplets.

Figure 1.3, reprinted with permission from Dinh *et al.* [46], shows the various liquid lines produced by Dinh *et al.* [46]. Figures 1.3(a–c) show top down photographs of the heads (left) and the tails (right) for droplets printed with a spacing of 90 μm onto a silicon substrate with temperature 35 °C, 50 °C and 60 °C, respectively. Figures 1.3(d–f) show the middle part of a liquid line for droplets printed with a spacing of 110 μm, 90 μm and 60 μm, respectively onto a silicon substrate with temperature 60 °C. In particular, figure 1.3(e) shows a liquid line that is uniform along its length.

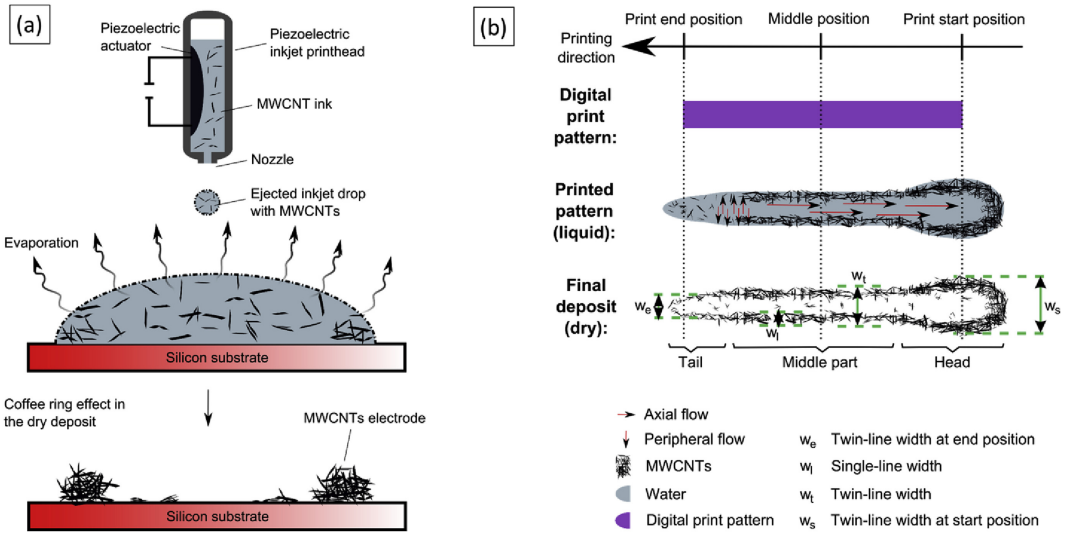

Figure 1.4: (a) Sketch of the cross-section of a 2D droplet of MWCNT-laden water being deposited onto a silicon substrate. The evaporation driven coffee-ring effect causes the MWCNTs to self-assemble into carbon electrodes. (b) Sketch of the top down view of a liquid line of MWCNT-laden water before and after completed evaporation. Reprinted with permission from Dinh *et al.* [46]. Copyright 2016 Elsevier.

Figure 1.4(a), reprinted with permission from Dinh *et al.* [46], shows a sketch of the cross-section of a 2D droplet of MWCNT-laden water being deposited onto a silicon substrate. The evaporation driven coffee-ring effect causes the MWCNTs to self-assemble into carbon electrodes. Figure 1.4(b) shows the sketch of the top down view of an liquid line of MWCNT-laden water before and after total evaporation. In particular, figure 1.4(b) divides the liquid line into a rounded head and tail and a straight middle part. When we consider 2D droplets in chapter 5 we shall only consider the straight middle part.

Following from Deegan *et al.* [38], Yarin *et al.* [166] developed a mathematical model to describe the evaporation rate, and hence the coffee-stain effect, of an evaporating 2D droplet. Yarin *et al.* [166] also compared their results with the particle deposits left by an evaporating 2D droplet of gold-nanoparticle-laden toluene solvent. Petsi and Burganos [99] also give a solution for deposits left by an evaporating 2D droplet for an arbitrary expression for the evaporative flux.

1.8 Mathematically similar problems

The mathematical models which describe the shape of the free surface of a droplet and its rate of evaporation are similar to models used to describe the dissolution of liquid droplets and gaseous bubbles (see review by Lohse and Zhang [81]). In particular, a number of authors have remarked on the mathematical similarities between liquid droplet evaporation into a gaseous atmosphere (as discussed in this thesis) and (*i*) gaseous bubbles dissolving into a surrounding liquid [48, 82, 90, 170] and (*ii*) liquid droplets dissolving into a surrounding liquid [44, 45, 72, 111, 171]. Moreover, the problems described in [48, 72, 111, 170] are mathematically equivalent to problems concerning multiple droplet evaporation, and the problems described in [44, 111, 171] are mathematically equivalent to problems concerning various modes of droplet evaporation.

Authors have also considered a number of other mathematically similar problems, including elastostatics [134], electrostatics [68], thermostatics [85], and hydrodynamics [146].

A range of mathematical techniques can be deployed to solve such problems [49, 134]; including separation of variables [158], orthogonal polynomial expansions [53], Fourier or Hankel transforms [156, 163, 164], and Green's functions [165].

In two dimensions, additional techniques become available, notably conformal mapping [73, 85]. This makes two-dimensional analogues of droplet evaporation problems appealing from the modeller's point of view: although two-dimensional problems may be somewhat artificial, their greater tractability allows more thorough analysis to be carried out.

1.9 Thesis overview

This thesis is concerned with various aspects of the evolution, and hence the lifetimes, of evaporating sessile droplets in various modes of evaporation.

In chapter 2 we give an account of various models for the evaporation of a sessile droplet on a horizontal substrate. We give a full derivation of the thermally-coupled diffusion-limited models for evaporation used by, for example, Ait Saada *et al.* [5]. We also give a statement of the model used by Dunn *et al.* [51] and explain the key differences between the thermally-coupled model and the Dunn model.

In chapter 3 we consider the thermally-coupled evaporation of an axisymmetric droplet using the finite element analysis package COMSOL Multiphysics [1]. We first validate our solutions against the solutions found previously by Dunn *et al.* [51], Ait Saada *et al.* [5] and Stauber *et al.* [143]. We then find the evaporation rates and lifetimes for axisymmetric water droplets with various initial contact angles evaporating on substrates of various thermal conductivities in the CR and CA modes of evaporation.

In chapter 4 we build on the work in chapter 3 and restrict our investigation to thin droplets evaporating on thin substrates, allowing us to obtain analytical expressions for the vapour and temperature fields produced by an evaporating droplet. In particular, we obtain the evaporation rate, and hence lifetime, of a droplet evaporating in the CR, CA, SS and SJ modes of evaporation.

In chapter 5 we consider the evaporation of thin two-dimensional sessile droplets either singly or in a pair. We use a conformal-mapping technique to obtain the vapour concentrations, and hence obtain closed-form solutions for the evolutions and the lifetimes of the droplets in the CR, CA and SS modes of evaporation.

In chapter 6 we summarise the results obtained, draw conclusions, and suggest possible directions for future work.

1.10 Publications and presentations

Aspects of the work in chapter 3 have been published as an extended abstract (Schofield *et al.* [116]) in the Proceedings of the 16th UK Heat Transfer Conference, September 2019, Nottingham, as well as being presented as an oral presentation by my primary

supervisor Prof. Stephen K. Wilson at this meeting and by myself at Droplets 2019, September 2019, Durham.

The work in chapter 4 has been published in the Journal of Fluid Mechanics (Schofield *et al.* [117]) and as an extended abstract (Wilson *et al.* [159]) in the Proceedings of the 15th UK Heat Transfer Conference, September 2017, London, as well as presented as an oral presentation by Prof. Stephen K. Wilson at this meeting. This work has also been presented by me at the Institute of Physics Printing and Graphics Society "Printing for the Future" conference, January 2018, Nottingham; the 60th British Applied Mathematics Colloquium, March 2018, St Andrews; the 31st Scottish Fluid Mechanics Meeting, May 2018, Aberdeen; the UK Fluids Network Fluid Mechanics of Cleaning and Decontamination Special Interest Group Summer 2018 Conference, August 2018, Cambridge; the UK Fluids Conference 2018, September 2018, Manchester; the 12th European Fluid Mechanics Conference, September 2018, Vienna; and a Continuum Mechanics and Industrial Mathematics Research Group Seminar within the Department of Mathematics and Statistics at the University of Strathclyde, January 2019.

The work in chapter 5 has been recently published in the Journal of Engineering Mathematics (Schofield *et al.* [118]), as well as presented by me at the 61st British Applied Mathematics Colloquium, April 2019, Bath, and the 32nd Scottish Fluid Mechanics Meeting, May 2019, Dundee and by Prof. Stephen K. Wilson as an oral presentation at Droplets 2019, September 2019, Durham.

Chapter 2

Theoretical Models for Droplet Evaporation

2.1 Introduction

In this chapter we give a mathematical description of a sessile droplet, and various models for its evaporation on a horizontal substrate. When choosing an appropriate model it is important to consider the dominant physical mechanisms which govern the evaporation of the droplet. Evaporation models are usually categorised as either of the following.

- Diffusion-limited (or two-sided) models, in which the evaporation is controlled by the diffusion of vapour molecules in the atmosphere. Diffusion-limited models are generally appropriate for situations in which the droplet evaporates in an equilibrated state.
- Non-equilibrium (or one-sided) models, in which evaporation is controlled by non-equilibrated thermal effects acting at the free surface of the droplet. Non-equilibrium models are generally appropriate for situations in which the droplet is heated.

As the work in this thesis concerns only diffusion-limited models of evaporation, we will

Parameter	Water [51]	Methanol [51]	Acetone [51]	Toluene [166]
$\hat{\rho}$ [kg m^{-3}]	9.98×10^2	7.90×10^2	7.88×10^2	8.67×10^2
$\hat{\mu}$ [kg m^{-1} s^{-1}]	9.46×10^{-4}	5.74×10^{-4}	3.15×10^{-4}	5.8×10^{-4}
$\hat{D}$ [m^2 s^{-1}]	2.44×10^{-5}	1.5×10^{-5}	1.06×10^{-5}	2.1×10^{-5}
$\hat{\sigma}$ [kg s^2]	7.25×10^{-2}	2.23×10^{-2}	2.38×10^{-2}	2.84×10^{-2}
$\hat{k}$ [kg m s^{-3} K^{-1}]	6.04×10^{-1}	2.03×10^{-1}	1.61×10^{-1}	–
$\hat{c}_\mathrm{p}$ [m^2 s^{-2} K^{-1}]	4.18×10^3	2.53×10^3	2.17×10^3	–
$\hat{\alpha}$ [m^2 s^{-1}]	1.44×10^{-7}	1×10^{-7}	9.41×10^{-8}	–
$\hat{L}$ [m]	1×10^{-3}	1×10^{-3}	1×10^{-3}	1×10^{-3}
$\hat{V}_0$ [m^3]	1×10^{-9}	1×10^{-9}	1×10^{-9}	1×10^{-9}
$\hat{c}_\mathrm{sat}(\hat{T}_\infty)$ [kg m^{-3}]	1.194×10^{-2}	1.86×10^{-1}	6.37×10^{-1}	1.77×10^{-1}
$\hat{c}_\infty$ [kg m^{-3}]	7.76×10^{-3}	0	0	0
$\hat{\tau}$ [s]	1.073×10^3	86	35	1.57×10^2

Table 2.1: Typical physical properties of various liquids as quoted by Dunn *et al.* [51] and Yarin *et al.* [166]. Also shown are lengthscales $\hat{L}$ and initial volumes $\hat{V}_0$ typical for the droplets described by Dunn *et al.* [51] and Yarin *et al.* [166], and the corresponding evaporative timescales $\hat{\tau}$ of the obtained using (2.1). Dashes indicate values not given in the corresponding source.

now give a complete derivation of these models. We will also give a brief description of non-equilibrium models in section 2.7.

2.2 Mathematical model of an evaporating droplet

We will now give a mathematical model of an evaporating sessile droplet. Using carets to denote dimensional quantities and unscaled angles, we consider a droplet of liquid with known constant density $\hat{\rho}$, surface tension $\hat{\sigma}$, viscosity $\hat{\mu}$, specific heat capacity $\hat{c}_\mathrm{p}$, thermal conductivity $\hat{k}$, thermal diffusivity $\hat{\alpha} = \hat{k}/\hat{\rho}\hat{c}_\mathrm{p}$, latent heat of vaporisation $\hat{\mathcal{L}}$, and with an unknown free surface $\hat{h}$ and temperature $\hat{T}$. The droplet is immersed within an atmosphere with constant pressure $\hat{p}^\mathrm{a}$, density $\hat{\rho}^\mathrm{a}$, specific heat capacity $\hat{c}^\mathrm{a}_\mathrm{p}$, thermal conductivity $\hat{k}^\mathrm{a}$, and thermal diffusivity $\hat{\alpha}^\mathrm{a} = \hat{k}^\mathrm{a}/\hat{\rho}^\mathrm{a}\hat{c}^\mathrm{a}_\mathrm{p}$, and with unknown vapour concentration $\hat{c}$ and temperature $\hat{T}^\mathrm{a}$. Table 2.1 gives typical physical properties of various liquids as quoted by Dunn *et al.* [51] and Yarin *et al.* [166]. Table 2.1 also gives the typical lengthscales $\hat{L}$ and timescales $\hat{\tau}$ of the droplets described by Dunn *et*

Parameter	Aluminium [51]	PTFE [51]	Aerogel [157]
$\hat{\rho}^{\mathrm{s}}$ [kg m^{-3}]	2.71×10^{3}	2.22×10^{3}	–
$\hat{c}_{\mathrm{p}}^{\mathrm{s}}$ [m^{2} s^{-2} K^{-1}]	9.11×10^{2}	1.05×10^{3}	–
$\hat{k}^{\mathrm{s}}$ [kg m s^{-3} K^{-1}]	2.73×10^{2}	2.5×10^{-1}	–
$\hat{\alpha}^{\mathrm{s}}$ [m^{2} s^{-1}]	1.20×10^{-4}	1.08×10^{-7}	4×10^{-7}

Table 2.2: Typical physical properties of various substrates as quoted by Dunn *et al.* [51] and Wei *et al.* [157]. Dashes indicate values not given in the corresponding source.

al. [51] and Yarin *et al.* [166], where

$$\hat{\tau} = \frac{\hat{\rho}}{2\hat{D}(\hat{c}_{\mathrm{sat}}(\hat{T}_{\infty}) - \hat{c}_{\infty})} \left(\frac{3\hat{V}_0}{2\pi} \right)^{2/3} \tag{2.1}$$

is the characteristic timescale of diffusion-limited evaporation as discussed by, for example, Stauber *et al.* [143], and is hereafter referred to as the *basic* timescale.

2.2.1 Wetting

We suppose that the droplet is deposited onto a horizontal substrate of constant thickness $\hat{h}^{\mathrm{s}}$, density $\hat{\rho}^{\mathrm{s}}$, specific heat capacity $\hat{c}_{\mathrm{p}}^{\mathrm{s}}$, thermal conductivity $\hat{k}^{\mathrm{s}}$, and thermal conductivity $\hat{k}^{\mathrm{a}}$, thermal diffusivity $\hat{\alpha}^{\mathrm{s}} = \hat{k}^{\mathrm{s}}/\hat{\rho}^{\mathrm{s}}\hat{c}_{\mathrm{p}}^{\mathrm{s}}$, and unknown temperature $\hat{T}^{\mathrm{s}}$. Table 2.2 shows typical physical properties of various substrates as quoted by Dunn *et al.* [51] and Wei *et al.* [157].

Adhesive forces (forces between unlike molecules) between the substrate and the droplet deform the droplet to a quasi-equilibrium state with a contact angle between the substrate and the droplet $\hat{\theta}$ ($0 \leq \hat{\theta} \leq \pi$) by the process of wetting. The equilibrium contact angle of a droplet deposited onto an ideal substrate, *i.e.* a substrate that is perfectly smooth, chemically homogeneous, rigid, impermeable and insoluble, is described by the Young–Dupré equation, [167]

$$\hat{\sigma} \cos \hat{\theta} = \hat{\sigma}_{\mathrm{sa}} - \hat{\sigma}_{\mathrm{sd}}, \tag{2.2}$$

where $\hat{\sigma}$, $\hat{\sigma}_{\mathrm{sa}}$, and $\hat{\sigma}_{\mathrm{sd}}$ denote the surface tensions at the droplet-atmosphere interface,

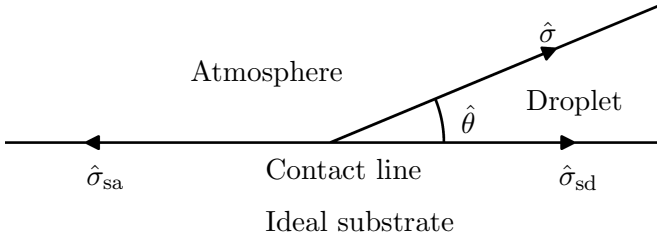

Figure 2.1: Sketch of the contact line for a low wetting droplet on an ideal substrate.

the substrate-atmosphere interface, and the substrate-droplet interface, respectively. Figure 2.1 shows a sketch of the contact line for a low wetting droplet on an ideal substrate.

The degree of wetting is characterised by the value of $\hat{\theta}$. We refer to $\hat{\theta} = 0$ as total wetting, $0 < \hat{\theta} \leq \pi/2$ as high wetting, $\pi/2 < \hat{\theta} < \pi$ as low wetting and $\hat{\theta} = \pi$ as zero wetting. Although equation (2.2) states that a droplet deposited onto an ideal substrate has a unique equilibrium contact angle, in reality, substrates are non-ideal, and surface roughness and/or chemical heterogeneities allow for contact line pinning, and hence in practice there is usually a range of stable equilibrium contact angles (see for example, Zhang *et al.* [169]).

2.2.2 The Young–Laplace equation

The liquid droplet is composed of molecules attracted to one another by cohesive forces (*i.e.* forces between like molecules). Every molecule in the bulk of the droplet experiences equal attraction in all directions by neighbouring molecules, and as a result the net cohesive force acting on the molecule is zero. However, when adhesive forces between the molecules in the atmosphere and the molecules in the droplet are negligible, then the liquid molecules on the surface of the droplet will experience a net force of cohesion in the direction of the inward normal to the surface. The cohesive force acting on a surface element must balance with a difference in normal stress across the

droplet-atmosphere interface, expressed as [108, pp. 173–176]

$$\hat{\boldsymbol{n}} \cdot (\Delta \hat{\boldsymbol{T}}) \cdot \hat{\boldsymbol{n}} = \hat{\sigma}(\hat{\nabla} \cdot \boldsymbol{n}), \tag{2.3}$$

where $\hat{\boldsymbol{n}}$ is the unit normal to the free surface, and

$$\Delta \hat{\boldsymbol{T}} = -\Delta \hat{p} \boldsymbol{I} + \hat{\mu} \left[\hat{\nabla} \hat{\boldsymbol{u}} + (\hat{\nabla} \hat{\boldsymbol{u}})^T \right] \tag{2.4}$$

is the stress tensor difference across the free surface of a droplet of Newtonian liquid, with $\Delta \hat{p} = \hat{p} - \hat{p}^{\mathrm{a}}$ denoting the pressure difference across the free surface, $\hat{\boldsymbol{u}}$ denoting the velocity field within the liquid, and $\boldsymbol{I}$ denoting the identity tensor. In writing (2.4) we have taken the viscosity of the atmosphere to be negligible, i.e. $\hat{\mu}^{\mathrm{a}} = 0$.

In addition to the normal stress balance (2.4), the tangential stress difference must satisfy

$$\hat{\boldsymbol{n}} \cdot (\Delta \hat{\boldsymbol{T}}) \cdot \hat{\boldsymbol{t}} = \hat{\nabla} \hat{\sigma} \cdot \hat{\boldsymbol{t}}, \tag{2.5}$$

where $\hat{\boldsymbol{t}}$ is a unit tangent to the free surface.

In general, $\hat{\sigma}$ depends on $\hat{T}$ (see for example, Sultan *et al.* [147] who consider a linear expression of $\hat{\sigma}(\hat{T})$). However, for the small magnitudes of cooling (< 10 K) considered in the present work, the variation in σ across the surface of the droplet is only 1%, and so $\hat{\sigma}$ can reasonably be assumed to be constant.

If we consider uniform surface tension, i.e. $\hat{\nabla} \hat{\sigma} = \boldsymbol{0}$, then equation (2.5) reduces to

$$\hat{\boldsymbol{n}} \cdot (\Delta \hat{\boldsymbol{T}}) \cdot \hat{\boldsymbol{t}} = 0. \tag{2.6}$$

We scale $\hat{\boldsymbol{u}} = \hat{U} \boldsymbol{u}$, $\Delta \hat{p} = (\hat{\sigma}/\hat{L}) \Delta p$ and $\hat{L} \hat{\nabla} = \nabla$, where $\hat{U} = \hat{L}/\hat{\tau}$ is the characteristic velocity scale, $\hat{L}$ is the characteristic length scale and $\hat{\tau}$ is the time scale given by (2.1). Thus, from equation (2.3) we have

$$\boldsymbol{n} \cdot (\Delta p \boldsymbol{I}) \cdot \boldsymbol{n} - \frac{\hat{\mu} \hat{U}}{\hat{\sigma}} \boldsymbol{n} \cdot \left[\nabla \boldsymbol{u} + (\nabla \boldsymbol{u})^T \right] \cdot \boldsymbol{n} = -\nabla \cdot \boldsymbol{n}. \tag{2.7}$$

Liquid	Ca	We	Re	Bo	Fo_m	Pe_m
Water	3.2×10^{-4}	8.2×10^{-3}	25.6	1.4×10^{-1}	2.6×10^{4}	3.8×10^{-5}
Methanol	3.8×10^{-4}	8.0×10^{-3}	21.1	3.5×10^{-1}	1.2×10^{3}	7.7×10^{-4}
Acetone	1.0×10^{-4}	2.8×10^{-3}	28.0	5.9×10^{-1}	2.1×10^{2}	4.8×10^{-3}
Toluene	1.4×10^{-4}	3.7×10^{-3}	26.4	3.2×10^{-1}	3.8×10^{3}	2.6×10^{-3}

Table 2.3: Typical values of nondimensional groups defined throughout this chapter for droplets of various liquids evaporating into air calculated using values from table 2.1.

The dimensionless group

$$\mathrm{Ca} = \frac{\hat{\mu}\hat{U}}{\hat{\sigma}} \tag{2.8}$$

is the capillary number which characterises the ratio of the magnitude of viscous forces to the magnitude of surface tension forces acting across the interface. Table 2.3 shows typical values of nondimensional groups defined throughout this chapter for droplets of various liquids evaporating into air calculated using values from table 2.1. Table 2.3 shows that for droplets of various standard liquids $\mathrm{Ca} \ll 1$. A small capillary number $\mathrm{Ca} \ll 1$ characterises a situation where surface tension forces dominate, thus the viscous term in equation (2.7) is negligible, i.e. equation (2.7) becomes

$$\boldsymbol{n} \cdot (\Delta p \boldsymbol{I}) \cdot \boldsymbol{n} = -\nabla \cdot \boldsymbol{n}. \tag{2.9}$$

Equation (2.9) is the dimensionless form of the Young–Laplace equation [167] and may be written simply as

$$\Delta p = -\nabla \cdot \boldsymbol{n} = \kappa, \tag{2.10}$$

where κ is the mean curvature of the free surface.

2.2.3 The free surface of the droplet

To determine the shape of the free surface of the droplet, we consider the dimensional Navier–Stokes equation for the flow within the droplet

$$\frac{\partial \hat{\boldsymbol{u}}}{\partial \hat{t}} + (\hat{\boldsymbol{u}} \cdot \hat{\nabla})\hat{\boldsymbol{u}} = \hat{\boldsymbol{f}} - \frac{\hat{\nabla}\hat{p}}{\hat{\rho}} + \frac{\hat{\mu}}{\hat{\rho}}\hat{\nabla}^2\hat{\boldsymbol{u}}, \tag{2.11}$$

where $\hat{\boldsymbol{f}} = -\hat{g}\boldsymbol{e}_z$ and $\hat{g}$ is gravitational acceleration. Scaling $\hat{\boldsymbol{u}} = \hat{U}\boldsymbol{u} = (\hat{L}\boldsymbol{u})/\hat{\tau},\ \hat{t} = \hat{\tau}t,\ \hat{L}\hat{\nabla} = \nabla,\ \hat{p} = (\hat{\sigma}/\hat{L})p,\ \hat{\boldsymbol{f}} = \hat{g}\boldsymbol{f}$, where $\hat{\tau}$ is the time scale given by (2.1), we obtain from equation (2.11)

$$\mathrm{We}\left(\frac{\partial \boldsymbol{u}}{\partial t} + (\boldsymbol{u} \cdot \nabla)\boldsymbol{u}\right) = \mathrm{Bo}\boldsymbol{f} - \nabla p + \mathrm{Ca}\nabla^2\boldsymbol{u}, \tag{2.12}$$

where we have introduced the following dimensionless groups.

The Weber number

$$\mathrm{We} = \frac{\hat{L}\hat{\rho}\hat{U}^2}{\hat{\sigma}} \tag{2.13}$$

characterises the ratio of the magnitude of inertial forces to the magnitude of capillary forces within the fluid.

The Bond number

$$\mathrm{Bo} = \frac{\hat{L}^2\hat{\rho}\hat{g}}{\hat{\sigma}} \tag{2.14}$$

characterises the ratio of the magnitude of the force of gravity to the magnitude of the capillary forces acting on the droplet.

Table 2.3 shows that for droplets of various standard liquids $\mathrm{We} \ll 1$. We note that these values of the Bond number are not much smaller than unity. Picknett and Bexon [102] remarked that for the millimetre-sized droplets they investigated, due to a non-negligible Bond number, the droplets were not perfectly-spherical caps. However, using the same values quoted in table 2.1, for a methanol droplet with radius $\hat{L} = 1 \times 10^{-4}$

m (instead of $\hat{L} = 1 \times 10^{-3}$ m) we obtain Bo $= 3.5 \times 10^{-3}$ (instead of Bo $= 3.5 \times 10^{-1}$). Thus, for submillimetre sized droplets there is a physical regime for which Bo $\ll 1$, Ca $\ll 1$ and We $\ll 1$. Although a droplet with the parameters quoted in table 2.1 is not quite in this regime, throughout this thesis we assume Bo $\ll 1$, Ca $\ll 1$ and We $\ll 1$. In this regime equation (2.12) reduces to

$$\nabla p = 0, \tag{2.15}$$

so p is constant throughout the droplet.

The conventional Reynolds number Re can be expressed in terms of Ca and We as

$$\mathrm{Re} = \frac{\hat{\rho}\hat{U}\hat{L}}{\hat{\mu}} = \frac{\mathrm{We}}{\mathrm{Ca}}, \tag{2.16}$$

and is also included in table 2.3 for completeness.

2.2.4 Axisymmetric droplet

In chapters 3 and 4 we consider the evaporation of axisymmetric droplets, thus it is natural to work in cylindrical coordinates $(\hat{r}, \hat{\phi}, \hat{z}) = (\hat{L}r, \hat{\phi}, \hat{L}z)$. In this coordinate system equations (2.10) and (2.15) are satisfied by a spherical cap of radius $\mathcal{R} = R/\sin\hat{\theta}$, the free surface of which is given by

$$h(r,t) = \pm\sqrt{\mathcal{R}^2 - r^2} - \mathcal{R}\cos\hat{\theta}, \tag{2.17}$$

where a positive sign gives the upper hemisphere of the surface, and a negative sign gives the lower hemisphere of the surface.

It is often convenient to express the free surface in terms of the contact radius R, namely

$$h(r,t) = \pm\sqrt{\frac{R^2}{\sin^2\hat{\theta}} - r^2} - R\cot\hat{\theta}. \tag{2.18}$$

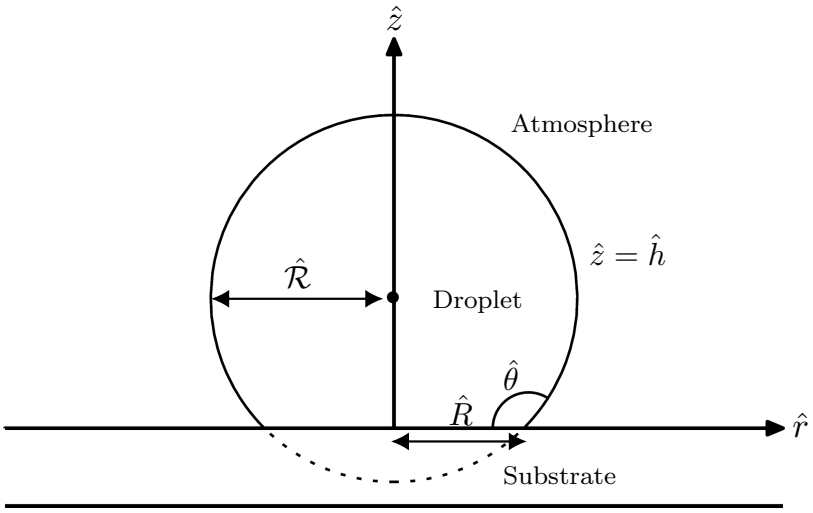

Figure 2.2: Cross-sectional view of an axisymmetric droplet with radius $\hat{\mathcal{R}}$, contact radius $\hat{R}$, and contact angle $\hat{\theta}$.

The volume of the spherical cap with contact radius R is given by

$$\begin{aligned} V(t) &= \frac{\pi}{6} R \tan\left(\frac{\hat{\theta}}{2}\right)\left(3R^2 + R^2 \tan^2\left(\frac{\hat{\theta}}{2}\right)\right) \\ &= \frac{\pi R^3 \sin\hat{\theta}(\cos\hat{\theta} + 2)}{3(\cos\hat{\theta} + 1)^2}. \end{aligned} \tag{2.19}$$

By rescaling the free surface (2.18) we obtain the dimensional free surface

$$\hat{h}(\hat{r}, \hat{t}) = \pm\sqrt{\frac{\hat{R}^2}{\sin^2\hat{\theta}} - \hat{r}^2} - \hat{R}\cot\hat{\theta}. \tag{2.20}$$

Figure 2.2 shows the geometry of an axisymmetric droplet with a free surface given by equation (2.20).

2.2.5 2D droplet

In chapter 5 we consider the evaporation of 2D droplets. When studying 2D droplets it is natural to work in Cartesian coordinates $(\hat{x}, \hat{y}) = \hat{L}(x, y)$. In this coordinate system

equations (2.10) and (2.15) are satisfied by a cylindrical cap of radius $\mathcal{R} = R/\sin\hat{\theta}$, the free surface of which is now given by

$$h(x,t) = \pm\sqrt{\frac{R^2}{\sin^2\hat{\theta}} - x^2} - R\cot\hat{\theta}. \tag{2.21}$$

Note that the equivalent cross-section for the axisymmetric droplet (2.18) is recovered by replacing $\hat{y} = \hat{z}$ and $\hat{x} = \hat{r}$. The cross-sectional area of the cylindrical cap with contact radius R is given by

$$A(t) = R^2\left(\frac{\hat{\theta}}{\sin^2\hat{\theta}} - \cot\hat{\theta}\right). \tag{2.22}$$

2.3 Diffusion-limited models

2.3.1 Thermally-coupled model

As discussed in chapter 1, previous authors have shown that the rate of evaporation for a sessile droplet is often governed by the diffusion of vapour in the atmosphere. Here we give a full formulation of the diffusion-limited model using axisymmetric polar coordinates $(\hat{r},\hat{z})$. The formulation of the corresponding 2D model follows the corresponding procedure using Cartesian coordinates $(\hat{x},\hat{y})$.

The distribution of vapour concentration $\hat{c}$ is governed by the advection-diffusion equation

$$\frac{\partial\hat{c}}{\partial\hat{t}} = \hat{\nabla}\cdot(\hat{D}\hat{\nabla}\hat{c}) - \hat{\nabla}\cdot(\hat{\boldsymbol{u}}^{\mathrm{a}}\hat{c}), \tag{2.23}$$

where $\hat{D}$ and $\hat{\boldsymbol{u}}^{\mathrm{a}}$ denote the diffusivity of vapour through the atmosphere and the

velocity in the atmosphere, respectively. Equation (2.23) can be rewritten as

$$\frac{1}{\mathrm{Fo}_m}\frac{\partial c}{\partial t} = \nabla^2 c - \mathrm{Pe}_m \nabla \cdot (\boldsymbol{u}^{\mathrm{a}} c), \tag{2.24}$$

where we have introduced the following dimensionless groups.

The (mass) Péclet number

$$\mathrm{Pe}_m = \frac{\hat{L}\hat{U}}{\hat{D}} \tag{2.25}$$

characterises the ratio of the magnitude of diffusive transport of mass to the magnitude of advective transport of mass.

The (mass) Fourier number

$$\mathrm{Fo}_m = \frac{\hat{\tau}\hat{D}}{\hat{L}^2} \tag{2.26}$$

characterises the ratio of the magnitude of the evaporative timescale to the magnitude of the mass diffusion timescale. Since in the diffusion-limited model $\hat{U} = \hat{L}/\hat{\tau}$, from (2.25) and (2.26) $\mathrm{Pe}_m = 1/\mathrm{Fo}_m$. Note that this equality does not necessarily hold in regimes that are not diffusion limited.

Table 2.3 shows that for droplets of various standard liquids $\mathrm{Fo}_m \gg 1$ and $\mathrm{Pe}_m \ll 1$. In this regime equation (2.23) reduces to

$$\hat{\nabla}^2 \hat{c} = 0. \tag{2.27}$$

Equation (2.27) is subject to the boundary conditions

$$\hat{c} = \hat{c}_{\mathrm{sat}} \qquad \text{on } \hat{z} = \hat{h}, \tag{2.28}$$

$$\hat{c} \to \hat{c}_\infty \qquad \text{as } \sqrt{\hat{r}^2 + \hat{z}^2} \to \infty \text{ and } \hat{z} > 0, \tag{2.29}$$

$$\frac{\partial \hat{c}}{\partial \hat{z}} = 0 \qquad \text{on } \hat{z} = 0 \text{ for } \hat{r} > \hat{R}, \tag{2.30}$$

where $\hat{c}_{\mathrm{sat}} = \hat{c}_{\mathrm{sat}}(\hat{T})$ denotes the saturation concentration of vapour and $\hat{c}_\infty$ denotes the

constant ambient concentration far from the droplet. We follow, for example, Sefiane *et al.* [121] and couple the saturation concentration at the free surface of the droplet to the temperature of the free surface of the droplet by choosing

$$\hat{c}_{\mathrm{sat}} = \hat{c}_{\mathrm{sat}}(\hat{T}), \tag{2.31}$$

where the function $\hat{c}_{\mathrm{sat}}(\hat{T})$ is, in general, expressed as a polynomial in $\hat{T} - \hat{T}_\infty$ given as

$$\hat{c}_{\mathrm{sat}}(\hat{T}) = \sum_{i=0}^{n} \hat{a}_i \frac{(\hat{T} - \hat{T}_\infty)^i}{i!}, \tag{2.32}$$

where $\hat{a}_i = \mathrm{d}^i \hat{c}_{\mathrm{sat}}/\mathrm{d}\hat{T}^i(\hat{T}_\infty)$ and $\hat{T}_\infty$ denotes the constant ambient atmospheric temperature.

Figure 2.3 shows $\hat{c}_{\mathrm{sat}}(\hat{T})$ as given by equation (2.32) for $n = 0, \ldots, 4$ for water vapour in air at $\hat{T}_\infty = 295$ K, using the values of a_i given by Sefiane *et al.* [121]. The present figure 2.3 is a corrected and extended version of figure 7 in Sefiane *et al.* [121]; specifically the quadratic curve ($n = 2$) has been corrected, and we have also included the constant ($n = 0$) and cubic ($n = 3$) expressions for completeness. We expect that $\mathrm{d}\hat{c}_{\mathrm{sat}}/\mathrm{d}\hat{T} > 0$, and so unphysical parts of the curves with $\mathrm{d}\hat{c}_{\mathrm{sat}}/\mathrm{d}\hat{T} < 0$ are plotted with a dotted curve. To emphasize the differences in each approximation, figure 2.3 shows $\hat{c}_{\mathrm{sat}}(\hat{T})$ plotted over a large range of $\hat{T}$. However, throughout this thesis we are primarily concerned with small magnitudes of evaporative cooling, < 10 K.

Since the vapour distribution in the atmosphere is temperature-dependent via equation (2.28) with (2.31), we must solve an appropriate temperature equation to find the temperature distribution in the system. As with the vapour concentration, the temperature is governed by the advection-diffusion equation. For simplicity, we split the temperature equation for the entire system into three separate temperature equations, namely

$$\frac{\partial \hat{T}^i}{\partial \hat{t}} = \hat{\alpha}^i \hat{\nabla}^2 \hat{T}^i - \hat{\nabla} \cdot (\hat{\boldsymbol{u}}^i \hat{T}^i), \tag{2.33}$$

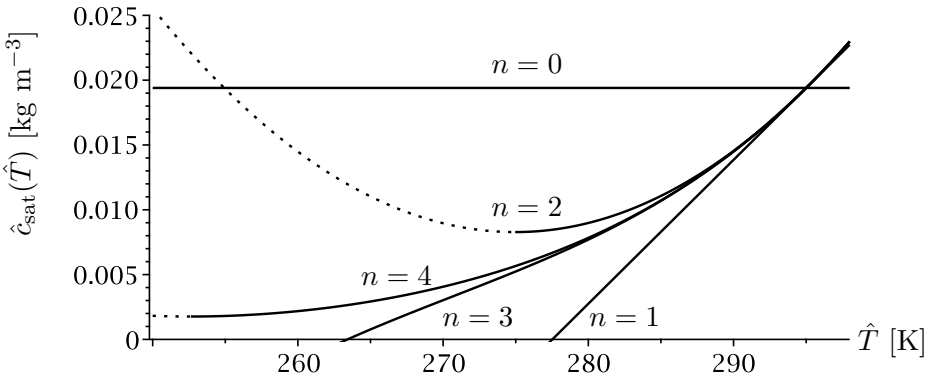

Figure 2.3: Saturation concentration of vapour $\hat{c}_{\mathrm{sat}}(\hat{T})$ as given by equation (2.32) for $n = 0, \ldots, 4$, for water vapour in air at $\hat{T}_\infty = 295$ K, using the values of a_i given by Sefiane *et al.* [121]. We expect that $\mathrm{d}\hat{c}_{\mathrm{sat}}/\mathrm{d}\hat{T} > 0$, and so unphysical parts of the curves with $\mathrm{d}\hat{c}_{\mathrm{sat}}/\mathrm{d}\hat{T} < 0$ are plotted with a dotted curve.

where $\hat{\alpha}^i = \hat{k}^i/\hat{\rho}^i\hat{c}^i_{\mathrm{p}}$ denotes the thermal diffusivity within the domain, $\hat{\boldsymbol{u}}^i$ denotes velocity within the domain and an index $i = \mathrm{a}$ denotes atmospheric quantities, an index $i = \mathrm{s}$ denotes substrate quantities, and the absence of an index denotes droplet quantities. As before, we rewrite equation (2.33) as

$$\frac{1}{\mathrm{Fo}^i_h}\frac{\partial T^i}{\partial t} = \nabla^2 T^i - \mathrm{Pe}^i_h \nabla \cdot (\boldsymbol{u}^i \hat{T}^i), \tag{2.34}$$

where

$$\mathrm{Fo}^i_h = \frac{\hat{\alpha}^i \hat{\tau}}{\hat{L}^2} \tag{2.35}$$

is the (thermal) Fourier number which characterises the ratio of the evaporative timescale to the thermal diffusive timescale, and

$$\mathrm{Pe}^i_h = \frac{\hat{L}\hat{U}^i}{\hat{\alpha}^i} \tag{2.36}$$

is the (thermal) Péclet number which characterises the ratio of the magnitude of diffusive transport of heat to the magnitude of advective transport of heat.

Table 2.4 shows values of Fo^i_h and Pe^i_h for various substances calculated using values

Atmosphere	$\mathrm{Fo}_h^{\mathrm{a}}$	$\mathrm{Pe}_h^{\mathrm{a}}$
Air ($\hat{c}_\infty = 0.4 \times \hat{c}_{\mathrm{sat}}$)	8.0×10^3	1.25×10^{-4}

Liquid	Fo_h	Pe_h
Water	5.5×10^1	1.8×10^{-2}
Methanol	4.4×10^0	2.3×10^{-1}
Acetone	1.8×10^0	5.5×10^{-1}

Substrate	$\mathrm{Fo}_h^{\mathrm{s}}$	$\mathrm{Pe}_h^{\mathrm{s}}$
Aluminium	4.6×10^4	0
PTFE	4.2×10^1	0
Aerogel	1.54×10^3	0

Table 2.4: Typical values of Fo_h^i and Pe_h^i for various substances calculated using values from tables 2.1 and 2.2, as well as properties of air given by Tsilingiris [153]. For the atmosphere and the substrate we have used $\hat{\tau} = 1073$ s, which corresponds to the water droplet evaporation quoted by Dunn *et al.* [51].

from tables 2.1 and 2.2, as well as properties of air given by Tsilingiris [153]. In particular, we use $\hat{\alpha}^{\mathrm{a}} = 2.1 \times 10^{-5}$ m^2 s^{-1} to calculate $\mathrm{Fo}_h^{\mathrm{a}}$ and $\mathrm{Pe}_h^{\mathrm{a}}$. Table 2.4 shows that for various standard substances, $\mathrm{Fo}_h^i \gg 1$ and $\mathrm{Pe}_h^i \ll 1$. Note that for methanol and acetone Fo_h is not much larger, and Pe_h is not much smaller, than unity. However, as we later discuss in chapters 3 and 4, it is possible to obtain longer-living droplets of methanol and acetone, which exist in the regime $\mathrm{Fo}_h^i \gg 1$ and $\mathrm{Pe}_h^i \ll 1$. In this regime equation (2.33) reduces to

$$\hat{\nabla}^2 \hat{T}^i = 0. \tag{2.37}$$

We solve equation (2.37) subject to the following boundary conditions. The temperature of the atmosphere approaches the ambient value far from the droplet, i.e.

$$\hat{T}^{\mathrm{a}} \to \hat{T}_\infty \qquad \text{as } \sqrt{\hat{r}^2 + \hat{z}^2} \to \infty \text{ for } \hat{z} > 0. \tag{2.38}$$

The temperature of the substrate takes the ambient value on its lower surface and far

from the droplet, i.e.

$$\hat{T}^{\mathrm{s}} = \hat{T}_{\infty} \qquad \text{on } \hat{z} = -\hat{h}^{\mathrm{s}} \quad \text{and} \quad \text{in } -\hat{h}^{\mathrm{s}} \leq \hat{z} \leq 0 \text{ as } \hat{r} \to \infty. \tag{2.39}$$

The temperature is continuous across the atmosphere-droplet, atmosphere-substrate and droplet-substrate interfaces, i.e.

$$\hat{T}^{\mathrm{a}} = \hat{T} \qquad \text{on } \hat{z} = \hat{h}, \tag{2.40}$$

$$\hat{T}^{\mathrm{a}} = \hat{T}^{\mathrm{s}} \qquad \text{on } \hat{z} = 0, \ \hat{r} > \hat{R}, \tag{2.41}$$

$$\hat{T} = \hat{T}^{\mathrm{s}} \qquad \text{on } \hat{z} = 0, \ \hat{r} < \hat{R}, \tag{2.42}$$

respectively.

The heat flux is continuous across the atmosphere-substrate and droplet-substrate interfaces, i.e.

$$\hat{k}^{\mathrm{a}} \frac{\partial \hat{T}^{\mathrm{a}}}{\partial \hat{z}} = \hat{k}^{\mathrm{s}} \frac{\partial \hat{T}^{\mathrm{s}}}{\partial \hat{z}} \qquad \text{on } \hat{z} = 0, \ \hat{r} > \hat{R}, \tag{2.43}$$

$$\hat{k} \frac{\partial \hat{T}}{\partial \hat{z}} = \hat{k}^{\mathrm{s}} \frac{\partial \hat{T}^{\mathrm{s}}}{\partial \hat{z}} \qquad \text{on } \hat{z} = 0, \ \hat{r} < \hat{R}. \tag{2.44}$$

The heat flux across the atmosphere-droplet interface satisfies the local energy balance

$$\frac{1}{\hat{\mathcal{L}}} \hat{\boldsymbol{n}} \cdot \hat{\nabla} \left(\hat{k} \hat{T} - \hat{k}^{\mathrm{a}} \hat{T}^{\mathrm{a}} \right) = \hat{\boldsymbol{n}} \cdot \hat{D} \hat{\nabla} \hat{c} = -\hat{J} \qquad \text{on } \hat{z} = \hat{h}, \tag{2.45}$$

where $\hat{J}(\hat{r}, \hat{t})$ denotes the evaporative mass flux from the free surface of the droplet. The rate of change of the mass of the droplet is found by integrating the mass flux over the free surface of the droplet, i.e.

$$\hat{\rho} \frac{\mathrm{d}\hat{V}}{\mathrm{d}\hat{t}} = -\int \hat{J} \mathrm{d}\hat{S}. \tag{2.46}$$

In chapter 3 we numerically solve the thermally-coupled model and obtain numerical

solutions for vapour concentration, temperature and droplet lifetimes. In chapter 4 we analytically solve the reduced form of the thermally-coupled model described in section 2.5 and obtain closed-form solutions for vapour concentration, temperature and droplet lifetimes.

2.3.2 Comparison with similar thermally-coupled models

The present thermally-coupled model described here differs slightly from the thermally-coupled models previously used by Dunn *et al.* [51] and Ristenpart *et al.* [112]. In the present model, the vapour distribution is coupled to the temperature everywhere, whereas in the Dunn model the vapour distribution is coupled to the temperature distribution in the droplet and substrate only. To decouple atmospheric thermal effects, Dunn *et al.* [51] neglected conditions (2.38), (2.40) and (2.43), and replaced the boundary conditions (2.41) and (2.45) as follows.

Instead of condition (2.41) Dunn *et al.* [51] imposed

$$\hat{T}^{\mathrm{s}} = \hat{T}_{\infty} \qquad \text{on } \hat{z} = 0,\ \hat{r} > \hat{R}, \tag{2.47}$$

and instead of condition (2.45) Dunn *et al.* [51] imposed

$$\frac{\hat{k}}{\hat{\mathcal{L}}}\hat{\boldsymbol{n}} \cdot \hat{\nabla}\hat{T} = \hat{\boldsymbol{n}} \cdot \hat{D}\hat{\nabla}\hat{c} = -\hat{J} \qquad \text{on } \hat{z} = \hat{h}. \tag{2.48}$$

Neglecting the atmospheric temperature field by taking specific limits of the thermally-coupled model is common practice (see, for example, [83, 112]). However, the Dunn model cannot be recovered by taking a limit of the thermally-coupled model. Condition (2.47) fixes the temperature of the unwetted upper surface of the substrate. This means that, as we will show in section 3.3.4, the unwetted upper surface of the substrate cannot cool, but the wetted upper surface of the substrate can cool.

Unlike Dunn *et al.* [51], Ristenpart *et al.* [112] use a model in which the lower surface of the substrate is kept at a fixed temperature, but the entire upper surface of the substrate

is allowed to cool. To impose this condition, while still decoupling atmospheric thermal effects, Ristenpart *et al.* [112] impose condition (2.48), but replace condition (2.47) with

$$\frac{\partial \hat{T}^{\mathrm{s}}}{\partial \hat{z}} = 0 \qquad \text{on } \hat{z} = 0,\ \hat{r} > \hat{R}. \tag{2.49}$$

We note that conditions (2.48) and (2.49) are valid in the regime $\hat{k}^{\mathrm{a}} \ll \hat{k}^{\mathrm{s}}$ and $\hat{k}^{\mathrm{a}} \ll \hat{k}$ from conditions (2.45) and (2.43), respectively.

2.4 Non-dimensional thermally-coupled model

Denoting $\hat{R}(0) = \hat{R}_0$, $\hat{\theta}(0) = \hat{\theta}_0$ and $\hat{V}(0) = \hat{V}_0$, when considering axisymmetric droplets we introduce the following set of non-dimensional quantities:

$$\begin{gathered}
r = \hat{r}/\hat{R}_0, \quad z = \hat{z}/\hat{R}_0, \quad T = \hat{T}/\hat{T}_\infty, \quad T^{\mathrm{s}} = \hat{T}^{\mathrm{s}}/\hat{T}_\infty, \quad T^{\mathrm{a}} = \hat{T}^{\mathrm{a}}/\hat{T}_\infty, \quad h = \hat{h}/\hat{R}_0, \\
h^s = \hat{h}^{\mathrm{s}}/\hat{R}_0, \quad V = \hat{V}/\hat{R}_0^3, \quad \alpha = \hat{k}^{\mathrm{a}}/\hat{k}, \quad \beta = \hat{k}^{\mathrm{a}}/\hat{k}^{\mathrm{s}}, \quad c = \frac{\hat{c} - \hat{c}_\infty}{\hat{c}_{\mathrm{sat}}(\hat{T}_\infty) - \hat{c}_\infty}, \\
\gamma_i = \left.\frac{\mathrm{d}^i \hat{c}}{\mathrm{d}\hat{T}^i}\right|_{\hat{T}=\hat{T}_\infty} \frac{\hat{T}_\infty^i}{i!(\hat{c}_{\mathrm{sat}}(\hat{T}_\infty) - \hat{c}_\infty)}, \quad \lambda = \frac{\hat{T}_\infty \hat{k}}{\hat{D}\hat{\mathcal{L}}(\hat{c}_{\mathrm{sat}}(\hat{T}_\infty) - \hat{c}_\infty)}, \\
t = \frac{2\hat{D}(\hat{c}_{\mathrm{sat}}(\hat{T}_\infty) - \hat{c}_\infty)}{\hat{\rho}} \left(\frac{2\pi}{3\hat{V}_0}\right)^{2/3} \hat{t}, \quad J = \frac{\hat{R}_0}{2\hat{D}(\hat{c}_{\mathrm{sat}}(\hat{T}_\infty) - \hat{c}_\infty)} \hat{J}.
\end{gathered} \tag{2.50}$$

The non-dimensionalised thermally-coupled evaporation problem is given by the following equations and boundary conditions.

The free surface of the droplet h is given by equation (2.17) and the volume of the droplet is given by equation (2.19).

Laplace's equation for the vapour concentration (2.27) becomes

$$\nabla^2 c = 0 \quad \text{in the atmosphere.} \tag{2.51}$$

The boundary conditions on the concentration in the atmosphere (2.28)–(2.30) be-

come

$$c = \sum_{i=0}^{n} \gamma_i (T-1)^i \qquad \text{on } z = h, \tag{2.52}$$

$$c \to 0 \qquad \text{as } \sqrt{r^2+z^2} \to \infty \text{ and } z > 0, \tag{2.53}$$

$$\frac{\partial c}{\partial z} = 0 \qquad \text{on } z = 0 \text{ for } \hat{r} > \hat{R}, \tag{2.54}$$

respectively.

The three Laplace's equations for temperature in the atmosphere, droplet and substrate (2.37) become

$$\nabla^2 T^{\mathrm{a}} = 0 \quad \text{in the atmosphere,} \tag{2.55}$$

$$\nabla^2 T = 0 \quad \text{in the droplet,} \tag{2.56}$$

$$\nabla^2 T^{\mathrm{s}} = 0 \quad \text{in the substrate,} \tag{2.57}$$

respectively.

The ambient conditions on temperature (2.38) and (2.39) become

$$T^{\mathrm{a}} \to 1 \qquad \text{as } \sqrt{r^2+z^2} \to \infty \text{ for } z > 0, \tag{2.58}$$

$$T^{\mathrm{s}} = 1 \qquad \text{on } z = -h^s \quad \text{and} \quad \text{on } -h^s \le z \le 0 \text{ as } r \to \infty, \tag{2.59}$$

respectively.

The temperature continuity conditions (2.40)–(2.42) become

$$T^{\mathrm{a}} = T \qquad \text{on } z = h, \tag{2.60}$$

$$T^{\mathrm{a}} = T^{\mathrm{s}} \qquad \text{on } z = 0,\ r > R, \tag{2.61}$$

$$T = T^s \qquad \text{on } z = 0,\ 0 < r < R, \tag{2.62}$$

respectively.

The energy balance conditions (2.43)–(2.45) become

$$\beta \frac{\partial T^{\mathrm{a}}}{\partial z} = \frac{\partial T^{\mathrm{s}}}{\partial z} \qquad \text{on } z = 0,\ r > R, \tag{2.63}$$

$$\frac{\partial T}{\partial z} = \frac{\alpha}{\beta} \frac{\partial T^{\mathrm{s}}}{\partial z} \qquad \text{on } z = 0,\ 0 < r < R, \tag{2.64}$$

$$J = -\lambda \boldsymbol{n} \cdot \nabla \left(T - \alpha T^{\mathrm{a}} \right) = -\boldsymbol{n} \cdot \nabla c \qquad \text{on } z = h, \tag{2.65}$$

respectively.

The rate of change of the mass of the droplet (2.46) becomes

$$\frac{\mathrm{d}V}{\mathrm{d}t} = -\left(\frac{3\hat{V}_0}{2\pi} \right)^{2/3} \frac{1}{\hat{R}_0^2} \int J \mathrm{d}S. \tag{2.66}$$

2.5 Thermally-coupled model for a thin droplet evaporating on a thin substrate

The thermally-coupled model given in section 2.4 can be solved numerically, for example, by finite element methods [3, 5, 6, 133]. However, to make analytical progress with this model, further reductions are required. An approach used when modelling thin droplets, *i.e.* droplets for which $\hat{\theta}_0 \ll 1$, is to consider a thin-film limit in which we compare the magnitudes of various lengthscales, identify negligible quantities, and reduce the model further, for example [50, 52]. Moreover, when modelling thin substrates *i.e.* substrates for which $h^{\mathrm{s}} \ll 1$, the same principle of comparing characteristic lengthscales can be applied to the substrate, leading to a reduced model which is analytically tractable.

2.5.1 Rescaled equations and boundary conditions

Due to the different vertical lengthscales in the atmosphere, the droplet and the substrate we introduce the non-dimensional quantities $z^{\mathrm{a}} = z$, $\bar{z} = z/\hat{\theta}_0$ and $z^{\mathrm{s}} = z/h^{\mathrm{s}}$, to denote z in the atmosphere, the droplet and the substrate, respectively. To simplify

notation, we also introduce the non-dimensional quantities

$$\theta = \hat{\theta}/\hat{\theta}_0, \quad \bar{V} = V/\hat{\theta}_0, \quad \bar{h} = h/\hat{\theta}_0, \quad \bar{t} = t(9/\hat{\theta}_0)^{1/3}, \quad S = \beta h^{\mathrm{s}}/\alpha\hat{\theta}_0. \tag{2.67}$$

The new timescale introduced in (2.67) comes from taking the thin-film limit of the timescale in (2.50). Before we make any reductions, we rewrite the thermally-coupled model in these new non-dimensional quantities as follows.

The free surface of the droplet (2.17) becomes

$$\bar{h} = \frac{1}{\hat{\theta}_0}\left(\pm\sqrt{\frac{R^2}{\sin^2(\hat{\theta}_0\theta)} - r^2} - R\cot(\hat{\theta}_0\theta)\right). \tag{2.68}$$

The volume of the droplet (2.19) becomes

$$\bar{V} = \frac{\pi R^3 \sin(\hat{\theta}_0\theta)(\cos(\hat{\theta}_0\theta) + 2)}{\hat{\theta}_0 3(\cos(\hat{\theta}_0\theta) + 1)^2}. \tag{2.69}$$

Laplace's equation for the vapour concentration (2.51) remains as

$$\nabla^2 c = 0 \quad \text{in the atmosphere.} \tag{2.70}$$

The boundary conditions on the vapour concentration (2.52)–(2.54) become

$$c = \sum_{i=0}^{n} \gamma_i (T-1)^i \qquad \text{on } z^{\mathrm{a}} = \hat{\theta}_0 \bar{h}, \tag{2.71}$$

$$c \to 0 \qquad \text{as } \sqrt{r^2 + z^{\mathrm{a}2}} \to \infty \text{ and } z^{\mathrm{a}} > 0, \tag{2.72}$$

$$\frac{\partial c}{\partial z^{\mathrm{a}}} = 0 \qquad \text{on } z^{\mathrm{a}} = 0 \text{ for } \hat{r} > \hat{R}, \tag{2.73}$$

respectively.

The three Laplace's equations for the temperature in the atmosphere, droplet and

substrate (2.55)–(2.57) become

$$\frac{1}{r}\frac{\partial}{\partial r}\left(r\frac{\partial T^{\mathrm{a}}}{\partial r}\right)+\frac{\partial^2 T^{\mathrm{a}}}{\partial z^{\mathrm{a}2}}=0 \quad \text{in the atmosphere,} \tag{2.74}$$

$$\frac{1}{r}\frac{\partial}{\partial r}\left(r\frac{\partial T}{\partial r}\right)+\frac{1}{\hat{\theta}_0{}^2}\frac{\partial^2 T}{\partial \bar{z}^2}=0 \quad \text{in the droplet,} \tag{2.75}$$

$$\frac{1}{r}\frac{\partial}{\partial r}\left(r\frac{\partial T^{\mathrm{s}}}{\partial r}\right)+\frac{1}{h^{\mathrm{s}2}}\frac{\partial^2 T^{\mathrm{s}}}{\partial z^{\mathrm{s}2}}=0 \quad \text{in the substrate,} \tag{2.76}$$

respectively.

The energy balance conditions (2.63)–(2.65) become

$$\beta\left.\frac{\partial T^{\mathrm{a}}}{\partial z^{\mathrm{a}}}\right|_{z^{\mathrm{a}}=0}=\left.\frac{1}{h^{\mathrm{s}}}\frac{\partial T^{\mathrm{s}}}{\partial z}\right|_{z^{\mathrm{s}}=0} \qquad \text{for } r>R, \tag{2.77}$$

$$\left.\frac{1}{\hat{\theta}_0}\frac{\partial T}{\partial \bar{z}}\right|_{\bar{z}=0}=\left.\frac{\alpha}{\beta h^{\mathrm{s}}}\frac{\partial T^{\mathrm{s}}}{\partial z^{\mathrm{s}}}\right|_{z^{\mathrm{s}}=0} \qquad \text{for } 0<r<R, \tag{2.78}$$

$$J=-\left.\frac{\lambda}{\hat{\theta}_0}\frac{\partial T}{\partial \bar{z}}\right|_{\bar{z}=\bar{h}}+\lambda\alpha\left.\frac{\partial T^{\mathrm{a}}}{\partial z^{\mathrm{a}}}\right|_{z^{\mathrm{a}}=\hat{\theta}_0\bar{h}}=-\left.\frac{\partial c}{\partial z^{\mathrm{a}}}\right|_{z^{\mathrm{a}}=\hat{\theta}_0\bar{h}} \qquad \text{on } z=h, \tag{2.79}$$

respectively.

The rate of change of the mass of the droplet (2.66) becomes

$$\hat{\theta}_0^{2/3}9^{1/3}\frac{\mathrm{d}\bar{V}}{\mathrm{d}\bar{t}}=-\left(\frac{3\hat{V}_0}{2\pi}\right)^{2/3}\frac{1}{\hat{R}_0^2}\int J\mathrm{d}S. \tag{2.80}$$

2.5.2 Reduced equations and boundary conditions

At leading order in $\hat{\theta}_0 \ll 1$ and $h^{\mathrm{s}} \ll 1$ the equations given in section 2.5.1 reduce as follows.

The free surface of the droplet (2.68) becomes

$$\bar{h}=\theta\frac{R^2-r^2}{2R}. \tag{2.81}$$

The volume of the droplet (2.69) becomes

$$\bar{V} = \frac{\pi}{4}\theta R^3. \tag{2.82}$$

Laplace's equation for the vapour concentration (2.70) becomes

$$\frac{1}{r}\frac{\partial}{\partial r}\left(r\frac{\partial c}{\partial r}\right) + \frac{\partial^2 c}{\partial z^{\mathrm{a}2}} = 0 \quad \text{for } z^{\mathrm{a}} > 0. \tag{2.83}$$

The boundary conditions on the vapour concentration (2.52)–(2.54) become

$$c = \sum_{i=0}^{n} \gamma_i (T-1)^i \qquad \text{on } z^{\mathrm{a}} = 0 \text{ for } r < R, \tag{2.84}$$

$$c \to 0 \qquad \text{as } \sqrt{r^2 + z^{\mathrm{a}2}} \to \infty \text{ and } z^{\mathrm{a}} > 0, \tag{2.85}$$

$$\frac{\partial c}{\partial z^{\mathrm{a}}} = 0 \qquad \text{on } z^{\mathrm{a}} = 0 \text{ for } r > R, \tag{2.86}$$

respectively.

The three Laplace's equations for the temperature in the atmosphere, droplet and substrate (2.74)–(2.76) become

$$\frac{1}{r}\frac{\partial}{\partial r}\left(r\frac{\partial T^{\mathrm{a}}}{\partial r}\right) + \frac{\partial^2 T^{\mathrm{a}}}{\partial z^{\mathrm{a}2}} = 0 \quad \text{for } z^{\mathrm{a}} > 0, \tag{2.87}$$

$$\frac{\partial^2 T}{\partial \bar{z}^2} = 0 \quad \text{in the droplet,} \tag{2.88}$$

$$\frac{\partial^2 T^{\mathrm{s}}}{\partial z^{\mathrm{s}2}} = 0 \quad \text{in the substrate,} \tag{2.89}$$

respectively.

The energy balance conditions (2.77)–(2.79) become

$$h^{\mathrm{s}}\beta \left.\frac{\partial T^{\mathrm{a}}}{\partial z^{\mathrm{a}}}\right|_{z^{\mathrm{a}}=0} = \left.\frac{\partial T^{\mathrm{s}}}{\partial z^{\mathrm{s}}}\right|_{z^{\mathrm{s}}=0} \qquad \text{for } r > R, \tag{2.90}$$

$$S \left.\frac{\partial T}{\partial \bar{z}}\right|_{\bar{z}=0} = \left.\frac{\partial T^{\mathrm{s}}}{\partial z^{\mathrm{s}}}\right|_{z^{\mathrm{s}}=0} \qquad \text{for } 0 < r < R, \tag{2.91}$$

$$J = -\frac{1}{\alpha\hat{\theta}_0}\left.\frac{\partial T}{\partial \bar{z}}\right|_{\bar{z}=\bar{h}} + \left.\frac{\partial T^{\mathrm{a}}}{\partial z^{\mathrm{a}}}\right|_{z^{\mathrm{a}}=0} = -\frac{1}{\lambda\alpha}\left.\frac{\partial c}{\partial z^{\mathrm{a}}}\right|_{z^{\mathrm{a}}=0}, \tag{2.92}$$

respectively, where S is defined by (2.67).

The rate of change of the mass of the droplet (2.80) becomes

$$\frac{\mathrm{d}\bar{V}}{\mathrm{d}\bar{t}} = -2\pi \int_0^R Jr\mathrm{d}r. \tag{2.93}$$

We consider evaporation of a thin droplet on a thin substrate in chapter 4 and, in particular, obtain analytical expressions for the droplet evolution and lifetime.

2.6 Thermally-decoupled model

Setting $\gamma_i = 0$ for $i > 0$ in equation (2.52) gives $c_{\mathrm{sat}} \equiv 1$. This decouples the vapour distribution and the temperature distribution, thus recovering the thermally-decoupled evaporation model used by, for example [39, 102, 143, 144], and given as follows.

The distribution of vapour concentration c is governed by

$$\nabla^2 c = 0 \quad \text{in the atmosphere,} \tag{2.94}$$

subject to zero vapour flux normal to the substrate,

$$\frac{\partial c}{\partial z} = 0 \qquad \text{on } z = 0,\ r > R, \tag{2.95}$$

ambient saturation of the atmosphere far from the droplet,

$$c \to 0 \qquad \text{as } \sqrt{r^2 + z^{\mathrm{a}2}} \to \infty \text{ for } z^{\mathrm{a}} > 0, \tag{2.96}$$

and total saturation of the atmosphere at the free surface,

$$c = 1 \qquad \text{on } z = h. \tag{2.97}$$

2.6.1 Solutions to the thermally-decoupled model

As mentioned in chapter 1, the thermally-decoupled model has been the subject of scientific research for many decades. The earliest analytical solution for the thermally-decoupled model was given by Weber [156] who gave an analogous solution for the evaporation of thin droplets ($\hat{\theta} \ll 1$) in the electrostatic context of the electric field produced by a charged disc. In particular, from Weber's [156] solution, the dimensional evaporative flux from a thin droplet,

$$\hat{J} = \frac{2}{\pi} \frac{\hat{D}(\hat{c}_{\mathrm{sat}} - \hat{c}_{\infty})}{\sqrt{\hat{R}^2 - \hat{r}^2}}, \tag{2.98}$$

is found to be singular (but integrable) at the contact line of the droplet.

The analytical solution for the general case of a non-thin droplet with $0 < \hat{\theta} < \pi$ was first reported, again in the context of electrostatics, by Lebedev [75, pp. 221-224]. From Lebedev's [75] solution Deegan *et al.* [39] found an expression for the evaporative flux from a droplet with contact angle $\hat{\theta}$, namely

$$\hat{J} = \frac{\hat{D}(\hat{c}_{\mathrm{sat}} - \hat{c}_{\infty})}{\hat{R}} \left[\frac{1}{2} \sin\hat{\theta} + \sqrt{2}(\cosh\alpha + \cos\hat{\theta})^{3/2} \right.$$
$$\left. \times \int_0^{\infty} \frac{\tau \cosh\hat{\theta}\tau}{\cosh\pi\tau} \tanh[\tau(\pi - \hat{\theta})] P_{-1/2+i\tau}(\cosh\alpha) \mathrm{d}\tau \right], \tag{2.99}$$

where $P_{-1/2+i\tau}$ denotes the Legendre function of the first kind of degree $-1/2 + i\tau$ and

argument

$$\cosh\alpha = \frac{\hat{r}^2\cos\hat{\theta} \pm \hat{R}\sqrt{\hat{R}^2 - \hat{r}^2\sin^2\hat{\theta}}}{\hat{R}^2 - \hat{r}^2}. \tag{2.100}$$

Deegan *et al.* [37, 39] used a simpler approximate expression for the dimensional evaporative flux from a droplet, namely

$$\hat{J}(\hat{r},\hat{t}) \propto [1 - (\hat{r}/\hat{R})^2]^{-\lambda}, \tag{2.101}$$

where $\lambda = (\pi - 2\hat{\theta})/(2\pi - 2\hat{\theta})$. In particular, 2.101 reveals that the flux at the contact line of the droplet is singular for $\hat{\theta} < \pi/2$, finite for $\hat{\theta} = \pi/2$ and zero for $\hat{\theta} > \pi/2$.

In chapter 3 we compare the results of the thermally-coupled model to the results of the thermally-decoupled model. We also use the thermally-decoupled model to solve problems concerning the evaporation of 2D droplets in chapter 5.

2.6.2 Thermally-decoupled model for a thin droplet

As in the thermally-coupled model, in the limit in which the droplet is thin, the thermally-decoupled model simplifies because the profile of the droplet may be ignored when imposing the boundary conditions on $\hat{c}$. Specifically, the mathematical problem becomes that of solving for $\hat{c}$ in a half-space or other large domain, subject to appropriate mixed boundary conditions. As discussed in section 1.8, previous authors have investigated mathematically similar problems.

We consider the thermally-decoupled model for a thin droplet in two dimensions in chapter 5.

2.7 One-sided model

As previously mentioned, the models described in the section 2.3–2.6 are known as diffusion-limited models because the evaporation of the droplet is governed by the

quasi-steady diffusion of vapour. However, diffusion-limited models are not applicable for droplets which evaporate in a non-equilibrated regime. The non-equilibrium model is appropriate for modelling heated droplets.

The non-equilibrium model follows from the work of Schrage [119], who showed that evaporative flux in a non-equilibrated regime is proportional to the difference between the equilibrium vapour pressure $\hat{p}^{\mathrm{v}}_{\mathrm{sat}}$ and the actual vapour pressure $\hat{p}^{\mathrm{v}}$, as shown in the Hertz–Knudsen equation:

$$\hat{J} = \frac{\hat{\rho}^{\mathrm{v}}\hat{\mathcal{L}}\hat{L}}{\hat{k}\hat{T}^{*}}\sqrt{\frac{\bar{R}\hat{T}}{2\pi}}\left(\frac{\hat{p}^{\mathrm{v}}_{\mathrm{sat}}}{\hat{p}^{\mathrm{v}}} - 1\right), \tag{2.102}$$

where $\hat{T}^{*}$ denotes the equilibrium saturation temperature, $\hat{\rho}^{\mathrm{v}}$ denotes the density of the vapour, $\hat{T}$ is the temperature of the free surface, and $\bar{R}$ is the gas constant per unit mass.

As well as being applied to the evaporation of heated droplets [10, 11, 12, 137], non-equilibrium models can be used to model other physical phenomena, such as droplet spreading [7, 10, 138], the coffee-stain effect [101, 100], and vapour bubble dynamics [8, 9, 10]. We will not use the one-sided model in this thesis.

Chapter 3

Thermally-Coupled Model: Numerical Method and Results

3.1 Introduction

In this chapter we obtain numerical solutions to the thermally-coupled diffusion-limited evaporation model described in chapter 2. Following, for example, Dunn *et al.* [51] and Ait Saada *et al.* [5], we use a finite element based approach to solve the quasi-steady problem described in section 2.3. Specifically, we use the finite element analysis package COMSOL Multiphysics [1]. Using these quasi-steady solutions we use a simple time-stepping method to obtain the quasi-steady evolution, and hence the lifetime, of an evaporating droplet.

We first describe the numerical model. We then validate our numerical results against the results obtained numerically by Ait Saada *et al.* [5]. We then compare our numerical solutions to the thermally-coupled model described in section 2.3 with our numerical solutions to the Dunn model described in section 2.3.2 and the thermally-decoupled model described in section 2.6. In both cases we highlight the key differences between the present numerical method, and the numerical methods presented by Ait Saada *et al.* [5] and Dunn *et al.* [51], respectively. In particular, we show how these differences

contribute to the differences between our present results and the corresponding results of Ait Saada *et al.* [5] and Dunn *et al.* [51].

After validating our numerical results we conduct new investigations into the influence of various thermo-physical properties on the vapour concentration, temperature and evaporative flux. We also show how to recover the thermally-decoupled model from the thermally-coupled model. Finally, we present new calculations of the lifetimes of droplets with a wide range of initial contact angles on substrates with a wide range of thermal conductivities. All of these numerical calculations are carried out using the thermally-coupled model described in section 2.3 and using the physical parameter values shown in tables 2.1 and 2.2, unless otherwise specified.

3.2 Description of the numerical method

In this section we explain how we numerically implement the thermally-coupled model described in section 2.3. The numerical method presented here is broadly similar to that of Ait Saada *et al.* [5], with the exception of the meshing and time-stepping methods.

3.2.1 Geometry

We create a geometry for our computational model using the geometry tools provided in COMSOL Multiphysics. Since the computational domain must be finite, we follow, for example, Dunn *et al.* [51] and Ait Saada *et al.* [5], and replace the far-field conditions (2.29), (2.38) and (2.39) with boundary conditions imposed at a large but finite distance from the droplet, namely

$$\hat{c} = \hat{c}_\infty \qquad \text{on } \sqrt{\hat{r}^2 + \hat{z}^2} = \mathcal{S}\hat{R} \ \text{ for } \hat{z} > 0, \tag{3.1}$$

$$\hat{T}^{\mathrm{a}} = \hat{T}_\infty \qquad \text{on } \sqrt{\hat{r}^2 + \hat{z}^2} = \mathcal{S}\hat{R} \ \text{ for } \hat{z} > 0, \tag{3.2}$$

$$\hat{T}^{\mathrm{s}} = \hat{T}_\infty \qquad \text{on } \hat{z} = -\hat{h}^{\mathrm{s}},\ 0 \le \hat{r} \le \mathcal{S}\hat{R} \quad \text{and} \quad -\hat{h}^{\mathrm{s}} \le \hat{z} \le 0,\ \hat{r} = \mathcal{S}\hat{R}, \tag{3.3}$$

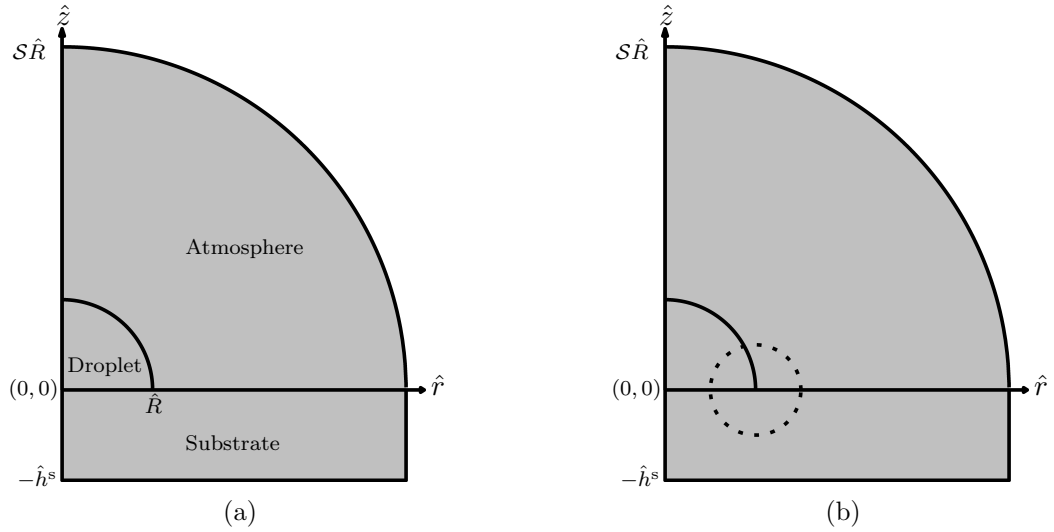

Figure 3.1: Sketch (not to scale) of the numerical domain on which we impose boundary conditions (3.1)–(3.3). (a) The computational subdomains representing the substrate, the droplet, and the atmosphere. (b) The circle (dotted) centred at the contact line within which we greatly increase the mesh resolution.

respectively, where $\mathcal{S}$ is a dimensionless number (typically 300) which determines the size of the computational domain. The lifetimes of a droplet evaluated using $\mathcal{S} = 300$ and using $\mathcal{S} = 400$ typically differ by $\approx 0.5\%$.

Figure 3.1 shows a sketch (not to scale) of the numerical domain with finite boundaries on which we impose conditions (3.1)–(3.3). Figure 3.1(a) illustrates the computational subdomains representing the substrate, the droplet and the atmosphere.

Since, as we have already described, the flux can be singular at to the contact line, to improve the accuracy of the solutions it is necessary to increase the mesh resolution near the contact line $(\hat{R}, 0)$. In section 3.2.3 below we follow Dunn *et al.* [51] and greatly increase the mesh resolution within a circle with a radius less than $\hat{h}^{\mathrm{s}}$ and $\hat{R}$, centred at the contact line. For all of the computations in this chapter we use a circle of radius $\min(\hat{h}^{\mathrm{s}}, \hat{R})/20$. Figure 3.1(b) illustrates the circle (dotted) centred at the contact line within which we greatly increase the mesh resolution.

3.2.2 Governing equations

We implement the equations to be solved using the *Mathematics* set of physics tools provided in COMSOL Multiphysics. The equations we have to solve are the Laplace equation for vapour concentration in the atmosphere, *i.e.* equation (2.27), and the three Laplace equations for temperature in the substrate, the droplet, and the atmosphere, *i.e.* equation (2.37). To create these we use the *Coefficient Form PDE* tool, which solves an equation of the form

$$e_a \frac{\partial^2 u}{\partial \hat{t}^2} + d_a \frac{\partial u}{\partial \hat{t}} + \hat{\nabla} \cdot (-c\hat{\nabla} u - \boldsymbol{\alpha} u + \boldsymbol{\gamma}) + \boldsymbol{\beta} \cdot \hat{\nabla} u + a u = f. \tag{3.4}$$

To implement the Laplace equations we simply set $e_a = 0$, $d_a = 0$, $c = 1$, $\boldsymbol{\alpha} = \mathbf{0}$, $\boldsymbol{\gamma} = \mathbf{0}$, $a = 0$, and $f = 0$. Since we need to solve equation (3.4) in cylindrical polar coordinates, and COMSOL Multiphysics takes $\hat{\nabla} = (\partial/\partial\hat{r}, \partial/\partial\hat{z})$, we set $\boldsymbol{\beta} = (-1/\hat{r}, 0)$.

3.2.3 Computational mesh

We create the computational mesh using the meshing tools provided in COMSOL Multiphysics. Before any mesh refinements are made, we apply a default free triangular mesh to the entire computational domain. We set the element size in this mesh to the COMSOL predefined setting *Extremely Fine*.

As previously mentioned, the flux can be singular (but integrable) at the contact line. Therefore, we find some mesh sensitivity of the flux near to the contact line. To ensure that the mesh sensitivity of the flux near to the contact line does not introduce a mesh sensitivity of the rate of change of volume of the droplet (*i.e.* the flux integrated along the free-surface of the droplet), and hence the lifetime of the droplets, we carry out a convergence check on the mesh.

For this convergence check the flux is evaluated using a series of meshes that are increasingly refined near to the contact line. The final two meshes in this series are denoted

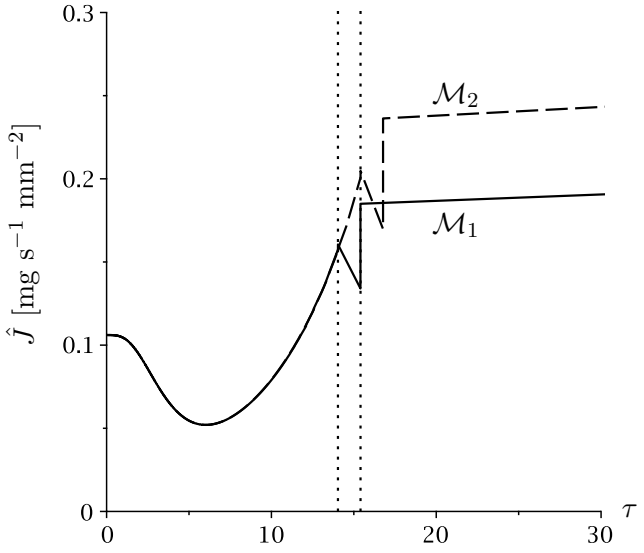

Figure 3.2: Numerically evaluated flux $\hat{J}$ plotted as a function of the toroidal coordinate τ for a typical droplet with contact angle $\hat{\theta} = 4\pi/5$ and contact radius $\hat{R} = 1$ mm, evaluated using $n = 1$ in equation (2.52). The dotted lines indicate the τ position on the free surface after which the two final mesh elements before the contact line lie. In order of increasing τ, the first and second dotted lines correspond to meshes $\mathcal{M}_1$ and $\mathcal{M}_2$, respectively.

$\mathcal{M}_1$ and $\mathcal{M}_2$, where the mesh elements close to the contact line in $\mathcal{M}_2$ are half the size of the corresponding elements in $\mathcal{M}_1$.

To show the mesh sensitivity of the flux we use the toroidal coordinates described in appendix A. In toroidal coordinates $\tau = 0$ corresponds to the top of the droplet and $\tau = \infty$ corresponds to the contact line. Figure 3.2 shows how the numerically evaluated flux $\hat{J}$ varies with the toroidal coordinate

$$\tau = \frac{1}{2} \ln \left(\frac{(\hat{r} + \hat{R})^2 + \hat{z}^2}{(\hat{r} - \hat{R})^2 + \hat{z}^2} \right)$$

for a typical droplet with contact angle $\hat{\theta} = 4\pi/5$ and contact radius $\hat{R} = 1$ mm, evaluated using $n = 1$ in equation (2.52). In figure 3.2 all but two of the mesh elements for $\mathcal{M}_1$ lie in $\tau < 14.0$ (indicated by the first dotted line). The final two mesh elements on the free surface of the droplet lie in $14.0 < \tau < 200$. No mesh elements lie in $\tau > 200$. For $\mathcal{M}_2$ the final two mesh elements on the free surface lie in $15.4 < \tau < 200$ (indicated by the second dotted line). Figure 3.2 shows that the mesh sensitivity caused by singular flux at the contact line only affects the final two mesh elements of the given mesh.

Plotting the flux profiles as functions of τ is useful for examining the behaviour of the numerical model near the contact line, but it enormously exaggerates the mesh dependency of our results. To determine the mesh sensitivity of the rate of change of the droplet volume, the difference in flux integrated along the free-surface of the droplet is considered. For the two meshes shown in figure 3.2, the difference in the flux integrated along the free-surface of the droplet is 0.037%. This difference is negligible, and thus demonstrates that the rate of change of the droplet volume, and hence the droplet lifetime, is not mesh sensitive.

For all of the computations described in this chapter we use the following mesh refinement. On the boundaries within the circular subdomain indicated by the dotted circle shown in figure 3.1(b) we set the maximum element size to $\hat{R}/1000$. On the remaining (unrefined) solid boundaries of the droplet subdomain we set the maximum element

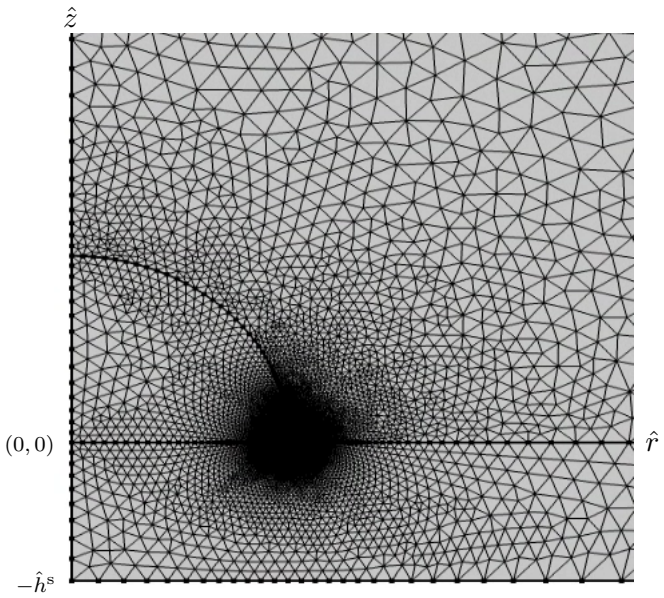

Figure 3.3: An example of the mesh close to the droplet, generated using the mesh refinements detailed within this section. This example was generated using $\hat{R} = 1.35$ mm, $\hat{\theta} = \pi/2$ and $\hat{h}^{\mathrm{s}} = 1$ mm.

size to $\hat{R}/100$. These meshes are found to be suitably refined near to the contact line, as per the mesh refinement check. A typical build of a mesh with these settings contains roughly 10^5 domain elements and 10^3 boundary elements. Figure 3.3 shows an example of the mesh close to the droplet, generated using the mesh refinements detailed within this section. This example was generated using $\hat{R} = 1.35$ mm, $\hat{\theta} = \pi/2$ and $\hat{h}^{\mathrm{s}} = 1$ mm. A typical runtime of the quasi-steady problem (including mesh building) using this mesh is about 30 seconds on a standard desktop computer.

3.2.4 Time-stepping and data extrapolation

With the finalised computational domain, equations and boundary conditions, and computational mesh we use the default stationary solver provided in COMSOL Multiphysics to numerically solve the quasi-steady problem described in section 2.3. Once the quasi-steady solution is obtained, we use the integration tools provided in COMSOL Multiphysics to evaluate the rate of change of the volume of the droplet, *i.e.* equation (2.52). Then, following Dunn *et al.* [51], we apply Euler's forward method

given generally by

$$\hat{V}_{n+1} = \hat{V}_n - \hat{t}_\delta \left| \frac{\mathrm{d}\hat{V}_n}{\mathrm{d}\hat{t}} \right|, \tag{3.5}$$

where $\hat{t}_\delta$ is the (constant) time-step

$$\hat{t}_\delta = \frac{\hat{V}_0}{\left| \frac{\mathrm{d}\hat{V}_0}{\mathrm{d}\hat{t}} \right| N}, \tag{3.6}$$

for which N is a dimensionless number (typically 500) that is kept constant for each evaluation of the droplet lifetime, to obtain the droplet volume at time $\hat{t} = n\hat{t}_\delta$.

Using the newly-obtained volume we rebuild the computational domain and mesh described in sections 3.2.1 and 3.2.3, respectively, and solve for $\mathrm{d}\hat{V}/\mathrm{d}\hat{t}$ at $\hat{t} = n\hat{t}_\delta$. This process of obtaining a new droplet volume is marched forward in time until the droplet volume reaches zero (or, in practice, first becomes slightly negative), at which point the computations are terminated. After obtaining an array of data for $\hat{V}$ at each time step we use the *Curvefitting* tools of Maplesoft Maple 2017 to obtain an extrapolated droplet lifetime. In particular, we use the linear *ArrayInterpolation* command on the final two volume data points.

A property of a robust finite element analysis mesh is the absence of so called "sliver elements", *i.e.* meshing elements with at least one hyperacute angle. Therefore, COMSOL Multiphysics does not allow triangular meshing elements with any angle less than ≈ 0.005 radians. Thus, it is necessary to use these same *Curvefitting* tools to extrapolate the droplet evolution for droplets whose contact angle becomes $0 < \hat{\theta} \lesssim 0.005$, *i.e.* does not become negative, during the lifetime calculation (typically for droplets evaporating in the CR mode with $\hat{\theta}_0 < 0.1$). A typical runtime for a single lifetime calculation is about four hours on a standard desktop computer.

We note that the time-stepping method described here is different from the one used by Ait Saada *et al.* [5]. We give a detailed comparison of the different time-stepping methods used in section 3.5.

3.3 Validating the numerical method

To begin to understand the coupled behaviour of vapour concentration and temperature distribution during evaporation, and to confirm that our numerical method is correctly implemented, we seek to reproduce the results given by Ait Saada *et al.* [5]. For this we use the physical parameters used by Ait Saada *et al.* [5]. Table 3.1 lists the physical parameters for the air atmosphere and the water droplet as used by Ait Saada *et al.* [5]. Table 3.1 also shows the physical properties of the various substrates used by Dunn *et al.* [51]. Note that some of the physical parameters in table 3.1 are different to the corresponding parameters in table 2.1. This is because Ait Saada *et al.* [5] consider a droplet that is 3.15 K warmer than the droplet considered by Dunn *et al.* [51].

Throughout this chapter we follow Ait Saada *et al.* [5] and also consider substrates with very large ($\hat{k}^s \to \infty$ W m^{-1} K^{-1}) and very small conductivities ($\hat{k}^s = 0$ W m^{-1} K^{-1}), in practice $\hat{k}^s = \hat{k} \times 10^4$ and $\hat{k}^s = \hat{k} \times 10^{-4}$, respectively. Although such substrates are not physically realistic, the results obtained in these extreme situations can help clearly demonstrate the influence of substrate conductivity on evaporation.

3.3.1 Validating the solution for the vapour concentration and temperature fields

We first consider the numerically calculated quasi-steady vapour concentration and temperature fields. The fixed temperatures of the lower surface of the substrate and the far-field act to anchor the temperature of the lower surface of the droplet at $\hat{T}_\infty$. However, the evaporation at the free surface of the droplet cools the droplet to below $\hat{T}_\infty$. Therefore, the temperature of the droplet depends on the physical properties of the system that determine the magnitudes of the thermal anchoring and the cooling effects.

Figure 3.4 shows the vapour concentration $\hat{c}$ for a droplet of water with contact angle $\hat{\theta} = 1.36$ and contact radius $\hat{R} = 1.86$ mm evaporating into air with $\hat{c}_\infty = 0.4\hat{c}_{\text{sat}}(\hat{T}_\infty)$ and $\hat{T}_\infty = 298.15$ K on (a) an infinitely conducting substrate ($\hat{k}^s \to \infty$ W m^{-1} K^{-1}) and

Air atmosphere [5]		
$\hat{\rho}^{\mathrm{a}}$	[kg m^{-3}]	1.1845×10^{2}
$\hat{\mu}^{\mathrm{a}}$	[kg m^{-1} s^{-1}]	1.844×10^{-5}
$\hat{c}_{\mathrm{p}}^{\mathrm{a}}$	[m^{2} s^{-2} K^{-1}]	1.0063×10^{3}
$\hat{k}^{\mathrm{a}}$	[W m^{-1} K^{-1}]	2.597×10^{-2}
$\hat{T}_{\infty}$	[K]	298.15

Water droplet [5]		
$\hat{R}_0$	[m]	1.86×10^{-3}
$\hat{\theta}_0$		1.361
$\hat{\rho}$	[kg m^{-3}]	9.97×10^{2}
$\hat{\mu}$	[kg m^{-1} s^{-1}]	8.68×10^{-4}
$\hat{D}$	[m^{2} s^{-1}]	2.50×10^{-5}
$\hat{\sigma}$	[kg s^{2}]	7.20×10^{-2}
$\hat{k}$	[W m^{-1} K^{-1}]	6.12×10^{-1}
$\hat{c}_{\mathrm{p}}$	[m^{2} s^{-2} K^{-1}]	4.07×10^{3}
$\hat{\mathcal{L}}$	[m^{2} s^{-2}]	2.44×10^{6}

Substrate [51]		Aluminium	Titanium	Macor	PTFE
$\hat{h}^{\mathrm{s}}$	[m]	1×10^{-3}	1×10^{-3}	1×10^{-3}	1×10^{-3}
$\hat{\rho}^{\mathrm{s}}$	[kg m^{-3}]	2.71×10^{3}	4.54×10^{3}	2.52×10^{3}	2.20×10^{3}
$\hat{c}_{\mathrm{p}}^{\mathrm{s}}$	[m^{2} s^{-2} K^{-1}]	913	523	790	1.05×10^{3}
$\hat{k}^{\mathrm{s}}$	[W m^{-1} K^{-1}]	237	21.9	1.46	0.25

Table 3.1: Physical parameters for the air atmosphere, water droplet and various substrates, as used by Ait Saada *et al.* [5] and Dunn *et al.* [51].

(b) a PTFE substrate ($\hat{k}^{\mathrm{s}} = 0.25$ W m^{-1} K^{-1}). Figure 3.4 also shows the temperature contours of $\hat{T}$, $\hat{T}^{\mathrm{s}}$ and $\hat{T}^{\mathrm{a}}$.

Figure 3.4 (a) shows that the infinitely conducting substrate has not cooled. However, figure 3.4 (b) shows that the PTFE substrate is cooled close to the droplet. This is because the larger conductivity anchors the temperature of the droplet to $\hat{T}_{\infty}$ more strongly than the smaller conductivity of PTFE. Since vapour saturation is an increasing function of temperature, a warmer droplet has a greater vapour concentration at its free surface. Consequently, evaporation is faster for a droplet on a more conductive substrate. Figure 3.4 captures all of the same qualitative behaviour as figure 4 of Ait Saada *et al.* [5].

To determine the quantitative agreement between the present results and the results obtained by Ait Saada *et al.* [5], we compare the solutions for the profiles of temperature, vapour concentration and flux. Ait Saada *et al.* [5] only presented results for the choice of $n = 4$ in equation (2.52). We also obtain the corresponding results for $n = 0$ and $n = 1$. Doing this allows us to highlight the different results obtained by the thermally-decoupled model ($n = 0$) and the thermally-coupled model ($n > 0$).

Figure 3.5 shows numerically evaluated solutions for temperature, vapour concentration, and flux profiles for a droplet of water with contact angle $\hat{\theta} = 1.361$ and contact radius $\hat{R} = 1.86$ mm evaporating into air with ambient temperature $\hat{T}_{\infty} = 298.15$ K and thermal conductivity $\hat{k}^{\mathrm{a}} = \hat{k}^{\mathrm{air}} = 0.026$ W m^{-1} K^{-1} on an infinitely conducting substrate $\hat{k}^{\mathrm{s}} \to \infty$ W m^{-1} K^{-1}, a PTFE substrate $\hat{k}^{\mathrm{s}} = 0.25$ W m^{-1} K^{-1}, and a perfectly insulating substrate $\hat{k}^{\mathrm{s}} = 0$ W m^{-1} K^{-1}. Column [(a), (d), (g)] is obtained using $n = 0$ in equation (2.52), likewise column [(b), (e), (h)] is obtained using $n = 1$, and column [(c), (f), (i)] is obtained using $n = 4$.

Figures 3.5(a)–(c) show the temperature profiles on the free surface of the droplet and the upper surface of the substrate. Figures 3.5(a)–(c) show that, for all choices of n, as $\hat{k}^{\mathrm{s}}$ increases the evaporative cooling of the free surface decreases. By comparing figures 3.5(a)–(c) we see that the thermally-decoupled model shown in (a) predicts greater evaporative cooling as $\hat{k}^{\mathrm{s}}$ decreases than the thermally-coupled model shown in (b),

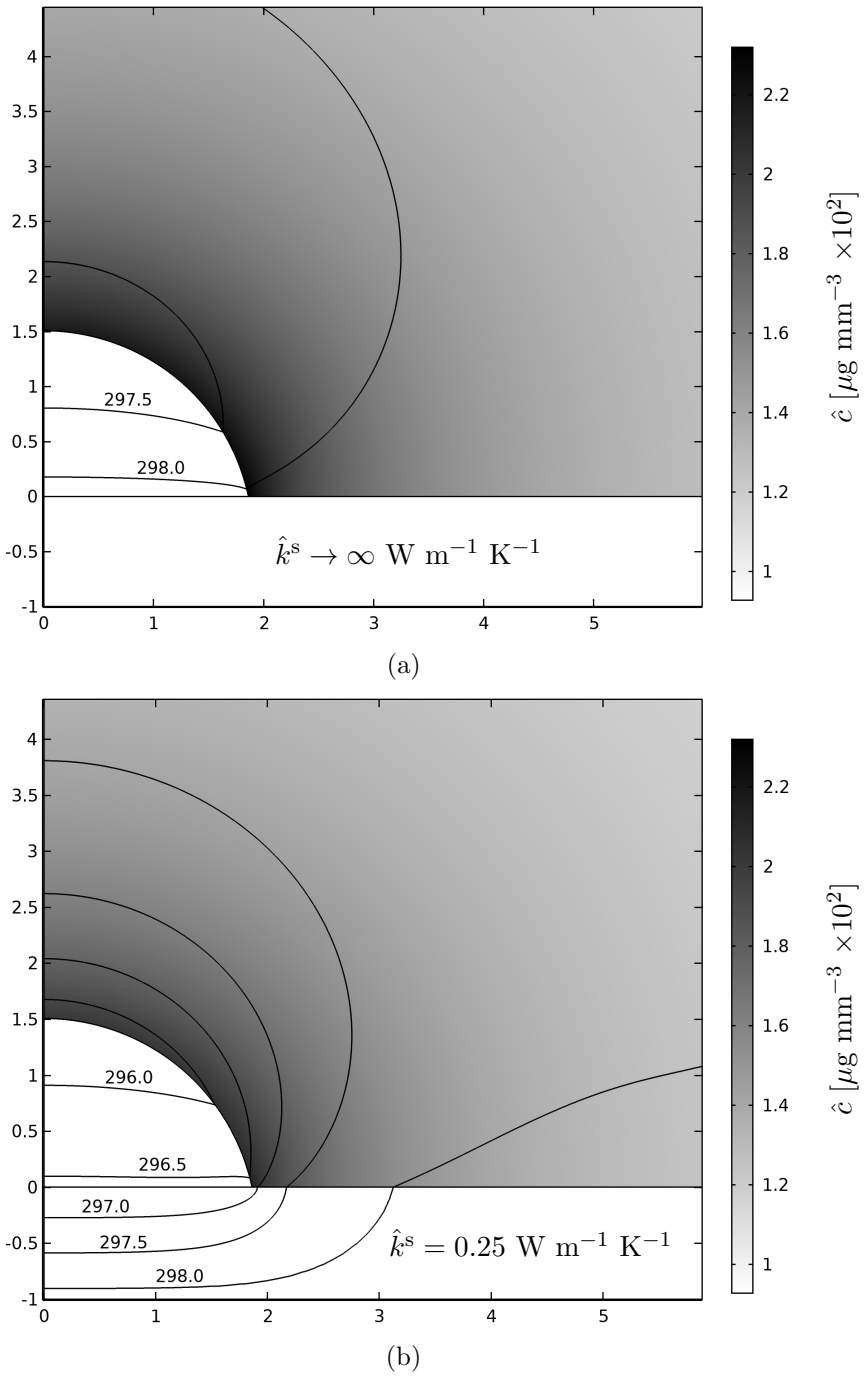

Figure 3.4: Vapour concentration $\hat{c}$ for a droplet of water with contact angle $\hat{\theta} = 1.361$ and contact radius $\hat{R} = 1.86$ mm evaporating into air with $\hat{c}_\infty = 0.4\hat{c}_{\mathrm{sat}}(\hat{T}_\infty)$ and $\hat{T}_\infty = 298.15$ K on (a) an infinitely conducting substrate ($\hat{k}^{\mathrm{s}} \to \infty$ W m^{-1} K^{-1}) and (b) a PTFE substrate ($\hat{k}^{\mathrm{s}} = 0.25$ W m^{-1} K^{-1}). Also shown are temperature contours $\hat{T}$, $\hat{T}^{\mathrm{s}}$ and $\hat{T}^{\mathrm{a}}$ in K.

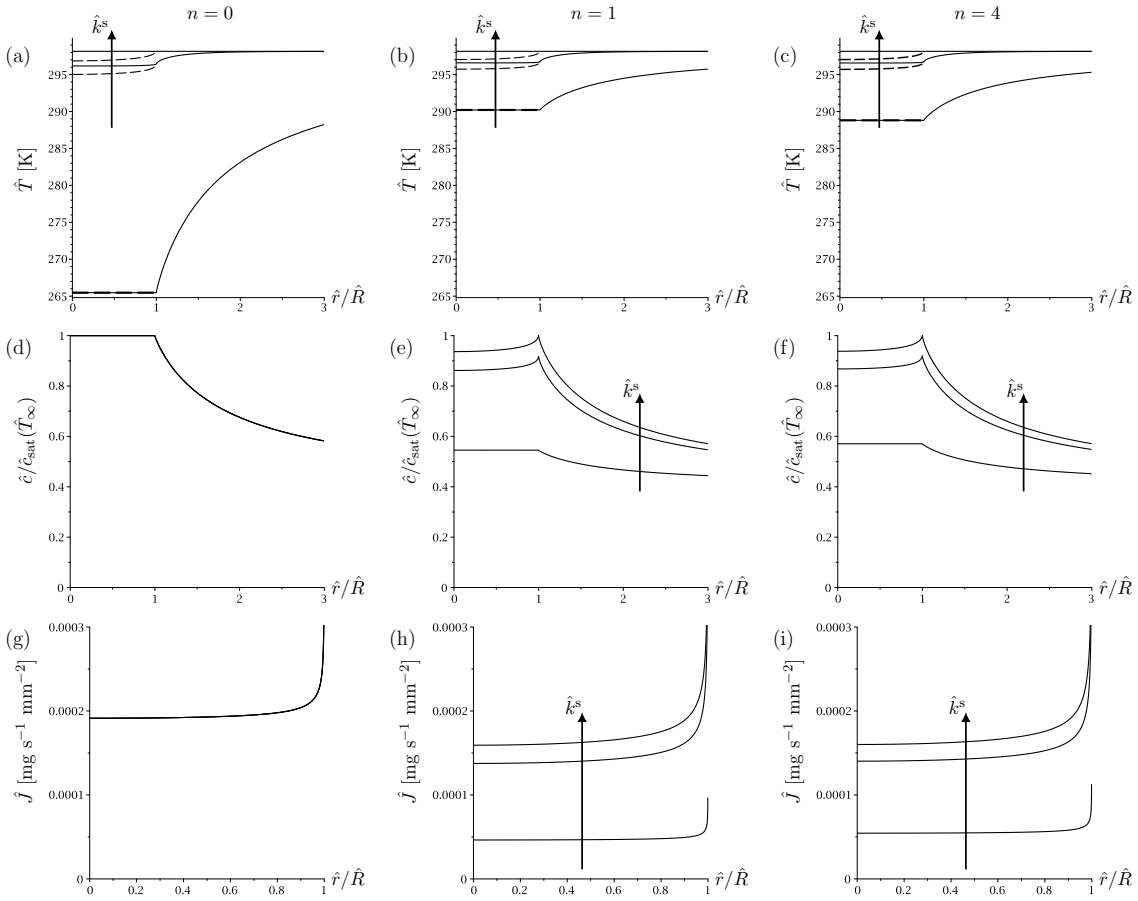

Figure 3.5: Numerically evaluated solutions for temperature, vapour concentration and flux profiles, for a droplet of water with contact angle $\hat{\theta} = 1.361$ and contact radius $\hat{R} = 1.86$ mm evaporating into air with $\hat{c}_\infty = 0.4\hat{c}_{\text{sat}}(\hat{T}_\infty)$ and $\hat{T}_\infty = 298.15$ K on an infinitely conducting substrate $\hat{k}^s \to \infty$ W m^{-1} K^{-1}, a PTFE substrate $\hat{k}^s = 0.25$ W m^{-1} K^{-1}, and a perfectly insulating substrate $\hat{k}^s = 0$ W m^{-1} K^{-1}. Column [(a), (d), (g)] is obtained using $n = 0$ in equation (2.52), likewise column [(b), (e), (h)] is obtained using $n = 1$ and column [(c), (f), (i)] is obtained using $n = 4$. In figures (a)–(c) dashed curves show the temperature along the free surface of the droplet and solid curves show the temperature along the substrate upper surface. In figures (d)–(f) the concentration profile is taken along the free surface of the droplet for $\hat{r} < \hat{R}$, and along the substrate upper surface for $\hat{r} > \hat{R}$. Arrows indicate the direction of increasing $\hat{k}^s$.

(c). Furthermore, we see more cooling for $n = 4$ than for $n = 1$. This is caused by the increased flux for $n = 4$, which in turn is because $\hat{c}_{\text{sat}}$ is larger for $n = 4$ than for $n = 1$ over the temperature range we are concerned with.

Figures 3.5(d)–(f) show the scaled vapour concentration profiles on the atmosphere-droplet interface and the atmosphere-substrate interface. Since the vapour concentration is decoupled from the temperature solution for the thermally-decoupled model, all of the concentration profiles are identical in figure 3.5(d). Figures 3.5(b), 3.5(c), 3.5(e) and 3.5(f) show that for $\hat{r} < \hat{R}$ the temperature of the free surface, and also the vapour concentration, increase monotonically to a maximum value at $\hat{r} = \hat{R}$. For $\hat{r} > \hat{R}$ the temperature of the substrate increases towards $\hat{T}_\infty$ and the vapour concentration decreases towards $\hat{c}_\infty = 0.4\hat{c}_{\text{sat}}(\hat{T}_\infty)$ as $\hat{r} \to \infty$. Figure 3.5(d) shows that the thermally-decoupled model gives $\hat{c}_{\text{sat}} = \hat{c}_{\text{sat}}(\hat{T}_\infty) =$ constant across the entire free surface of the droplet. However, figures 3.5(e) and 3.5(f) show that, in general, $\hat{c}_{\text{sat}} \leq \hat{c}_{\text{sat}}(\hat{T}_\infty)$ for the thermally-coupled model of evaporation, with $\hat{c}_{\text{sat}}(\hat{T}) = \hat{c}_{\text{sat}}(\hat{T}_\infty)$ only at $\hat{r} = \hat{R}$ when $\hat{k}^{\text{s}} \to \infty$. In particular, figures 3.5(e) and 3.5(f) show that $\hat{c}_{\text{sat}}(\hat{T}_\infty)$ increases with $\hat{k}^{\text{s}}$.

Figures 3.5(g)–(i) show the flux profiles along the free surface of the droplet. Specifically, figures 3.5(g)–(i) show that for all values of $\hat{k}^{\text{s}}$ the flux is singular at the contact line. Again, since the flux is de-coupled from the temperature solution when $n = 0$, all of the flux profiles are identical in figure 3.5(g). Figures 3.5(h) and 3.5(i) show that for the thermally-coupled model $\hat{J}$ increases as $\hat{k}^{\text{s}}$ increases. This is because increasing $\hat{k}^{\text{s}}$ decreases the magnitude of the cooling, and thus increases $\hat{c}_{\text{sat}}(\hat{T})$, on the free surface of the droplet.

By comparing figure 3.5(g) and figures 3.5(h) and 3.5(i) we see that the thermally-decoupled model ($n = 0$) predicts greater flux than the thermally coupled model ($n > 0$) for all $\hat{k}^{\text{s}}$. This is because $\hat{c}_{\text{sat}}(\hat{T})$ is larger for $n = 0$ than for $n > 0$.

We compare the present results for $n = 4$ with the results obtained by Ait Saada *et al.* [5]. Comparing the present figure 3.5(c) and figure 5(b) of Ait Saada *et al.* [5], we see near-identical results for the temperature profiles. Both results show about a

9 K difference in the cooling of the wetted substrate between $\hat{k}^{\mathrm{s}} \to \infty$ and $\hat{k}^{\mathrm{s}} = 0$. By carefully inspecting figure 4 of Ait Saada *et al.* [5], we observe a similar vapour profile to that shown in figure 3.5(f). Comparing the present figure 3.5(i) and figure 7(b) of Ait Saada *et al.* [5] we also see near-perfect agreement between the present flux profiles and those obtained by Ait Saada *et al.* [5] for droplets of water evaporating on substrates of varying thermal conductivity.

3.3.2 Validating the solution for the rate of change of the volume of a droplet

Using the numerically calculated flux we obtain the instantaneous rate of change of the volume of a droplet. Table 3.2 shows the rate of change of the volume of a droplet corresponding to the results obtained in figure 3.5. Table 3.2 also shows the numerical values of the analytical solutions for the thermally-decoupled model, as obtained, for example, by Stauber *et al.* [143] using their equation (10), and the numerical results obtained by Ait Saada *et al.* [5].

Comparing the present $n = 0$ results and the Stauber *et al.* [143] results shows that the thermally-decoupled model numerical results presented here are within 0.3% of the corresponding analytical values.

Table 3.2 clearly shows that the thermally-coupled model results depend on the substrate conductivity. We see that increasing the conductivity of the substrate gives a higher evaporation rate. Comparing the present $n = 0$ results and the present $n = 1$ and $n = 4$ results we see that, in all cases, the thermally-decoupled model gives larger rates of change of the volume of the droplet than the thermally-coupled model.

Table 3.2 also shows the sensitivity of the results to the choice of n in equation (2.52) for the thermally-coupled model solutions. Comparing the $\hat{k}^{\mathrm{s}} \to \infty$ results for $n = 1$ and $n = 4$, we do not see any difference. This is because the highly conducting substrate reduces the cooling of the droplet, and thus the thermally-coupled model is not sensitive to the choice of n in this case. However, we see that as we decrease the conductivity of

$\hat{k}^{\mathrm{s}}$ [W m^{-1} K^{-1}]		0	0.25	∞
$-\frac{\mathrm{d}\hat{V}}{\mathrm{d}\hat{t}}$ mm^3 s^{-1}	$n = 0$	0.00372	0.00372	0.00372
	Stauber *et al.* [143]	0.00371	0.00371	0.00371
	$n = 1$	8.9780×10^{-4}	0.00298	0.00347
	$n = 4$	0.00105	0.00301	0.00347
	Ait Saada *et al.* [5]	0.001087	0.003	0.003435

Table 3.2: Summary of instantaneous rates of change of the volume of the droplet $-\mathrm{d}\hat{V}/\mathrm{d}\hat{t}$ for the droplets discussed in section 3.3.1.

the substrate the sensitivity to n increases.

3.3.3 Validating the solution for the droplet lifetime

Using the numerically obtained rate of change of the volume of the droplet and the time-stepping method described in section 3.2.4 we obtain the evolution of the rate of change of the volume of the droplet, and hence the droplet lifetimes. Figure 3.6 shows the present numerically evaluated rate of change of the volume of the droplet $\mathrm{d}\hat{V}/\mathrm{d}\hat{t}$ as it evolves in time for a droplet of water evaporating into air on a PTFE substrate ($\hat{k}^{\mathrm{s}} = 0.025$ W m^{-1} K^{-1}), initiated as described in section 3.3.1 (*i.e.* the present numerical results for a droplet initially identical to that as discussed by Ait Saada *et al.* [5], evaporating on a PTFE substrate) in each of the (a) CR and (b) CA modes of evaporation. From figure 3.6 we see that, for this particular droplet, $\hat{t}_{\mathrm{CR}} < \hat{t}_{\mathrm{CA}}$. We also see from figure 3.6 (a) that as $\hat{t} \to \hat{t}_{\mathrm{CR}}$ the rate of change of the volume of the droplet approaches the non-zero rate of change of the volume of a droplet corresponding to a thin droplet ($\hat{\theta} \ll 1$). Likewise, from figure 3.6 (b) we see that as $\hat{t} \to \hat{t}_{\mathrm{CA}}$ the rate of change of the volume of the droplet approaches zero. Note that in both cases the time-stepping method terminates (very slightly) before reaching these limits due to the numerically insignificant volume of droplet remaining.

Here we compare the lifetimes we have numerically calculated for the thermally-decoupled model with the analytical lifetime expressions given by Stauber *et al.* [143] and the numerically calculated lifetimes given by Ait Saada *et al.* [5].

Stauber *et al.* [143] gave analytical expressions for the thermally-decoupled model life-

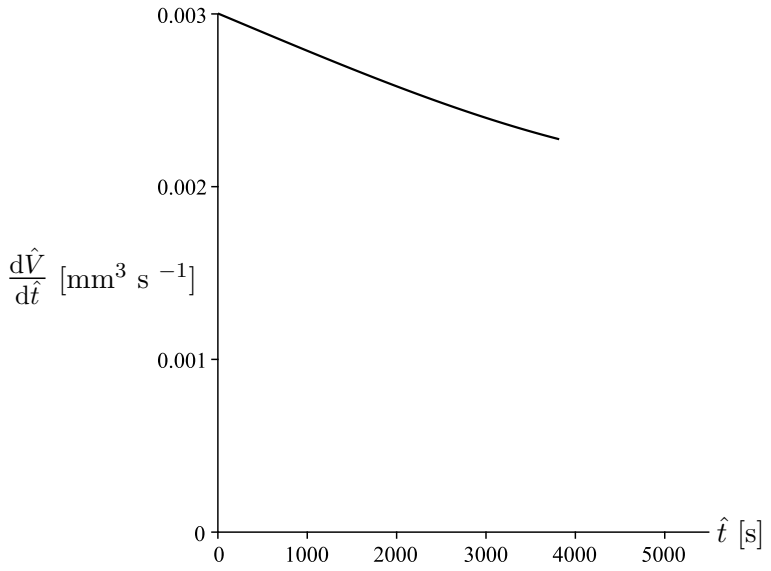

(a)

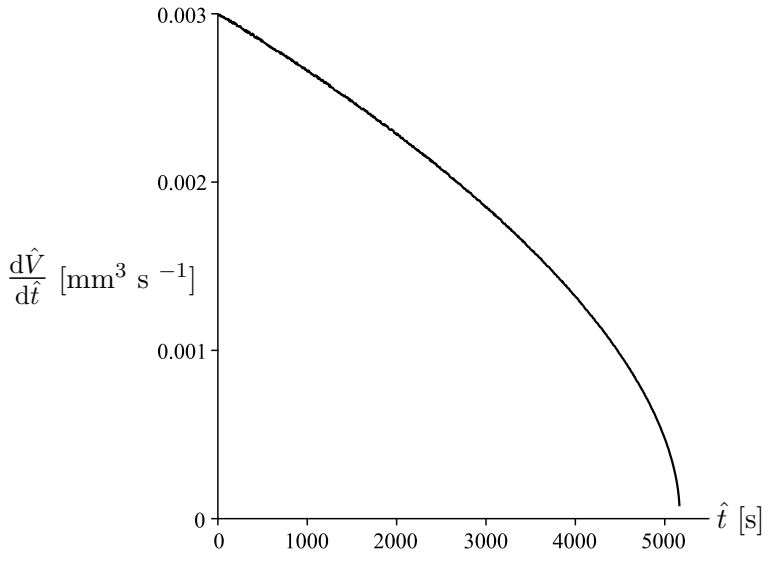

(b)

Figure 3.6: The present numerically evaluated rate of change of the volume of the droplet $d\hat{V}/d\hat{t}$ as it evolves in time for a droplet of water evaporating into air on a PTFE substrate ($\hat{k}^s = 0.025$ W m^{-1} K^{-1}), initiated as described in section 3.3.1, in each of the (a) CR and (b) CA modes of evaporation.

	t_{CR}	
$\hat{k}^{\mathrm{s}}$ [W m^{-1} K^{-1}]	0.25	∞
Ait Saada *et al.* [5]	3780 s	3300 s
Present $n = 4$	3834 s	3369 s
Stauber *et al.* [143]	3219 s	

	t_{CA}	
$\hat{k}^{\mathrm{s}}$ [W m^{-1} K^{-1}]	0.25	∞
Ait Saada *et al.* [5]	4750 s	4000 s
Present $n = 4$	5167 s	4333 s
Stauber *et al.* [143]	4034 s	

Table 3.3: Summary of CR and CA lifetimes for a droplet of water with initial radius $\hat{R} = 1.86$ mm and contact angle $\hat{\theta} = 1.361$.

times $\hat{t}_{\mathrm{CR}}$ and $\hat{t}_{\mathrm{CA}}$ in their equations (3.2) and (3.3), respectively. Evaporative cooling means that $\hat{T} \leq \hat{T}_{\infty}$ across the free surface of the droplet in both the thermally-coupled model and the thermally-decoupled model. However, the cooling of the droplet does not decrease the vapour concentration on the free surface of the droplet in the thermally-decoupled model. Consequently, the lifetimes in the thermally-decoupled model act as a lower bound for the lifetimes in the thermally-coupled model.

We also compare the lifetime values obtained by Ait Saada *et al.* [5], who used $n = 4$ in equation (2.52), with the present results. Table 3.3 summarises the lifetime data for $\hat{\theta}_0 = 1.361$. Table 3.3 shows that the CR and CA lifetimes obtained by Ait Saada *et al.* [5] are up to 2% and 8% shorter than corresponding present results, respectively. In particular, the lifetime of the CA mode obtained by Ait Saada *et al.* for a droplet evaporating on an infinitely conducting substrate is even less than that for the corresponding thermally-decoupled model. Since this is evidently impossible, this suggests problems with the method Ait Saada *et al.* [5] used to obtain the droplet lifetimes.

To find the source of the disagreement between the present results for the CA mode lifetimes and the results presented by Ait Saada *et al.* [5] we compare the different time-stepping methods used. The present time-stepping method given by equations (3.5) and (3.6) is verified by comparing with the analytical results given by Stauber *et al.* [143] for the thermally-decoupled model. As previously described, the present numerical results are within 0.5% of the analytical predictions.

Ait Saada *et al.* [5] obtained their time-step $\Delta\hat{t}$ using their equation (12), namely

$$\Delta\hat{t} = \frac{\mathrm{d}\hat{t}}{\mathrm{d}\hat{V}}\Delta\hat{V}, \tag{3.7}$$

where $\Delta\hat{V}$ is a fixed change in droplet volume. From equation (2.46) we find

$$\frac{\mathrm{d}\hat{V}}{\mathrm{d}\hat{t}} \to -\frac{2\pi}{\hat{\rho}}\int_0^{\hat{R}(\hat{t})} \hat{J}\hat{r}\mathrm{d}\hat{r} \quad \text{as } \hat{\theta} \to 0. \tag{3.8}$$

Thus, in the CR mode, $\Delta\hat{t}$ remains well defined as $\hat{t} \to \hat{t}_{\mathrm{CR}}$ since $\hat{R}$ is constant. However, in the CA mode, equation (2.46) shows that

$$\frac{\mathrm{d}\hat{V}}{\mathrm{d}\hat{t}} \to 0 \quad \text{as } \hat{R} \to 0. \tag{3.9}$$

Thus, in the CA mode $\Delta\hat{t} \to \infty$ as $\hat{t} \to \hat{t}_{\mathrm{CA}}$. Therefore, equation (3.7) is not suitable for obtaining time-steps in the CA mode of evaporation. Ait Saada *et al.* [5] justify their time-stepping method in their figure 3, where they compare their numerical results with the experimental results of Song *et al.* [140], Hu and Larson *et al.* [66], and Dunn *et al.* [51]. Although Ait Saada *et al.* [5] show good agreement of their model for the CR mode of evaporation, no verification is given for the CA mode. We therefore suggest that the principal source of disagreement between the lifetimes given by Ait Saada *et al.* [5] and the present results is the time-stepping method, and that the time-stepping method used by Ait Saada *et al.* [5] is less reliable than the present method. To verify this suggestion, however, it would be necessary to implement the method used by Ait Saada *et al.* [5] within the present numerical method and compare the behaviour as $\hat{V} \to 0$ directly.

3.3.4 Comparison with the predictions of the Dunn model

To explain the differences between the thermally-coupled model and the Dunn model described in section 2.3.2 we compare the results obtained by Dunn *et al.* [51] with the results of own calculations using the Dunn model and the thermally-coupled model.

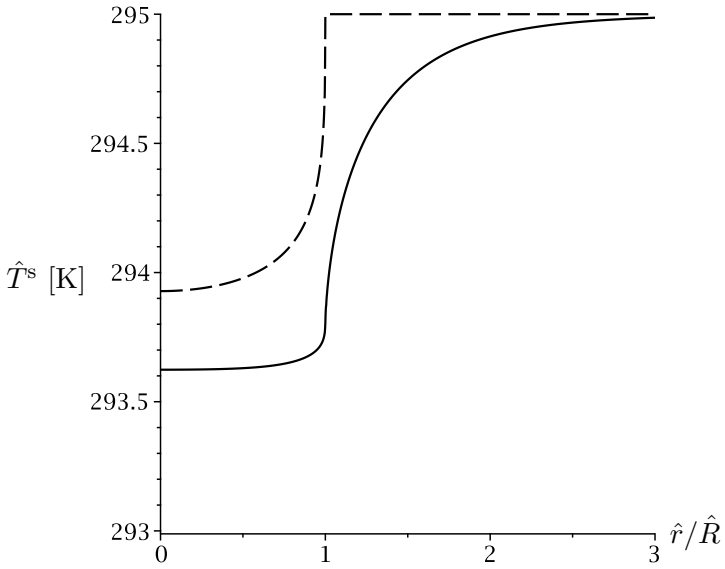

Figure 3.7: Typical numerically evaluated temperature profile on the upper surface of the substrate. The dashed curve shows the results obtained using the Dunn model. The solid curve shows the results obtained using the present thermally-coupled model.

Figure 3.7 shows a typical numerically evaluated temperature profile on the upper surface of the substrate. Figure 3.7 shows that, by assumption, when using the Dunn model the temperature of the upper surface of the substrate reaches $\hat{T}_\infty$ at $\hat{r} = \hat{R}$. However, when using the thermally-coupled model the substrate temperature does not reach $\hat{T}_\infty$ at the contact line, but instead tends to $\hat{T}_\infty$ only as $\hat{r} \to \infty$. Consequently, the wetted surface of the substrate is warmer when using the Dunn model than when using the thermally-coupled model. This makes the droplet warmer, and hence evaporate faster.

Using the results obtained by Dunn *et al.* [51] we compare the rates of change of the volume of the droplet predicted by the Dunn model and by the thermally-coupled model. Figure 3.8 summarises the numerically calculated rate of change of the volume of the droplet for droplets of acetone, methanol and water on substrates of aluminium, titanium, Macor and PTFE. Figure 3.8(a) shows the values given in figure 4 of Dunn *et al.* [51], obtained using the Dunn model. Figure 3.8(b) shows our recalculated values

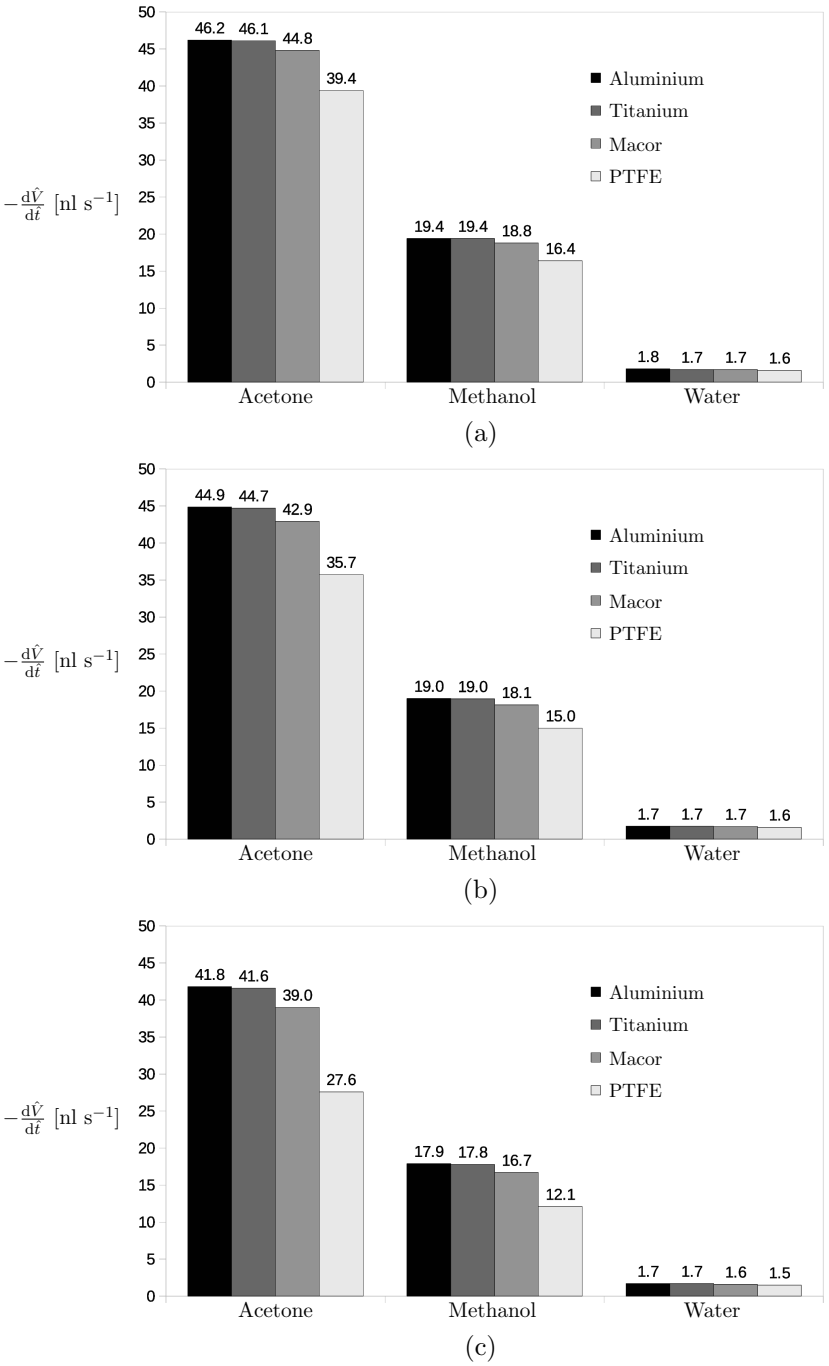

Figure 3.8: Bar charts summarising the numerically calculated evaporation rates for droplets of acetone, methanol and water evaporating on substrates of aluminium, titanium, Macor and PTFE. (a) Values quoted in figure 4 of Dunn *et al.* [51], obtained using the Dunn model. (b) Present values obtained using Dunn model and the present mesh. (c) Corresponding values obtained using the present thermally-coupled model described in section 2.4.

obtained using the Dunn model and the present mesh. Figure 3.8(c) shows the corresponding values obtained using the thermally-coupled model described in section 2.4. In general, figures 3.8(a)–(c) show the same trend, namely that the evaporation rate decreases with substrate conductivity. The difference between the evaporation rates given by figures 3.8(a) and 3.8(b) is presumably due to the different meshes used. Figure 3.8 shows that in almost every case the Dunn model predicts a greater evaporation rate than the thermally-coupled model. The difference between the predicted values is greatest for the cases with the most evaporative cooling, *i.e.* the cases with lower $\hat{k}^{\mathrm{s}}$.

3.4 Results for the full range of initial contact angles

So far we have validated the implementation of our numerical method against the results of Ait Saada *et al.* [5]. However, Ait Saada *et al.* [5] only considered a single initial contact angle, namely $\hat{\theta}_0 = 1.361$. We now investigate the effects that different thermophysical properties have on droplets with the full range of initial contact angles.

We first present the quasi-steady solutions for vapour concentration and temperature. We then present lifetime results for droplets with initial contact angles in the full range $0 \leq \hat{\theta}_0 \leq \pi$ for a variety of different substrates. For the remainder of this chapter we use the values of the physical parameters given by Dunn *et al.* [51], *i.e.* the values presented in tables 2.1 and 2.2.

3.4.1 Dependence of solutions for $\hat{c}$, $\hat{T}$ and $\hat{J}$ on $\hat{k}^{\mathrm{s}}$ and $\hat{\theta}$

Firstly, we discuss the behaviour of the quasi-steady solution for the coupled vapour concentration and temperature. In particular, we see how $\hat{c}$ and $\hat{T}$ vary with $\hat{k}^{\mathrm{s}}$ and $\hat{\theta}$. We have already seen from figure 3.4 that decreasing the thermal conductivity of the substrate allows the substrate to cool more, which means the vapour concentration is lower on the free surface of the droplet. Figure 3.9 shows the vapour concentration $\hat{c}$

for a droplet of water with contact angle (a) $\hat{\theta} = 2\pi/3$ and (b) $\hat{\theta} = 5\pi/6$, and contact radius $\hat{R} = 0.5$ mm evaporating into air with $\hat{c}_\infty = 0.4\hat{c}_{\rm sat}(\hat{T})$ and $\hat{T}_\infty = 295$ K on a PTFE substrate ($\hat{k}^{\rm s} = 0.25$ W m^{-1} K^{-1}). Figure 3.9 also shows the temperature contours of $\hat{T}$, $\hat{T}^{\rm s}$ and $\hat{T}^{\rm a}$. Figure 3.9 shows that, given the same contact radius, a droplet with a larger contact angle is cooler than a droplet with a smaller contact angle. This is because a droplet with a larger contact angle is taller, so the free surface of the droplet is further from the lower surface of the substrate, thus reducing the temperature anchoring effects of the substrate.

As in figure 3.5, figure 3.10 shows numerically evaluated solutions for temperature, vapour concentration, and flux profiles for a droplet of water with contact angle $\hat{\theta} = 5\pi/6$ and contact radius $\hat{R} = 0.5$ mm evaporating into air with ambient temperature $\hat{T}_\infty = 295$ K and thermal conductivity $\hat{k}^{\rm a} = \hat{k}^{\rm air} = 0.026$ W m^{-1} K^{-1} on an infinitely conducting substrate $\hat{k}^{\rm s} \to \infty$ W m^{-1} K^{-1}, a PTFE substrate $\hat{k}^{\rm s} = 0.25$ W m^{-1} K^{-1}, and a perfectly insulating substrate $\hat{k}^{\rm s} = 0$ W m^{-1} K^{-1}. Note that, since the free surface of the droplet is overhanging for $\hat{\theta} > \pi/2$, the profiles for $\hat{T}$, $\hat{c}$ and $\hat{J}$ on the free surface are double-valued. Column [(a), (d), (g)] is obtained using $n = 0$ in equation (2.52), likewise column [(b), (e), (h)] is obtained using $n = 1$ and column [(c), (f), (h)] is obtained using $n = 4$. Since the droplet height is double-valued for $\hat{r} > \hat{R}$, the temperature, vapour concentration and flux profiles are also double-valued for $\hat{r} > \hat{R}$.

Figures 3.10(a)–(f) show much the same behaviour as shown in figures 3.5(a)–(f). Specifically, we again see that the free-surface temperature, and thus the vapour concentration, increases to a maximum value at the contact line of the droplet.

Figure 3.10(g) shows the flux profile calculated using the thermally-decoupled model, where the flux is zero at the contact line. This is because, since the vapour concentration is uniform along the free surface of the droplet, the acute corner region near the contact line becomes saturated with vapour, and so the droplet cannot evaporate from the contact line. Figures 3.10(h) and 3.10(i) show that, as in figure 3.5, for $\hat{k}^{\rm s} \neq 0$ the flux is singular at the contact line. This is because the vapour concentration is maximum in

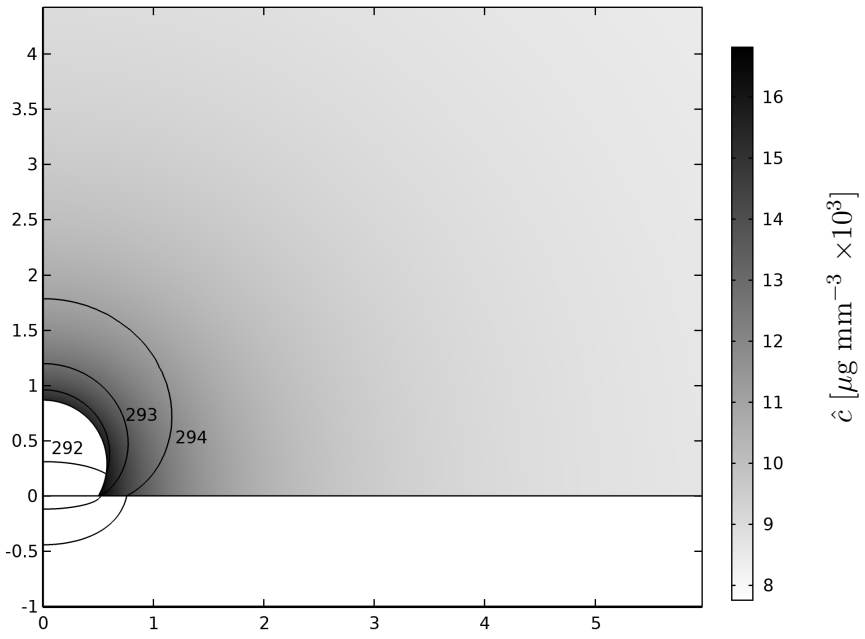

(a)

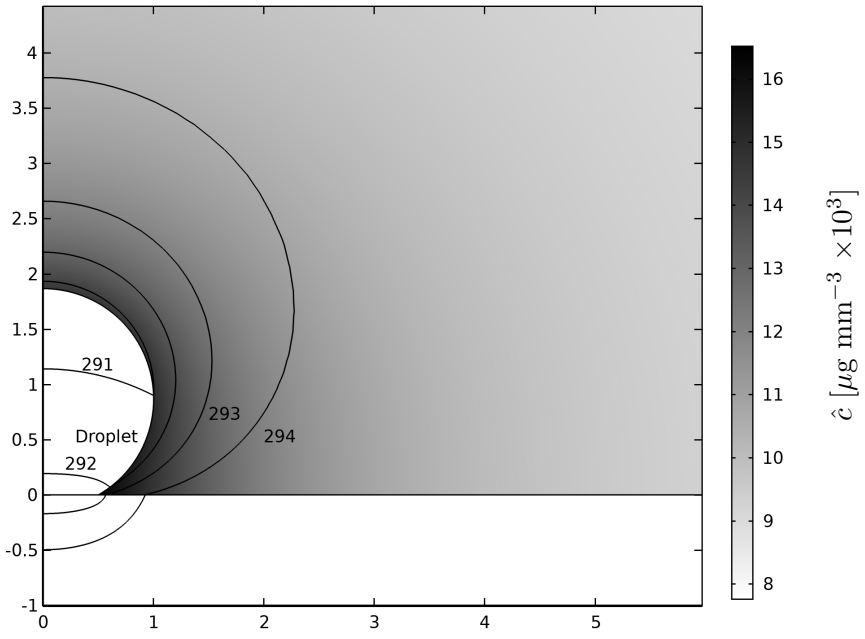

(b)

Figure 3.9: Vapour concentration $\hat{c}$ for a droplet of water with contact angle (a) $\hat{\theta} = 2\pi/3$ and (b) $\hat{\theta} = 5\pi/6$, and contact radius $\hat{R} = 0.5$ mm evaporating into air with 40% humidity and $\hat{T}_\infty = 295$ K on a PTFE substrate ($\hat{k}^{\mathrm{s}} = 0.25$ W m^{-1} K^{-1}). Also shown are the temperature contours of $\hat{T}$, $\hat{T}^{\mathrm{s}}$ and $\hat{T}^{\mathrm{a}}$ in K.

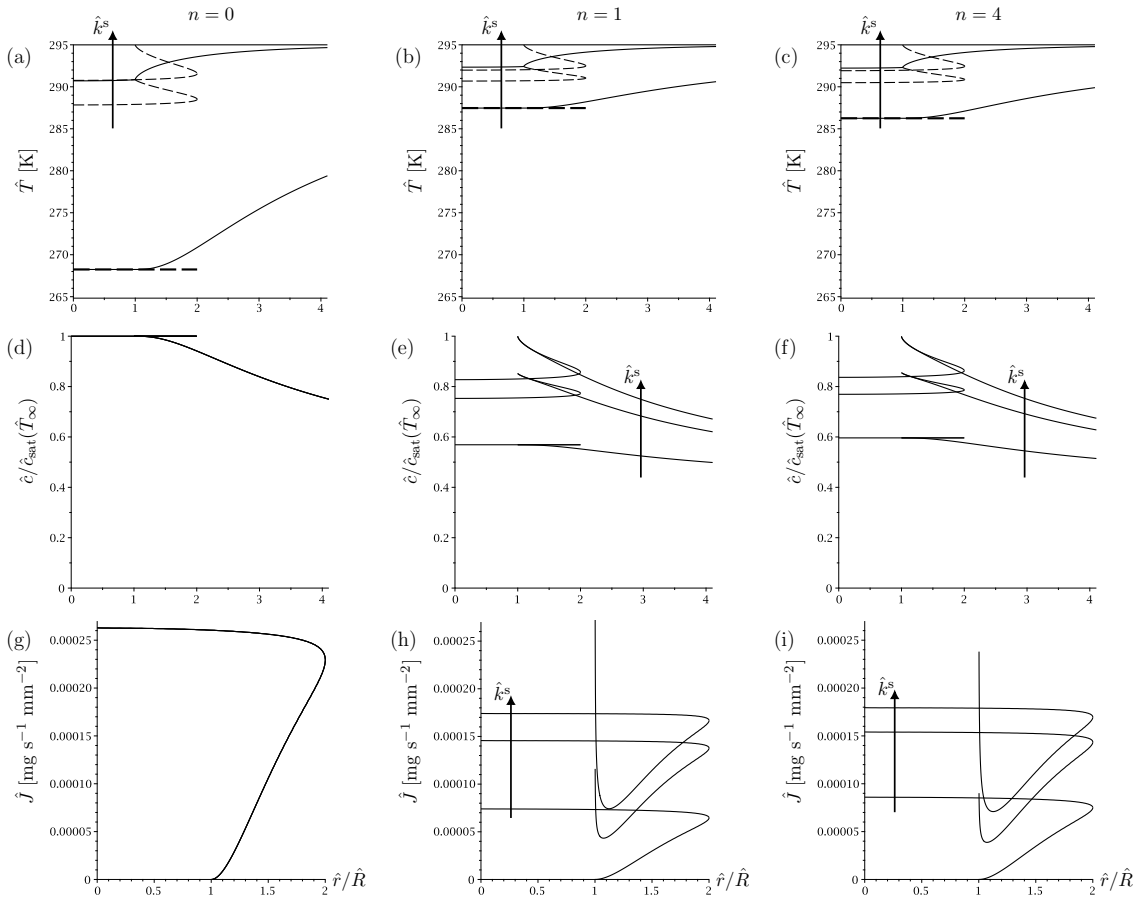

Figure 3.10: Numerically evaluated solutions for temperature, vapour concentration and flux profiles, for a droplet of water with contact angle $\hat{\theta} = 5\pi/6$ and contact radius $\hat{R} = 0.5$ mm evaporating on an infinitely conducting substrate $\hat{k}^s \to \infty$ W m^{-1} K^{-1}, a PTFE substrate $\hat{k}^s = 0.25$ W m^{-1} K^{-1} and a perfectly insulating substrate $\hat{k}^s = 0$ W m^{-1} K^{-1}. Column [(a), (d), (g)] is obtained using $n = 0$ in equation (2.52), likewise column [(b), (e), (g)] is obtained using $n = 1$ and column [(c), (f), (i)] is obtained using $n = 4$. In figures (a)–(c) dashed curves show the temperature along the free surface of the droplet and solid curves show the temperature along the upper surface of the substrate. In figures (d)–(f) the concentration profile is taken along the free surface of the droplet for $\hat{r} < \hat{R}$, and along the upper surface of the substrate for $\hat{r} > \hat{R}$. Arrows indicate the direction of increasing $\hat{k}^s$.

the acute corner region of the droplet, but decreases along the free surface of the droplet, allowing for the droplet to evaporate from the contact line. However, in contrast to figure 3.5, figures 3.10(h) and 3.10(i) show that for $\hat{k}^s = 0$ the flux at the contact line is apparently zero. This is because for $\hat{k}^s = 0$ the vapour concentration is again (nearly) uniform along the free surface of the droplet. As discussed in section 2.6 the

local behaviour near to the contact line of an evaporating droplet has been investigated by various authors using reduced forms of the thermally-coupled model. However, as we mention later in section 6.2.2, we are unaware of any investigations into the local behaviour near to the contact line using the full thermally-coupled model.

3.4.2 Dependence of solutions for $\hat{c}$, $\hat{T}$ and $\hat{J}$ on $\hat{k}^{\mathrm{a}}$

We have shown that the thermal conductivity of the substrate is an important factor in determining the temperature of the droplet. We are also interested in knowing the importance of the thermal conductivity of the atmosphere in determining the temperature of the droplet, particularly for droplets with very large contact angles ($\hat{\theta} \approx \pi$). We have chosen to investigate high contact angle droplets because these droplets have a small droplet-substrate interface, thus we expect the conductivity of the substrate to have less influence on the droplet lifetime than for low contact angle droplets with larger droplet-substrate interfaces.

We investigate the dependence of our numerical results on the thermal conductivity of the atmosphere $\hat{k}^{\mathrm{a}}$. We carry out these calculations for a droplet of water with high contact angle $\hat{\theta} = \pi - 0.1$ and contact radius $\hat{R} = 0.1$ mm, evaporating into atmospheres with all of the physical properties of air with $\hat{c}_{\infty} = 0.4\hat{c}_{\mathrm{sat}}(\hat{T}_{\infty})$ except for thermal conductivity, which we take to be $\hat{k}^{\mathrm{a}} = 0$, $\hat{k}^{\mathrm{a}} = \hat{k}^{\mathrm{air}}$ and $\hat{k}^{\mathrm{a}} \to \infty$. We carry out these calculations for an aluminium substrate and a PTFE substrate.

Figure 3.11 shows the numerically calculated results for the temperature, vapour concentration and flux on the free surface of a droplet evaporating into atmospheres of varying thermal conductivity.

Figure 3.11(a) shows that when $\hat{k}^{\mathrm{a}} = 0$ the results for $\hat{T}$ vary significantly with substrate conductivity $\hat{k}^{\mathrm{s}}$. Figures 3.11(b) and 3.11(c) show that as $\hat{k}^{\mathrm{a}}$ increases, $\hat{T}$ becomes less dependent on $\hat{k}^{\mathrm{s}}$. In the limit $\hat{k}^{\mathrm{a}} \to \infty$ we see that $\hat{T} \equiv \hat{T}_{\infty}$ on the free surface, independent of $\hat{k}^{\mathrm{s}}$. Figures 3.11(a)–(f) show that $\hat{c}$ behaves in a similar fashion to $\hat{T}$. This is because when $\hat{k}^{\mathrm{a}} \to \infty$ the temperature of the free surface of the droplet is

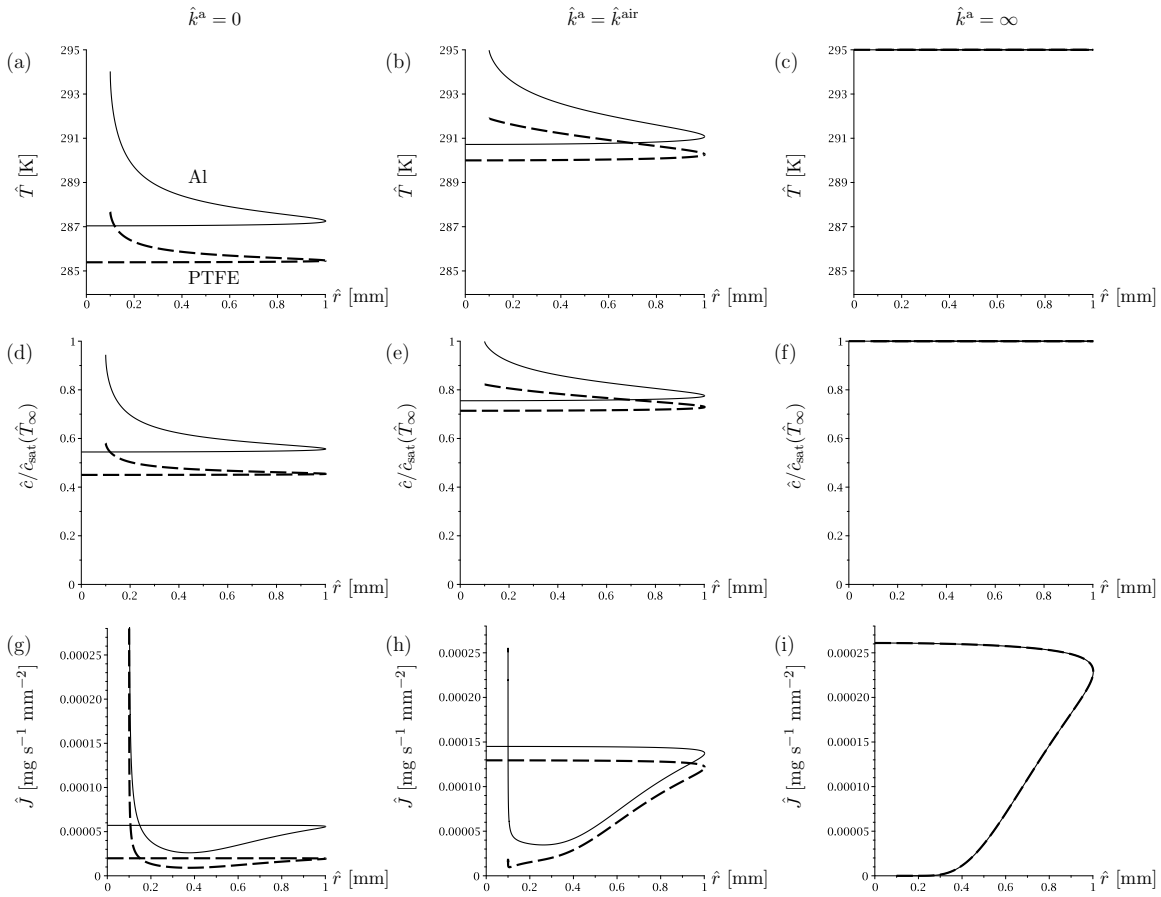

Figure 3.11: Numerically evaluated solutions for the free-surface temperature $\hat{T}$ (a)–(c), vapour concentration $\hat{c}$ (d)–(f) and flux $\hat{J}$ (g)–(i) profiles for a droplet of water with contact angle $\hat{\theta} = \pi - 0.1$ and contact radius $\hat{R} = 0.1$ mm evaporating on an aluminium substrate (solid curves) and a PTFE substrate (dashed curves), into atmospheres of varying thermal conductivity $\hat{k}^{\rm a}$. All of the results are obtained using $n = 1$ in equation (2.32).

entirely determined by (and equal to) the ambient far field atmospheric temperature $\hat{T}_\infty$. Figure 3.11(g) shows that when $\hat{k}^{\rm a} = 0$ we have $\hat{J} \to \infty$ at the contact line. Conversely, figure 3.11(i) shows that when $\hat{k}^{\rm a} \to \infty$ we have $\hat{J} \to 0$ at the contact line. As before, the nature of the flux at the contact line depends on the uniformity of $\hat{c}_{\rm sat}(\hat{T})$ on the free surface of the droplet.

Figure 3.11 shows that the evaporation rate is most strongly influenced by the substrate conductivity in the limit $\hat{k}^{\rm a} = 0$. On the other hand, in the limit $\hat{k}^{\rm a} \to \infty$, the evaporation rate approaches that of the thermally-decoupled model. This is because a

large thermal conductivity in the atmosphere creates a uniform temperature $\hat{T} = \hat{T}_\infty$ on the free surface of the droplet.

From figures 3.11[(b),(e),(h)] we note that even when the droplet-substrate interface is small, the temperature of the droplet, and hence the evaporation rate, still depends on the thermal conductivity of the substrate. This is because the temperature across the droplet-substrate interface is continuous, even for a point contact. As $\hat{k}^{\mathrm{s}}$ decreases the temperature of the droplet-substrate interface is increasingly determined by the evaporative cooling and the diffusion of heat through the atmosphere, and as $\hat{k}^{\mathrm{s}}$ increases this temperature is increasingly determined by the temperature of the lower surface of the substrate.

3.5 Droplet lifetimes

As before, we use the numerically obtained rate of change of the volume of the droplet $\hat{V}$ and the time-stepping method described in section 3.2.4 to obtain droplet lifetimes. In particular, we obtain droplet lifetimes for a variety of substrates with different thermal conductivities, for the full range of initial contact angles.

For a droplet with $\hat{R} > 0$ the volume, and hence the lifetime, of the droplet becomes singular as $\hat{\theta}_0 \to \pi^-$. As we did in section 2.4, we again follow Stauber *et al.* [143], and scale time with the basic timescale

$$\hat{\tau} = \frac{\hat{\rho}}{2\hat{D}(\hat{c}_{\mathrm{sat}}(\hat{T}_\infty) - \hat{c}_\infty)} \left(\frac{3\hat{V}_0}{2\pi}\right)^{2/3}, \tag{3.10}$$

to compare the lifetimes of droplets with $0 \leq \hat{\theta}_0 \leq \pi$. Using this timescale we have $\hat{t}_{\mathrm{CA}} = 1$ for any droplet with $\hat{\theta}_0 = \pi/2$ evaluated using the thermally-decoupled model of evaporation.

Figures 3.12 and 3.13 show, respectively, numerically evaluated scaled lifetimes in the CR and CA modes for droplets of water evaporating into 40% humidity air on various substrates of thickness $\hat{h}^{\mathrm{s}} = 1$ mm. We see that for the thermally-coupled model

the droplet lifetime decreases as $\hat{k}^{\mathrm{s}}$ increases. To obtain the lifetimes for $\hat{\theta}_0 = \pi$ we have linearly extrapolated from lifetime data with $\hat{\theta}_0 = \pi - 0.07$ (not shown) and $\hat{\theta}_0 = \pi - 0.1$.

Figure 3.12 shows that t_{CR} monotonically increases with $\hat{\theta}_0$ in the thermally-coupled model. However, this is not the case for the thermally-decoupled model for which t_{CR} begins to decrease after $\hat{\theta}_0 \approx 2.5830$, as discussed by Stauber *et al.* [143] and shown in figure 3.12. Figure 3.13 shows that t_{CA} monotonically increases with $\hat{\theta}_0$ for $\hat{k}^{\mathrm{s}} = 237$ W m^{-1} K^{-1} in the thermally-coupled model. However for $\hat{k}^{\mathrm{s}} = 0.25$ W m^{-1} K^{-1} and $\hat{k}^{\mathrm{s}} = 0.5$ W m^{-1} K^{-1} t_{CA} decreases as $\hat{\theta}_0 \to \pi$. Figure 3.13 also shows that for the thermally-decoupled model t_{CA} begins to decrease after $\hat{\theta}_0 = \pi/2$, as discussed by Stauber *et al.* [143]. Figure 3.13 shows us that, for $\hat{\theta}_0$ close to π, for poorly conducting substrates the thermally-coupled lifetime of the droplet decreases as $\hat{\theta}_0$ increases, as in the thermally-decoupled model. This is because, as we have previously discussed, as the conductivity of the substrate decreases, the vapour concentration on the free surface of the droplet becomes increasingly uniform. Thus, the thermally-coupled lifetime of the droplet as a function of $\hat{\theta}_0$ behaves qualitatively the same the thermally-decoupled lifetime.

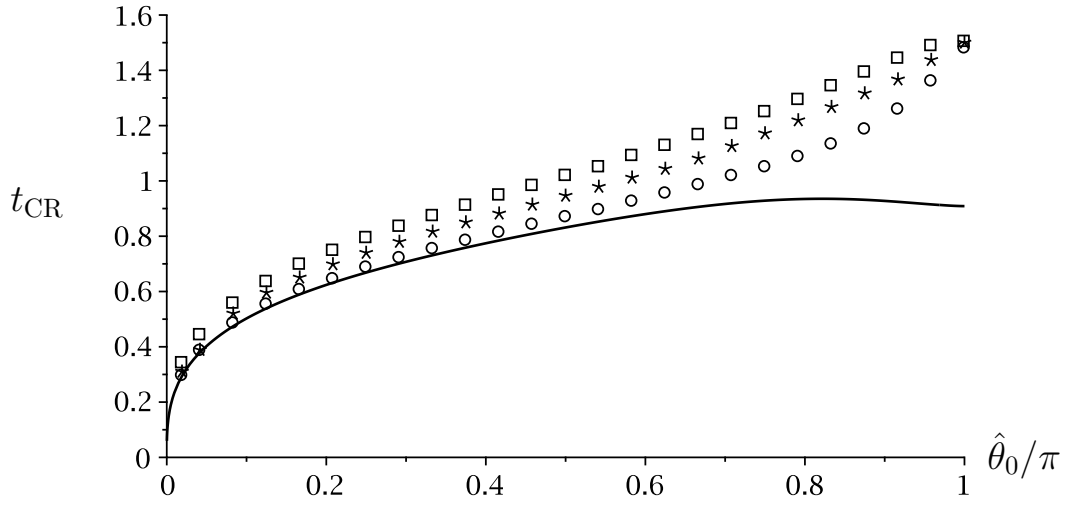

Figure 3.12: Numerically evaluated scaled lifetimes of the CR mode t_{CR} for droplets of water with initial radius $\hat{R} = 1$ mm evaporating into air with $\hat{c}_\infty = 0.4\hat{c}_{\mathrm{sat}}(\hat{T}_\infty)$ on aluminium $\circ$ ($\hat{k}^{\mathrm{s}} = 237$ W m^{-1} K^{-1}), HDPE $\star$ ($\hat{k}^{\mathrm{s}} = 0.50$ W m^{-1} K^{-1}) and PTFE $\square$ ($\hat{k}^{\mathrm{s}} = 0.25$ W m^{-1} K^{-1}) substrates of thickness $\hat{h}^{\mathrm{s}} = 1$ mm. Analytical results given by Stauber *et al.* [143] for the thermally-decoupled model shown as a solid line. The lifetimes are evaluated using physical parameters given in table 2.1.

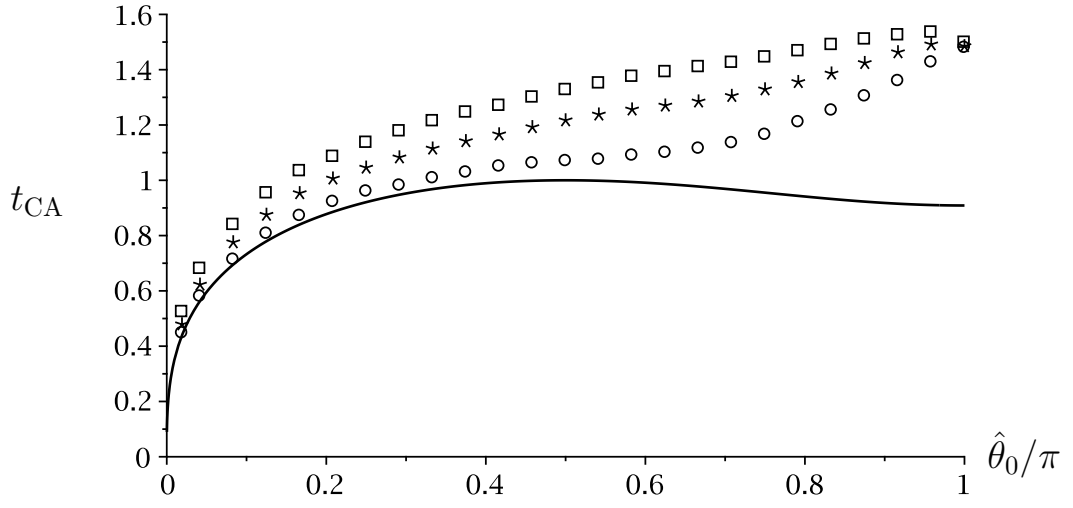

Figure 3.13: Numerically evaluated scaled lifetimes of the CA mode t_{CA} for droplets of water with initial radius $\hat{R} = 1$ mm evaporating into air with $\hat{c}_\infty = 0.4\hat{c}_{\mathrm{sat}}(\hat{T}_\infty)$ on aluminium $\circ$ ($\hat{k}^{\mathrm{s}} = 237$ W m^{-1} K^{-1}), HDPE $\star$ ($\hat{k}^{\mathrm{s}} = 0.50$ W m^{-1} K^{-1}) and PTFE $\square$ ($\hat{k}^{\mathrm{s}} = 0.25$ W m^{-1} K^{-1}) substrates of thickness $\hat{h}^{\mathrm{s}} = 1$ mm. Analytical results given by Stauber *et al.* [143] for the thermally-decoupled model shown as a solid line. The lifetimes are evaluated using physical parameters given in table 2.1.

From both figures 3.12 and 3.13 we see that in the limit $\hat{\theta}_0 \to \pi^-$ the lifetimes of the droplets are less dependent on the substrate conductivity than for $0 < \hat{\theta}_0 < \pi$. This is because in the limit $\hat{\theta}_0 \to \pi^-$ the droplet has a single point of contact with the substrate, thus the influence of the substrate conductivity is minimised. However, the substrate retains some influence due to the continuity of temperature through the droplet-substrate single point of contact and the conduction of heat through the atmosphere, as discussed earlier.

Figures 3.12 and 3.13 show that for any given $\hat{\theta}_0$ the difference between the lifetimes evaluated for aluminium ($\hat{k}^{\mathrm{s}} = 237$ W m^{-1} K^{-1}) and high-density polyethylene (HDPE) ($\hat{k}^{\mathrm{s}} = 0.5$ W m^{-1} K^{-1}) substrates is the same order of magnitude as the difference between the lifetimes evaluated for HDPE and PTFE ($\hat{k}^{\mathrm{s}} = 0.25$ W m^{-1} K^{-1}) substrates. This shows that the lifetimes of the droplets increase quickly as $\hat{k}^{\mathrm{s}}$ decreases. To illustrate this point further, we investigate the lifetimes calculated for a single value of $\hat{\theta}_0$ with $\hat{k}^{\mathrm{s}}$ spanning many decades of W m^{-1} K^{-1}. Figure 3.14 shows scaled lifetimes of droplets with $\hat{\theta}_0 = \pi/2$ in the CR mode and in the CA mode plotted as a function of $\hat{k}^{\mathrm{s}}$ using a log scale. Figure 3.14 shows that the lifetimes decrease monotonically as $\hat{k}^{\mathrm{s}}$ increases. In particular, the lifetimes are relatively sensitive to the conductivity of the substrate for $\hat{k}^{\mathrm{s}} < \hat{k} = 0.612$ W m^{-1} K^{-1}. However, the lifetimes quickly become independent of $\hat{k}^{\mathrm{s}}$ as $\hat{k}^{\mathrm{s}}$ increases.

3.6 Conclusions

In this chapter, we have carried out an in-depth investigation into the evaporation and lifetimes of sessile droplets. In particular, we have investigated the combined influences of initial contact angle $\hat{\theta}_0$ and substrate conductivity $\hat{k}^{\mathrm{s}}$ on droplet evaporation.

First, we verified the implementation of our numerical method against existing results obtained by previous authors. In general, a warmer droplet will evaporate faster than a cooler one, due to the increased vapour concentration at the free surface of the droplet. We have also found that substrates with higher thermal conductivity and droplets

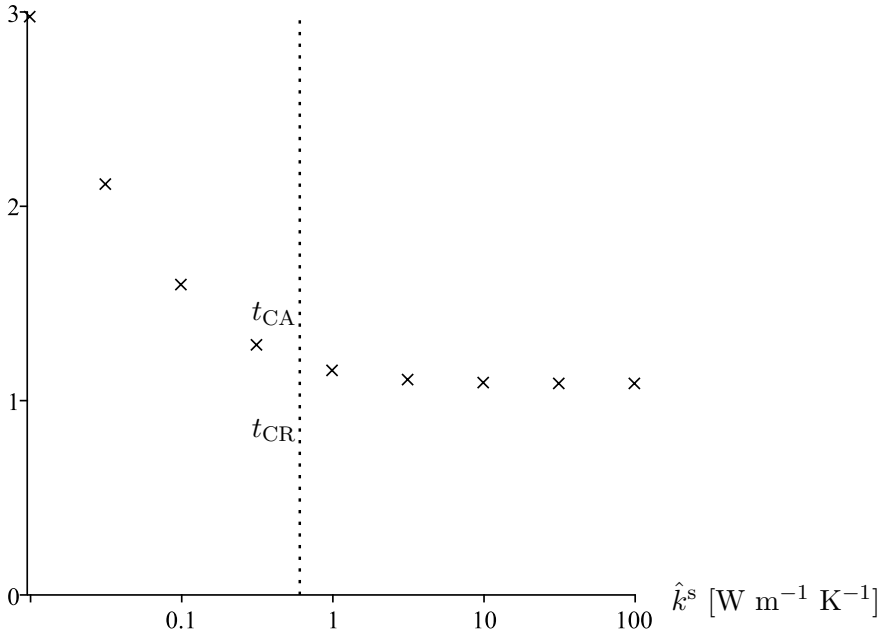

Figure 3.14: Scaled lifetimes of droplets with $\hat{\theta}_0 = \pi/2$ in the CR mode (circles) and the CA mode (crosses) plotted as a function of $\hat{k}^{\mathrm{s}}$ using a log scale. $\hat{k}^{\mathrm{s}} = \hat{k} = 0.604$ W m^{-1} K^{-1} is shown as a dotted line.

with lower contact angles are more effective at keeping the temperature across the free surface of the droplet close to the ambient value than substrates with lower thermal conductivity and droplets with higher contact angles. This means that, in general, the lifetime of a droplet will increase as $\hat{k}^{\mathrm{s}}$ decreases and as $\hat{\theta}$ increases. We have made these observations using the thermally-coupled model given in section 2.3.

In contrast to the thermally-coupled model, for thermally-decoupled model the vapour saturation is not influenced by evaporative cooling. These means that the vapour concentration at the free surface of the droplet is always at its maximum value, and thus the lifetimes obtained using the thermally-decoupled model are the lower bound of the lifetimes obtained using the thermally-coupled model. Using the thermally-coupled model we recover these lower bounds in the limits for which $\hat{T} \equiv \hat{T}_{\infty}$ on the free surface of the droplet, *i.e.* the limit $\hat{k}^{\mathrm{a}} \to \infty$ or the limit $\hat{k}^{\mathrm{s}} \to \infty$ and $\hat{k} \to \infty$.

We have also considered the Dunn mode. In this model, the temperature of the unwetted surface of the substrate does not change at all, which anchors the droplet to a

higher temperature than if the substrate was allowed to cool. The warmer droplet leads to a higher vapour concentration on the free surface of the droplet. This means that for a given set of physical parameters, the evaporation rate obtained using the Dunn model is greater than the corresponding result obtained using the thermally-coupled model.

We saw that it is important to consider the number of terms n in the approximation for $c_{\mathrm{sat}}(T)$ given by equation (2.52). Small values of n are acceptable for cases in which we can expect low amounts of evaporative cooling, i.e. for small $\hat{\theta}(0)$ and large values of $\hat{k}^{\mathrm{s}}$ or $\hat{k}^{\mathrm{a}}$. For large values of $\hat{\theta}(0)$ and small values of $\hat{k}^{\mathrm{s}}$, larger values of n should be used. We have also shown that it is important to take care when choosing a timestepping method. In particular we have shown that the present timestepping method is more reliable than the timestepping method used by Ait Saada *et al.* [5].

In general, we found that substrates with lower conductivity allow for more evaporative cooling, and therefore produce longer droplet lifetimes. The contact angle also determines the magnitude of cooling, with higher contact angles allowing for more cooling further from the temperature-anchoring substrate than lower contact angles.

Chapter 4

Evaporation of a Thin Droplet on a Thin Substrate when the Influence of the Thermal Properties of the System is Strong

4.1 Introduction

In this chapter we obtain closed-form solutions to the thermally-coupled diffusion-limited evaporation model described in chapter 2. In particular, we follow the approach (but not the model) of Dunn *et al.* [52] and examine the limit of a thin droplet ($\hat{\theta}_0 \ll 1$) evaporating on a thin substrate ($h^{\mathrm{s}} \ll 1$), with an expression for $\hat{c}_{\mathrm{sat}}$ that is linear in $\hat{T}$. The evaporation of a thin sessile droplet is analysed when the influence of the thermal properties of the system is strong. Specifically, we obtain asymptotic solutions for the evolution, and hence explicit expressions for the lifetimes, of a droplet when the

substrate has a high thermal resistance relative to the droplet and when the saturation concentration of the vapour depends strongly on temperature. The work presented in this chapter has been published in the Journal of Fluid Mechanics (Schofield *et al.* [117]).

4.2 Problem formulation

Whereas Dunn *et al.* [52] investigated the thin-film limit of the Dunn model described in section 2.3.2, here we investigate the corresponding thin-film limit of the thermally-coupled model, *i.e.* the thin-film model described in section 2.5. Moreover, Dunn *et al.* [52] only investigated the initial evaporation rate of the droplet, whereas here we investigate the full evolution of the droplets in the CR, CA, SS and SJ modes of evaporation.

In order to make analytical progress we follow the approach of Dunn *et al.* [50, 52] and assume that both the droplet and the substrate are thin (*i.e.* that $\hat{\theta}_0 \ll 1$ and $h^{\mathrm{s}} \ll 1$), but make no assumption about their relative thicknesses (*i.e.* we make no *a priori* assumption about the size of $h^{\mathrm{s}}/\hat{\theta}_0$). Hence at leading order in the appropriate thin-film limit, the free surface of the droplet is given by equation (2.81) and the volume of the droplet is given by equation (2.82).

In practice, the atmosphere is typically a relatively poor thermal conductor when compared with the droplet and the substrate [83, 112], and provided that

$$\frac{\hat{k}^{\mathrm{a}}}{\hat{k}}\theta_0 = \alpha\hat{\theta} \ll 1 \quad \text{and} \quad \frac{\hat{k}^{\mathrm{a}}}{\hat{k}^{\mathrm{s}}}\frac{\hat{h}^{\mathrm{s}}}{\hat{R}_0} = \beta h^{\mathrm{s}} \ll 1 \tag{4.1}$$

the energy balance conditions (2.90)–(2.92) reduce to

$$\left.\frac{\partial T^{\mathrm{s}}}{\partial z^{\mathrm{s}}}\right|_{z^{\mathrm{s}}=0} = 0 \qquad \text{for } r > R, \tag{4.2}$$

$$S\left.\frac{\partial T}{\partial \bar{z}}\right|_{\bar{z}=0} = \left.\frac{\partial T^{\mathrm{s}}}{\partial z^{\mathrm{s}}}\right|_{z^{\mathrm{s}}=0} \qquad \text{for } 0 < r < R, \tag{4.3}$$

$$J = -\frac{\lambda}{\hat{\theta}_0}\left.\frac{\partial T}{\partial \bar{z}}\right|_{\bar{z}=\bar{h}} = -\left.\frac{\partial c}{\partial z^{\mathrm{a}}}\right|_{z^{\mathrm{a}}=0}, \tag{4.4}$$

respectively, where λ and S are defined by (2.50) and (2.67), respectively. Note that, since both the droplet and the substrate are thin, these conditions hold when $\hat{k}$ and $\hat{k}^{\mathrm{s}}$ are comparable with $\hat{k}^{\mathrm{a}}$.

To simplify presentation, as well as investigate the influence of the variation of the saturation concentration of the vapour with temperature on the droplet evolution, we introduce the non-dimensional groups

$$\Delta C = \frac{\hat{\theta}_0 \hat{\mathcal{L}} \hat{D} \hat{c}'_{\mathrm{sat}}(\hat{T}_\infty)}{\hat{k}}, \quad E = \frac{\hat{\theta}_0}{\lambda} = \frac{\hat{\theta}_0 \hat{\mathcal{L}} \hat{D}(c_{\mathrm{sat}}(\hat{T}_\infty) - \hat{c}_\infty)}{\hat{k}\hat{T}_\infty} \tag{4.5}$$

where ΔC measures the variation of the saturation concentration of the vapour with temperature and E measures the evaporative cooling.

When (4.1) holds, and using (4.5), it is straightforward to show that equations (2.88) and (2.89) are satisfied by

$$T = 1 - EJ(\bar{z} + S) \quad \text{for} \quad 0 < \bar{z} < \bar{h}, \quad r < R, \tag{4.6}$$

$$T^{\mathrm{s}} = 1 - EJS(z^{\mathrm{s}} + 1) \quad \text{for} \quad -1 < z^{\mathrm{s}} < 0, \quad r < R, \tag{4.7}$$

$$T^{\mathrm{s}} = 1 \quad \text{for} \quad -1 < z^{\mathrm{s}} < 0, \quad r > R. \tag{4.8}$$

Following Dunn *et al.* [52], and using an expression for c_{sat} that is linear in T (*i.e.* $n = 1$ in equation (2.84)) the coupled problem for c as described in section 2.5.2 satisfies

$$\nabla^2 c = 0 \quad \text{in} \quad z^{\mathrm{a}} > 0 \tag{4.9}$$

subject to

$$c = 1 - \Delta C(h+S)J \quad \text{on} \quad z^{\mathrm{a}} = 0 \quad \text{for} \quad r < R, \tag{4.10}$$

$$\frac{\partial c}{\partial z^{\mathrm{a}}} = 0 \quad \text{on} \quad z^{\mathrm{a}} = 0 \quad \text{for} \quad r > R, \tag{4.11}$$

and

$$c \to 0 \quad \text{as} \quad (r^2 + z^{\mathrm{a}2})^{1/2} \to \infty, \tag{4.12}$$

and the decoupled problem for T^{a} satisfies

$$\nabla^2 T^{\mathrm{a}} = 0 \quad \text{in} \quad z^{\mathrm{a}} > 0 \tag{4.13}$$

subject to

$$T^{\mathrm{a}} = 1 - EJ(\bar{h}+S) \quad \text{on} \quad z^{\mathrm{a}} = 0 \quad \text{for} \quad r < R, \tag{4.14}$$

$$T^{\mathrm{a}} = 1 \quad \text{on} \quad z^{\mathrm{a}} = 0 \quad \text{for} \quad r > R, \tag{4.15}$$

and

$$T^{\mathrm{a}} \to 1 \quad \text{as} \quad (r^2 + z^{\mathrm{a}2})^{1/2} \to \infty. \tag{4.16}$$

The total evaporation rate is then given by

$$-\frac{\mathrm{d}\bar{V}}{\mathrm{d}\bar{t}} = -\frac{\pi}{4}\frac{\mathrm{d}}{\mathrm{d}t}(\theta R^3) = 2\pi \int_0^R J(r,t)\, r \mathrm{d}r, \tag{4.17}$$

where

$$J(r,t) = -\left.\frac{\partial c}{\partial z}\right|_{z=0}. \tag{4.18}$$

Whereas equations (4.9)–(4.12) show that the solution for c, and hence the evolution of the droplet given by (4.17) and (4.18), depends on ΔC and S but not E, equations (4.6)–(4.8) and (4.13)–(4.16) show that the evaporative cooling of the atmosphere, the droplet and the substrate also depends on E.

Note that although, as we have already mentioned, the thermally-coupled model differs from the Dunn model proposed by Dunn *et al.* [51], in the present limit of a thin droplet on a thin substrate the problem for T, T^{s} and c given by equations (4.6)–(4.12), but

not, of course, that for T^{a} given by equations (4.13)–(4.16), coincides exactly with the problem analysed by Dunn *et al.* [50, 52]. However, these latter authors considered only the initial evolution of a pinned droplet (*i.e.* evolution of a droplet evaporating in the CR mode for $t = O(1)$) and did not either analyse the entire evolution of the droplet or consider other modes of evaporation, both of which we do in this chapter.

In the special case $\Delta C = 0$ in which c_{sat} is independent of T the concentration of vapour at the free surface of the droplet is constant and we recover the thermally-decoupled model in which the solution for c, and hence the evolution of the droplet, is also independent of S, *i.e.* is entirely independent of the thermal properties of the system. Explicit expressions for the lifetimes of thin droplets in this special case (albeit using a different non-dimensionalisation of time) were obtained by [143] for the CR, CA and SS modes, and by [142] for the SJ mode. The key observation is that when $\Delta C = 0$ the lifetimes of thin droplets are, as anticipated, of the order of the basic timescale (2.1). This timescale is also applicable when thermal effects are weak, but not, as we shall show in the present chapter, when they are strong.

4.3 When the substrate has a high thermal resistance

Consider the evolution of an evaporating droplet using the model described in section 4.2 when the substrate has a high thermal resistance relative to the droplet (*i.e.* when the substrate is highly insulating and/or thick relative to the droplet), corresponding to the asymptotic limit $S \to \infty$ with $\Delta C \neq 0$.

Inspection of (4.9)–(4.17) suggests that in the limit $S \to \infty$ the complete evolution of a droplet will occur over the long timescale $\bar{t} = O(S) \gg 1$. In order to obtain a uniformly valid leading-order asymptotic solution able to capture the complete evolution of the droplet we therefore rescale c and J with $1/S$ and $\bar{t}$ with S by writing $c = \tilde{c}/S$, $J = \tilde{J}/S$ and $\bar{t} = S\tilde{t}$, and seek an asymptotic expansion for $\tilde{c}$ in the form

$$\tilde{c}(r, z, \tilde{t}) = \tilde{c}_0(r, z, \tilde{t}) + O(1/S), \tag{4.19}$$

with corresponding asymptotic expansions for the other dependent variables. Note that, in contrast to the other chapters of this thesis, throughout this chapter θ_0, R_0 and $\bar{V}_0$ denote the zeroth term in the asymptotic expansions of θ, R and $\bar{V}$, and not the initial values $\theta(0)$, $R(0)$ and $\bar{V}(0)$.

At leading order in the limit $S \to \infty$ we obtain $\tilde{J}_0 = 1/\Delta C$ (*i.e.* at leading order the mass flux from the free surface of the droplet is uniform and constant),

$$T_0 = 1 - E/\Delta C \tag{4.20}$$

(*i.e.* at leading order the droplet is uniformly cooled by a constant amount $E/\Delta C$) and

$$T_0^{\mathrm{s}} = 1 - E(z^{\mathrm{s}} + 1)/\Delta C, \tag{4.21}$$

and hence (4.17) yields the equation describing the leading-order evolution of the droplet, namely

$$\frac{\mathrm{d}}{\mathrm{d}\tilde{t}}(\theta_0 R_0^3) = -\frac{4R_0^2}{\Delta C}. \tag{4.22}$$

The explicit expression for the leading-order concentration of vapour,

$$\tilde{c}_0(r,z) = \int_0^\infty \frac{\mathcal{J}_0(\xi r)\mathcal{J}_1(\xi)\exp(-\xi z)}{\xi}\mathrm{d}\xi, \tag{4.23}$$

where $\mathcal{J}_n(\cdot)$ denotes the Bessel function of the first kind of order n, can be obtained (see, for example, [89]), but this is not required in order to determine the leading-order evolution of the droplet.

4.3.1 Evolution of a droplet evaporating in the Constant Radius mode

For a droplet evaporating in the CR mode with $R_0 \equiv 1$, solving (4.22) yields

$$R_0 \equiv 1, \quad \theta_0 = 1 - \frac{4}{\Delta C}\tilde{t}, \quad \bar{V}_0 = \frac{\pi\theta_0}{4}, \tag{4.24}$$

and hence the lifetime of the droplet, denoted by $\tilde{t}_{\rm CR}$, is given by $\tilde{t}_{\rm CR} = \Delta C/4$.

4.3.2 Evolution of a droplet evaporating in the Constant Angle mode

For a droplet evaporating in the CA mode with $\theta_0 \equiv 1$, solving (4.22) yields

$$R_0 = 1 - \frac{4}{3\Delta C}\tilde{t}, \quad \theta_0 \equiv 1, \quad \bar{V}_0 = \frac{\pi R_0^3}{4}, \tag{4.25}$$

and hence the lifetime of the droplet, denoted by $\tilde{t}_{\rm CA}$, is given by $\tilde{t}_{\rm CA} = 3\Delta C/4 = 3\tilde{t}_{\rm CR}$.

Both $\tilde{t}_{\rm CR}$ and $\tilde{t}_{\rm CA}$ are directly proportional to ΔC (*i.e.* stronger variation of $c_{\rm sat}$ with T leads to slower evaporation and hence to longer lifetimes), and their ratio is exactly 3. This latter result contrasts with that in the special case $\Delta C = 0$ discussed by [143] for which the corresponding ratio is exactly 3/2.

4.3.3 Evolution of a droplet evaporating in the Stick-Slide mode

As described in section 1.4, the stick-slide (SS) mode of evaporation consists of a CR phase which lasts until the contact angle reaches a critical receding contact angle $\theta^\star$ ($0 \leq \theta^\star \leq 1$) followed by a CA phase. For a droplet evaporating in this mode, solving (4.22) yields (4.24) for $0 < \tilde{t} < \tilde{t}^\star$ and

$$R_0 = \frac{(1+2\theta^\star)\Delta C - 4\tilde{t}}{3\theta^\star \Delta C}, \quad \theta_0 \equiv \theta^\star, \quad \bar{V}_0 = \frac{\pi\theta_0 R_0^3}{4} \tag{4.26}$$

for $\tilde{t}^\star < \tilde{t} < \tilde{t}_{\rm SS}$, where

$$\tilde{t}^\star = \frac{\Delta C}{4}(1-\theta^\star) \quad \text{and} \quad \tilde{t}_{\rm SS} = \frac{\Delta C}{4}(1+2\theta^\star) \tag{4.27}$$

are the depinning time (*i.e.* the time at which the contact angle θ_0 reaches the critical receding angle $\theta^\star$) and the lifetime of the droplet, respectively. Both $\tilde{t}^\star$ and $\tilde{t}_{\rm SS}$ are directly proportional to ΔC, $\tilde{t}^\star$ is a linearly decreasing function of $\theta^\star$ satisfying $\tilde{t}^\star = \tilde{t}_{\rm CR}$

at $\theta^\star = 0$ and $\tilde{t}^\star = 0$ at $\theta^\star = 1$, and $\tilde{t}_{\rm SS}$ is a linearly increasing function of $\theta^\star$ satisfying $\tilde{t}_{\rm SS} = \tilde{t}_{\rm CR}$ at $\theta^\star = 0$ and $\tilde{t}_{\rm SS} = \tilde{t}_{\rm CA}$ at $\theta^\star = 1$.

Figure 4.1 shows (a) R_0, (b) θ_0 and (c) $\bar{V}_0$ as functions of $\tilde{t}$ for various values of $\theta^\star$, including $\theta^\star = 0$ (*i.e.* the CR mode given by (4.24)) and $\theta^\star = 1$ (*i.e.* the CA mode given by (4.25)), and (d) $\bar{V}_0$ as a function of $\tilde{t}$ for various values of ΔC. Figure 4.1 illustrates that R_0 and θ_0 are either constant or linearly decreasing functions of $\tilde{t}$, $\bar{V}_0$ is first (for $0 < \tilde{t} < \tilde{t}^\star$) a linearly and then (for $\tilde{t}^\star < \tilde{t} < \tilde{t}_{\rm SS}$) a cubically decreasing function of $\tilde{t}$, and as $\theta^\star$ increases the droplet depins earlier but has a longer lifetime. Somewhat more unexpectedly, figure 4.1(a) also illustrates that, except in the special case $\theta^\star = 0$, $R_0 = 2/3$ at $\tilde{t} = \tilde{t}_{\rm CR}$ irrespective of the value of the critical receding angle $\theta^\star$ (*i.e.* whatever the non-zero value of $\theta^\star$, the contact radius always reduces to 2/3 of its initial value at $\tilde{t} = \tilde{t}_{\rm CR}$).

4.3.4 Evolution of a droplet evaporating in the Stick-Jump mode

As also described in section 1.4, the stick-jump (SJ) mode of evaporation consists of an infinite series of stick (*i.e.* CR) phases separated by an infinite series of jump phases in which the contact angle jumps instantaneously from a minimum value $\theta_{\rm min}$ to a maximum value $\theta_{\rm max}$ ($0 \leq \theta_{\rm min} \leq \theta_{\rm max} \leq 1$) with a corresponding instantaneous jump in the contact radius. For a droplet evaporating in this mode, if we denote by R_n ($n = 1, 2, 3, \ldots$) the constant value of R_0 during the nth stick (*i.e.* CR) phase lasting from $t = t_{n-1}$ to $t = t_n$, then, by conservation of mass during the nth jump phase occurring at $t = t_n$ ($n = 1, 2, 3, \ldots$), we have $\theta_{\rm min} R_n^3 = \theta_{\rm max} R_{n+1}^3$, and so

$$R_{n+1} = \left(\frac{\theta_{\rm min}}{\theta_{\rm max}}\right)^{1/3} R_n = \left(\frac{\theta_{\rm min}}{\theta_{\rm max}}\right)^{n/3} R_1. \tag{4.28}$$

During the 1st stick phase with $R_0 = R_1 \equiv 1$ from $t = t_0 = 0$ to $t = t_1 = \Delta C(1 - \theta_{\rm min})/4$, θ_0 and $\bar{V}_0$ are given by (4.24), and thereafter during the nth stick phase

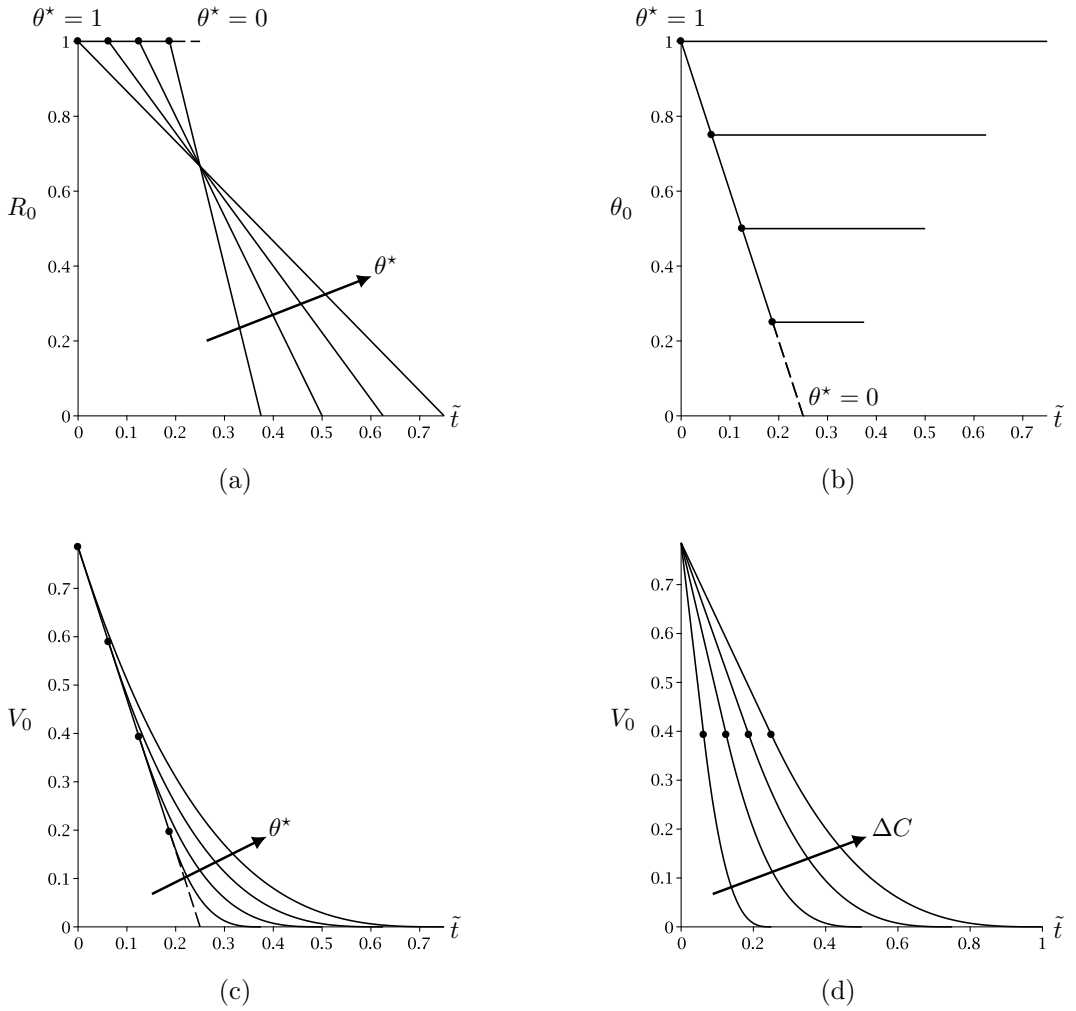

Figure 4.1: Evolution of a droplet on a substrate with a high thermal resistance (*i.e.* in the limit $S \to \infty$ with $\Delta C \neq 0$) evaporating in the SS mode. Plots of (a) R_0, (b) θ_0 and (c) $\bar{V}_0$ as functions of $\tilde{t}$ for $\theta^\star = 0$ (*i.e.* the CR mode, shown dashed), 1/4, 1/2, 3/4 and 1 (*i.e.* the CA mode) with $\Delta C = 1$, and (d) $\bar{V}_0$ as a function of $\tilde{t}$ for $\Delta C = 1/2$, 1, 3/2 and 2 with $\theta^\star = 1/2$. The dots (•) denote the instants at which depinning occurs (*i.e.* $\tilde{t} = \tilde{t}^\star$), and in parts (a), (c) and (d) the arrows indicate the direction of increasing values of the appropriate parameter.

$(n = 2, 3, 4, \ldots)$ with $R_0 = R_n$ from $t = t_{n-1}$ to $t = t_n$,

$$R_0 = R_n, \quad \theta_0 = \theta_{\max} - \frac{4}{\Delta C R_n}(\tilde{t} - \tilde{t}_{n-1}), \quad \bar{V}_0 = \frac{\pi \theta_0 R_n^3}{4}, \tag{4.29}$$

where

$$\tilde{t}_n = \frac{\Delta C}{4}\left[1 - \theta_{\max} + (\theta_{\max} - \theta_{\min})\frac{1 - (\theta_{\min}/\theta_{\max})^{n/3}}{1 - (\theta_{\min}/\theta_{\max})^{1/3}}\right]. \tag{4.30}$$

Taking the limit $n \to \infty$ in (4.30) we obtain the lifetime of the droplet, namely

$$\tilde{t}_{\rm SJ} = \frac{\Delta C}{4}\left[1 - \theta_{\max} + (\theta_{\max} - \theta_{\min})\frac{\theta_{\max}^{1/3}}{\theta_{\max}^{1/3} - \theta_{\min}^{1/3}}\right]. \tag{4.31}$$

In particular, $\tilde{t}_{\rm SJ}$ is directly proportional to ΔC, and is an increasing function of both $\theta_{\max}$ and $\theta_{\min}$ $(< \theta_{\max})$ satisfying $\tilde{t}_{\rm SJ} = \tilde{t}_{\rm CR}$ when $\theta_{\max} = 0$ and when $\theta_{\min} = 0$, and $\tilde{t}_{\rm SJ} \to \tilde{t}_{\rm SS}$ when $\theta_{\max} \to \theta_{\min} = \theta^\star$.

Figure 4.2 shows (a) R_0, (b) θ_0 and (c) V_0 as functions of $\tilde{t}$ for various values of $\theta_{\min}$, (d) V_0 as a function of $\tilde{t}$ for various values of ΔC, (e) $\tilde{t}_{\rm SJ}$ as a function of $\theta_{\min}$ $(\leq \theta_{\max})$ for various values of $\theta_{\max}$, and (f) $\tilde{t}_{\rm SJ}$ as a function of $\theta_{\max}$ $(\geq \theta_{\min})$ for various values of $\theta_{\min}$. Figure 4.2 illustrates that R_0 is constant and θ_0 is a linearly decreasing function of $\tilde{t}$ during each stick phase, R_0 and θ_0 jump instantaneously down and up, respectively, during each jump phase, and as the droplet evaporates the stick phases get progressively shorter (approaching zero duration in the limit $n \to \infty$).

4.4 When the saturation concentration depends strongly on temperature

A similar analysis to that described in section 4.3 can be performed when the saturation concentration of the vapour depends strongly on temperature, corresponding to the asymptotic limit $\Delta C \to \infty$.

Inspection of (4.9)–(4.17) suggests that in the limit $\Delta C \to \infty$ the complete evolution of a droplet will occur over the long timescale $\bar{t} = O(\Delta C) \gg 1$. Proceeding in the same

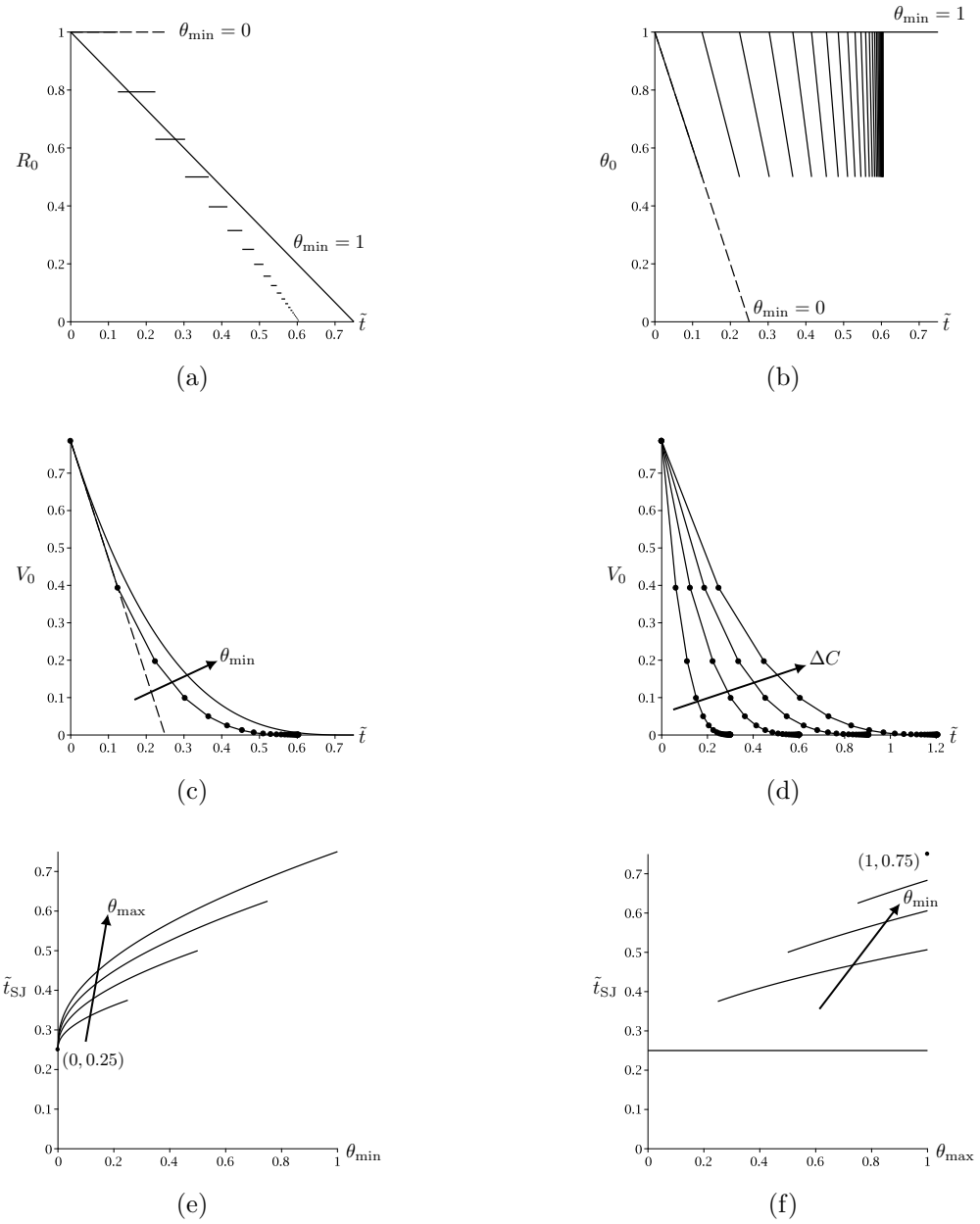

Figure 4.2: Evolution of a droplet on a substrate with a high thermal resistance (*i.e.* in the limit $S \to \infty$ with $\Delta C \neq 0$) evaporating in the SJ mode. Plots of (a) R_0, (b) θ_0 and (c) $\bar{V}_0$ as functions of $\tilde{t}$ for $\theta_{\min} = 0$ (*i.e.* the CR mode, shown dashed), 1/2 and 1 (*i.e.* the CA mode) with $\theta_{\max} = 1$ and $\Delta C = 1$, (d) V_0 as a function of $\tilde{t}$ for $\Delta C = 1/2$, 1, 3/2 and 2 with $\theta_{\max} = 1$ and $\theta_{\min} = 1/2$, (e) $\tilde{t}_{\rm SJ}$ as a function of $\theta_{\min} (\leq \theta_{\max})$ for $\theta_{\max} = 0$ (*i.e.* the CR mode), 1/4, 1/2, 3/4 and 1, and (f) $\tilde{t}_{\rm SJ}$ as a function of $\theta_{\max} (\geq \theta_{\min})$ for $\theta_{\min} = 0$ (*i.e.* the CR mode), 1/4, 1/2, 3/4 and 1 (*i.e.* the CA mode), with $\Delta C = 1$. In parts (c) and (d) the dots ($\bullet$) denote the instants at which the jump phases occur (*i.e.* $\tilde{t} = \tilde{t}_n$ for $n = 1, 2, 3, \ldots$), and in parts (c)–(f) the arrows indicate the direction of increasing values of the appropriate parameter.

manner as in section 4.3 we therefore rescale c and J with $1/\Delta C$ and $\bar{t}$ with ΔC by writing $c = \check{c}/\Delta C$, $J = \check{J}/\Delta C$ and $t = \Delta C\check{t}$, and seek an asymptotic expansion for $\check{c}$ in the form

$$\check{c}(r, z^{\mathrm{a}}, \check{t}) = \check{c}_0(r, z^{\mathrm{a}}, \check{t}) + O(1/\Delta C), \tag{4.32}$$

with corresponding asymptotic expansions for the other dependent variables.

In the limit $\Delta C \to \infty$ we obtain

$$\check{J} = \frac{2R_0}{[\theta_0(R_0^2 - r^2) + 2SR_0]\Delta C} + O\left(\frac{1}{\Delta C^2}\right), \tag{4.33}$$

$$T = 1 - \frac{2ER_0(\bar{z} + S)}{[\theta_0(R_0^2 - r^2) + 2SR_0]\Delta C} + O\left(\frac{1}{\Delta C^2}\right), \tag{4.34}$$

$$T^{\mathrm{s}} = 1 - \frac{2ER_0S(z^{\mathrm{s}} + 1)}{[\theta_0(R_0^2 - r^2) + 2SR_0]\Delta C} + O\left(\frac{1}{\Delta C^2}\right), \tag{4.35}$$

and hence (4.17) yields the equation describing the leading-order evolution of the droplet, namely

$$\frac{\mathrm{d}}{\mathrm{d}\check{t}}(\theta_0 R_0^3) = -\frac{8R_0}{\theta_0} \log\left(\frac{2S + \theta_0 R_0}{2S}\right). \tag{4.36}$$

In contrast to the limit $S \to \infty$, in this limit we are unable to obtain an explicit expression for the leading-order concentration of vapour, $\check{c}_0$, but, as in the limit $S \to \infty$, this is not required in order to determine the leading-order evolution of the droplet.

4.4.1 Evolution of a droplet evaporating in the Constant Radius mode

A droplet evaporating in the CR mode satisfies

$$R_0 \equiv 1, \quad \check{t} = F(1, 1, S) - F(1, \theta_0, S), \quad \bar{V}_0 = \frac{\pi\theta_0}{4}, \tag{4.37}$$

and hence $\check{t}_{\rm CR} = F(1,1,S)$, where $F(R_0,\theta_0,S)$ is an increasing function of each of its three arguments defined by

$$F(R_0,\theta_0,S) = \frac{S^2}{2}\left[\mathrm{Ei}\left(2\log\left(\frac{2S+\theta_0 R_0}{2S}\right)\right) - \mathrm{Ei}\left(\log\left(\frac{2S+\theta_0 R_0}{2S}\right)\right) - \log 2\right], \tag{4.38}$$

in which $\mathrm{Ei}(\cdot)$ denotes the exponential integral

$$\mathrm{Ei}(\xi) = -\int_{-\xi}^{\infty} \frac{\mathrm{e}^{-\lambda}}{\lambda}\,\mathrm{d}\lambda. \tag{4.39}$$

Note that $F(R_0,\theta_0,S)$ takes the value zero when any one of its arguments is zero.

4.4.2 Evolution of a droplet evaporating in the Constant Angle mode

A droplet evaporating in the CA mode satisfies

$$\check{t} = 3\left[F(1,1,S) - F(R_0,1,S)\right], \quad \theta_0 \equiv 1, \quad \bar{V}_0 = \frac{\pi R_0^3}{4}, \tag{4.40}$$

and hence $\check{t}_{\rm CA} = 3F(1,1,S) = 3\check{t}_{\rm CR}$.

Both $\check{t}_{\rm CR}$ and $\check{t}_{\rm CA}$ are increasing functions of S satisfying $\check{t}_{\rm CR}, \check{t}_{\rm CA} = O(1/\log S) \to 0^+$ as $S \to 0^+$, and $\check{t}_{\rm CR} \sim S/4 \to \infty$ and $\check{t}_{\rm CA} \sim 3S/4 \to \infty$ as $S \to \infty$, and (as in the limit $S \to \infty$) their ratio is exactly 3.

The solutions in the limit $\Delta C \to \infty$ given by (4.37) and (4.40) are similar, but not identical, to the corresponding solutions in the limit $S \to \infty$ given by (4.24) and (4.25) with S replaced by ΔC. Unlike the corresponding solutions in the limit $S \to \infty$, θ_0 and R_0 are not simply linear functions of $\check{t}$ in the CR and CA modes, respectively, and $\check{t}_{\rm CR}$ and $\check{t}_{\rm CA}$ are not simply linear functions of S. However, except for small values of S, the nonlinear function $F(R_0,\theta_0,S)$ defined by (4.38) is very well approximated by its linear leading-order small R_0 and/or small θ_0 and/or large S behaviour, *i.e.* $F(R_0,\theta_0,S) \approx \theta_0 R_0 S/4$. Hence, except for small values of S, the solutions in the limit $\Delta C \to \infty$ are very well approximated by the corresponding solutions in the limit $S \to \infty$ with S replaced by ΔC. In particular, except for small values of S, $\hat{t}_{\rm CR} \approx S/4$

and $\check{t}_{\rm CA} \approx 3S/4$.

4.4.3 Evolution of a droplet evaporating in the Stick-Slide mode

A droplet evaporating in the SS mode satisfies (4.37) for $0 < \check{t} < \check{t}^\star$ and

$$\check{t} = 2F(1,\theta^\star,S) + F(1,1,S) - 3F(R_0,\theta^\star,S), \quad \theta_0 \equiv \theta^\star, \quad \bar{V}_0 = \frac{\pi\theta^\star R_0^3}{4} \tag{4.41}$$

for $\check{t}^\star < \check{t} < \check{t}_{\rm SS}$, where

$$\check{t}^\star = F(1,1,S) - F(1,\theta^\star,S) \quad \text{and} \quad \check{t}_{\rm SS} = 2F(1,\theta^\star,S) + F(1,1,S). \tag{4.42}$$

Both $\check{t}^\star$ and $\check{t}_{\rm SS}$ are increasing functions of S satisfying $\check{t}^\star, \check{t}_{\rm SS} = O(1/\log S) \to 0^+$ as $S \to 0^+$, and $\check{t}^\star \sim S(1-\theta^\star)/4 \to \infty$ and $\check{t}_{\rm SS} \sim S(1+2\theta^\star)/4 \to \infty$ as $S \to \infty$. Furthermore, $\check{t}^\star$ is a decreasing function of $\theta^\star$ satisfying $\check{t}^\star = \check{t}_{\rm CR}$ at $\theta^\star = 0$ and $\check{t}^\star = 0$ at $\theta^\star = 1$, whereas $\check{t}_{\rm SS}$ is an increasing function of $\theta^\star$ satisfying $\check{t}_{\rm SS} = \check{t}_{\rm CR}$ at $\theta^\star = 0$ and $\check{t}_{\rm SS} = \check{t}_{\rm CA}$ at $\theta^\star = 1$. As for a droplet evaporating in either the CR or the CA mode, except for small values of S, the solutions in the limit $\Delta C \to \infty$ are again very well approximated by the corresponding solutions in the limit $S \to \infty$ with S replaced by ΔC, and so require no further discussion here.

4.4.4 Evolution of a droplet evaporating in the Stick-Jump mode

A droplet evaporating in the SJ mode again satisfies (4.28). During the 1st stick phase with $R_0 = R_1 \equiv 1$ from $t = t_0 = 0$ to $t = t_1 = F(1,1,S) - F(1,\theta_{\rm min},S)$, θ_0 and $\bar{V}_0$ are given by (4.37), and thereafter during the nth stick phase ($n = 2,3,4,\ldots$) with $R_0 = R_n$ from $t = t_{n-1}$ to $t = t_n$,

$$R_0 = R_n, \quad \check{t} - \check{t}_{n-1} = F(R_n,\theta_{\rm max},S) - F(R_n,\theta_0,S), \quad \bar{V}_0 = \frac{\pi\theta_0 R_n^3}{4}, \tag{4.43}$$

where

$$\check{t}_n = F(1,1,S) - F(1,\theta_{\min},S) + \sum_{m=2}^{n} F(R_m,\theta_{\max},S) - F(R_m,\theta_{\min},S). \tag{4.44}$$

Taking the limit $n \to \infty$ in (4.44) we obtain the lifetime of the droplet, namely

$$\check{t}_{\rm SJ} = F(1,1,S) - F(1,\theta_{\min},S) + \sum_{m=2}^{\infty} F(R_m,\theta_{\max},S) - F(R_m,\theta_{\min},S). \tag{4.45}$$

In particular, $\check{t}_{\rm SJ}$ is an increasing function of S satisfying $\check{t}_{\rm SJ} \to 0^+$ as $S \to 0^+$, and $\check{t}_{\rm SJ} = O(S) \to \infty$ as $S \to \infty$. Furthermore, $\check{t}_{\rm SJ}$ is an increasing function of both $\theta_{\max}$ and $\theta_{\min}$ $(< \theta_{\max})$ satisfying $\check{t}_{\rm SJ} = \check{t}_{\rm CR}$ when $\theta_{\max} = 0$ and when $\theta_{\min} = 0$, and $\check{t}_{\rm SJ} \to \check{t}_{\rm SS}$ when $\theta_{\max} \to \theta_{\min} = \theta^\star$. As for a droplet evaporating in either the CR or the CA mode, except for small values of S, the solutions in the limit $\Delta C \to \infty$ are again very well approximated by the corresponding solutions in the limit $S \to \infty$ with S replaced by ΔC, and so again require no further discussion here.

4.5 Conclusions

In this chapter we have analysed the evaporation of a thin sessile droplet on a thin substrate in two situations in which the influence of the thermal properties of the system is strong. Specifically, we have obtained uniformly valid leading-order asymptotic solutions for the evolution of the droplet when the substrate has a high thermal resistance relative to the droplet (corresponding to the limit $S \to \infty$ with $\Delta C \neq 0$) and when the saturation concentration of the vapour depends strongly on temperature (corresponding to the limit $\Delta C \to \infty$). In both situations we have obtained explicit expressions for the lifetimes of the droplet for all four of the modes of evaporation studied in the present chapter (namely the CR, CA, SS and SJ modes).

The thermally-decoupled model, which is applicable when the influence of the thermal properties of the system on the evolution of the droplet is weak, predicts that the lifetimes of the droplet are of the order of the thin-film limit of the basic timescale

(2.1), namely

$$\frac{\hat{\rho}}{2\hat{D}(\hat{c}_{\rm sat}(\hat{T}_\infty)-\hat{c}_\infty)}\left(\frac{3\hat{\theta}_0\hat{R}_0^3}{8}\right)^{2/3}. \tag{4.46}$$

In contrast, the present work shows that when the influence of the thermal properties of the system on the evolution of the droplet is strong (specifically, in the limit $S \to \infty$ and to a very good approximation in the limit $\Delta C \to \infty$), the lifetimes of the droplet are much longer than the basic timescale by a factor of size $S\Delta C \gg 1$, *i.e.* are actually on the much longer timescale

$$\frac{\hat{\rho}\hat{\theta}_0\hat{R}_0\hat{\mathcal{L}}\hat{h}^{\rm s}\hat{c}'_{\rm sat}(\hat{T}_\infty)}{\hat{k}^{\rm s}(\hat{c}_{\rm sat}(\hat{T}_\infty)-\hat{c}_\infty)}. \tag{4.47}$$

The different dependence of the timescales given by (4.46) and (4.47) on the physical parameters reflects the different dominant physical mechanisms when thermal effects are weak and when they are strong. The basic timescale (4.46), which is independent of $\hat{\mathcal{L}}$, $\hat{k}$, $\hat{k}^{\rm s}$ and $\hat{h}^{\rm s}$ (*i.e.* independent of the thermal properties of the system and the thickness of the substrate), corresponds to the familiar situation described by the thermally-decoupled diffusion-limited model in which the evaporation from the droplet is limited by diffusion of vapour in the atmosphere with constant saturation concentration at the free surface of the droplet. In contrast, the timescale (4.47), which is independent of $\hat{k}$ and $\hat{D}$ (*i.e.* independent of the thermal conductivity of the droplet and the coefficient of diffusion of vapour in the atmosphere), corresponds to the situation in which the evaporation from the droplet is limited by thermal conduction through the droplet and the substrate.

To illustrate the difference between the two situations, consider a thin droplet of methanol with initial radius $\hat{R}_0 = 10^{-3}$ m and initial contact angle $\hat{\theta}_0 = 0.02$ in an atmosphere of air with $\hat{c}_\infty = 0.4\hat{c}_{\rm sat}(\hat{T}_\infty)$, for which, using the typical parameter values given by [51], $\hat{\rho} = 790$ kg m^{-3}, $\hat{\mathcal{L}} = 1.20 \times 10^6$ m^2 s^{-2}, $\hat{k} = 0.203$ kg m s^{-3} K^{-1}, $\hat{c}_{\rm sat}(\hat{T}_\infty) = 0.186$ kg m^{-3}, $\hat{c}'_{\rm sat}(\hat{T}_\infty) = 9.47 \times 10^{-3}$ kg m^{-3} K^{-1} at $\hat{T}_\infty = 295$ K, and $\hat{D} = 1.50 \times 10^{-5}$ m^2 s^{-1}. The thermally-decoupled model predicts that on a

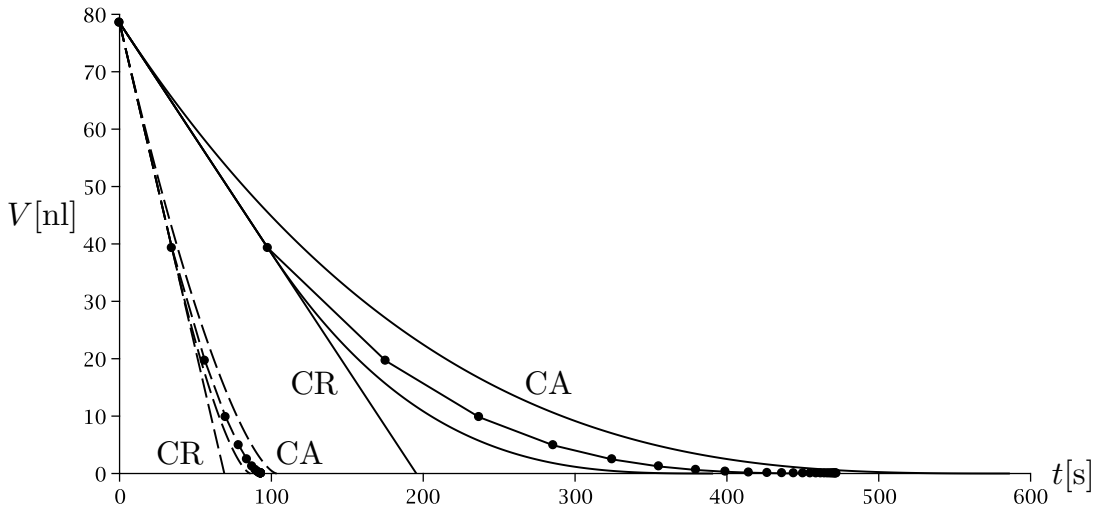

Figure 4.3: Evolution of the dimensional volume $\hat{V}$ (in nl) as a function of dimensional time $\hat{t}$ (in s) for a thin droplet of methanol on a substrate made of a good thermal conductor according to the thermally-decoupled model (dashed curves) and on a thin substrate made of an aerogel according to the present leading-order solution in the limit $S \to \infty$ with $\Delta C \neq 0$ (solid curves). In both cases the four curves correspond (from left to right) to evaporation in the CR, SS, SJ and CA modes. The dots (•) denote the instants at which depinning (SS mode) and the jump phases (SJ mode) occur.

substrate made of a good thermal conductor (such as, for example, a metal) the droplet evaporates completely in between 1.11 and 1.67 seconds (corresponding to the CR and CA modes, respectively). On the other hand, the present leading-order solution in the limit $S \to \infty$ with $\Delta C \neq 0$ predicts that on a thin substrate of thickness $\hat{h}^{\mathrm{s}} = 0.2$ mm made of a poor thermal conductor, specifically an aerogel with a typical thermal conductivity of $\hat{k}^{\mathrm{s}} = 0.015$ kg m s^{-3} K^{-1} (see, for example, [30]), corresponding to $\Delta C = 0.017$ and $S = 135$, the same droplet evaporates completely in between 3.22 and 9.65 seconds. Figure 4.3 shows the evolution of the dimensional volume $\hat{V}$ of the droplet as a function of dimensional time $\hat{t}$ for both substrates for all four modes of evaporation. In particular, figure 4.3 illustrates the main conclusion of the chapter, namely that when thermal effects are strong the lifetimes of evaporating droplets are significantly extended relative to those when thermal effects are weak.

Chapter 5

The Influence of the Shielding Effect on the Evaporation of Two-Dimensional Droplets

5.1 Introduction

In this chapter we analyse the evolution, and hence the lifetimes, of 2D droplets (as described in section 2.2.5) evaporating either singly, or as a pair. We consider the thermally-decoupled model for evaporation described in section 2.6 and use a conformal mapping technique to calculate the vapour concentrations in the surrounding atmosphere. Using the solution for the vapour concentration we obtain closed-form solutions for the evolution, and hence the lifetimes, of the droplets. The work presented in this chapter has recently been published in the Journal of Engineering Mathematics (Schofield *et al.* [118]).

In two dimensions there is a fundamental difficulty in solving the thermally-decoupled model concerning the specification of appropriate boundary conditions [134], which we will overcome, in the spirit of the work of Yarin *et al.* [166], by considering a suitably relaxed boundary condition.

In section 5.2 we consider the one-droplet problem. We present the governing equations (section 5.2.1), show that the most apparently natural problem does not have a solution (section 5.2.2), and then show that by considering a suitably relaxed boundary condition we can obtain a physically acceptable solution via a conformal-mapping technique (section 5.2.3). We validate this solution against numerical simulations (section 5.2.4), and use it to obtain closed-form solutions for the evolution and lifetimes of the droplet in various modes of evaporation (section 5.2.5). We then develop asymptotic expressions for these lifetimes in a large domain (section 5.2.5). In section 5.3 we consider the two-droplet problem. We obtain a solution to this problem (section 5.3.1), which we again validate against numerical simulations (section 5.3.2), before using it to obtain closed-form solutions for the evolution and lifetimes of the droplets (section 5.3.3). We develop asymptotic expressions for these lifetimes (section 5.3.3), and use these expressions to compare the lifetimes of a single droplet and a pair of droplets in dimensional terms (section 5.4).

5.2 One-droplet problem

5.2.1 Model

Consider a thin two-dimensional sessile droplet, as described in section 2.2.5, evaporating according to the 2D equivalent of the thermally-decoupled model described in section 2.6. The droplet has a semi-width $\hat{R}(\hat{t})$, contact angle $\hat{\theta}(\hat{t})$ and cross-sectional area $\hat{A}(\hat{t})$. Using Cartesian co-ordinates $(\hat{x}, \hat{y})$ with origin at the centre of the base of the droplet, the droplet evaporates into a surrounding atmosphere with constant coefficient of vapour diffusion $\hat{D}$, constant vapour saturation concentration $\hat{c} = \hat{c}_{\text{sat}}$, and constant ambient vapour concentration $\hat{c} = \hat{c}_{\infty}$. The vapour concentration in the atmosphere is denoted by $\hat{c}(\hat{x}, \hat{y}, \hat{t})$, and the diffusive mass flux from the surface of the droplet by $\hat{J}(\hat{x}, \hat{t})$.

Following the approach of Dunn *et al.* [50, 52], we non-dimensionalise and scale accord-

ing to

$$(\hat{x},\hat{y}) = \hat{R}_0(x,y), \quad \hat{R} = \hat{R}_0 R, \quad \hat{\theta} = \hat{\theta}_0\theta, \quad \hat{A} = \hat{R}_0^2\hat{\theta}_0 A,$$
$$\hat{c} = \hat{c}_\infty + (\hat{c}_{\rm sat} - \hat{c}_\infty)c, \quad \hat{J} = \frac{\hat{D}\,(\hat{c}_{\rm sat} - \hat{c}_\infty)}{\hat{R}_0}J, \quad \hat{t} = \frac{\hat{\rho}\hat{\theta}_0\hat{R}_0^2}{\hat{D}\,(\hat{c}_{\rm sat} - \hat{c}_\infty)}t, \tag{5.1}$$

where $\hat{R}_0 = \hat{R}(0)$ and $\hat{\theta}_0 = \hat{\theta}(0)$.

The free surface of the droplet is approximately parabolic and using the nondimensionalisation (5.1) its cross-sectional area is given by

$$A = \frac{2}{3}R^2\theta. \tag{5.2}$$

As in section 2.6, the vapour concentration is assumed to be quasi-steady, and so c satisfies Laplace's equation

$$\nabla^2 c = 0 \tag{5.3}$$

throughout the atmosphere.

Also as in section 2.6, the flux from the droplet is given by

$$J = -\frac{\partial c}{\partial y} \quad \text{for} \quad |x| \le R, \tag{5.4}$$

which may be evaluated at $y = 0$ due to the thinness of the droplet. Similarly, the saturation condition, $c = 1$, on the surface of the droplet may also be imposed on $y = 0$.

The saturation condition on the droplet and the no-flux condition on the substrate thus become

$$c(x,0) = 1 \quad \text{for} \quad |x| < R, \qquad \frac{\partial c}{\partial y}(x,0) = 0 \quad \text{for} \quad |x| > R, \tag{5.5}$$

respectively. To complete the problem we require a suitable boundary condition to be imposed in the "far field"; this turns out to be non-trivial to specify.

5.2.2 No solution in an infinite half-space

The simplest problem to specify is evaporation into an infinite half-space, so we aim to solve (5.3) subject to the far-field condition

$$c \to 0 \qquad \text{as} \qquad x^2 + y^2 \to \infty \quad \text{in} \quad y > 0, \tag{5.6}$$

as well as to a mixed boundary condition on $y = 0$ of the form

$$c(x,0) = f(x)\,(>0) \quad \text{for} \quad |x| < R, \qquad \frac{\partial c}{\partial y}(x,0) = 0 \quad \text{for} \quad |x| > R. \tag{5.7}$$

Applying a cosine transform to (5.3) and imposing the far-field condition (5.6) leads to a solution of the form

$$c = \int_0^\infty u^{-1} A(u) \mathrm{e}^{-uy} \cos(ux)\,\mathrm{d}u, \tag{5.8}$$

where the function $A(u)$ is to be determined. Imposing the boundary condition (5.7) requires that

$$\int_0^\infty u^{-1} A(u) \cos(xu)\,\mathrm{d}u = f(x) \quad \text{for} \quad |x| < R, \tag{5.9}$$

$$\int_0^\infty A(u) \cos(xu)\,\mathrm{d}u = 0 \quad \text{for} \quad |x| > R. \tag{5.10}$$

The work of Sneddon [134, §4.5] shows that requiring regularity of c at the contact line $x = R$ imposes the condition

$$\int_0^R \frac{f(x)}{\sqrt{R^2 - x^2}}\,\mathrm{d}x = 0, \tag{5.11}$$

so specifying that the function $f(x)$ is any positive constant is not an admissible boundary condition, and so, as could have been anticipated from the behaviour of the fundamental solution of Laplace's equation in two dimensions, the problem specified by (5.3), (5.5) and (5.6) has no solution. We note that (5.11) precludes not only solutions to the simplest problem in which the saturation concentration is constant on the droplet, but also solutions to more general problems in which it varies along the droplet surface due,

for example, to changes in temperature as in the thermally-coupled model described in section 2.4.

5.2.3 Solution in a finite domain via conformal mapping

Since the most apparently natural problem does not have a solution, we instead look for a closely related analogue that does. We therefore consider a slightly modified problem in which the far-field condition (5.6) is replaced by a similar Dirichlet condition at a distant, but finite, boundary. We therefore aim to solve

$$\nabla^2 c = 0 \quad \text{in} \quad y > 0, \quad x^2 + y^2 < \gamma^2, \tag{5.12}$$

subject to the standard boundary conditions on $y = 0$,

$$c(x,0) = 1 \quad \text{for} \quad |x| < R, \qquad \frac{\partial c}{\partial y}(x,0) = 0 \quad \text{for} \quad R < |x| < \gamma, \tag{5.13}$$

and the relaxed boundary condition

$$c = 0 \quad \text{for} \quad y > 0, \quad x^2 + y^2 = \gamma^2. \tag{5.14}$$

While it is difficult to find an analytical solution in a domain that is exactly semi-circular, we can obtain a solution in a semi-elliptical domain that approaches a semi-circular shape as it becomes large.

We proceed using conformal mapping. Let

$$z = x + \mathrm{i}y, \quad w = u + \mathrm{i}v. \tag{5.15}$$

Then the mapping

$$z = g(w) = -R \cos\left(\frac{\pi}{2}(w+1)\right) \tag{5.16}$$

maps the semi-infinite strip $(u, v) \in (-1, 1) \times (0, \infty)$ in the w-plane to the upper half of the z-plane. In particular, the rectangle $(-1, 1) \times (0, S)$ shown in figure 5.1(a) is

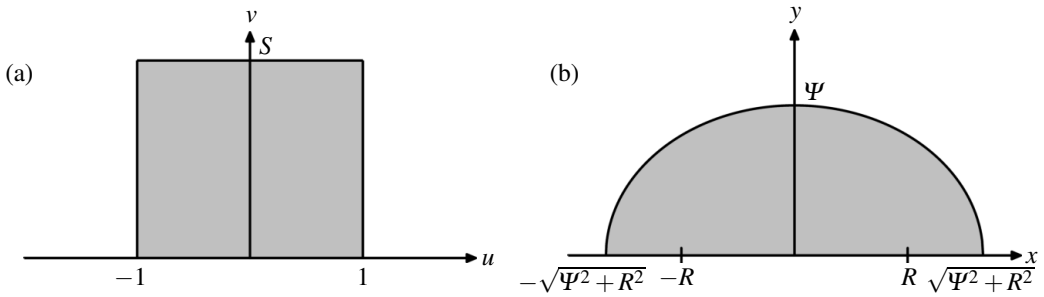

Figure 5.1: (a) The rectangular domain in the w-plane and (b) the semi-elliptical domain in the z-plane for the one-droplet problem.

mapped to the semi-ellipse with semi-major axis length $\sqrt{\Psi^2 + R^2}$ and semi-minor axis length Ψ shown in figure 5.1(b) and given by

$$z = \sqrt{\Psi^2 + R^2}\cos(s) + \mathrm{i}\Psi\sin(s) \quad \text{for} \quad 0 \leq s \leq \pi, \tag{5.17}$$

where

$$\Psi = R\sinh\left(\frac{\pi S}{2}\right). \tag{5.18}$$

An important point to note is that the shape of the semi-elliptical domain in the z-plane given by (5.17) depends on R as well as on Ψ. Thus, in general, for a droplet whose semi-width changes as it evolves, the shape of the domain also changes. However, in the regime of most interest, $\Psi \gg R$, in which the domain is large, equation (5.17) gives

$$z = \Psi \mathrm{e}^{\mathrm{i}s}\left[1 + O(\Psi^{-2})\right], \tag{5.19}$$

and so the domain is semi-circular with radius Ψ and independent of R up to $O(\Psi^{-2}) \ll 1$.

In the rectangular domain in the w-plane we seek a harmonic function $\Phi(u, v)$ satisfying

$$\Phi(u, 0) = 1, \quad \frac{\partial\Phi}{\partial u}(-1, v) = 0 = \frac{\partial\Phi}{\partial u}(1, v), \quad \Phi(u, S) = 0. \tag{5.20}$$

Solving the problem for Φ in the rectangular domain immediately gives the corresponding solution for c in the semi-elliptical domain.

By inspection, the solution in the rectangular domain is given by

$$\Phi(u,v) = 1 - \frac{v}{S} = 1 - \frac{\Im(w)}{S}, \tag{5.21}$$

so

$$c(x,y) = 1 - \frac{\Im\left(g^{-1}(z)\right)}{S} = 1 - \frac{1}{\operatorname{arcsinh}(\Psi/R)}\Im\left[\arccos\left(-\frac{z}{R}\right)\right], \tag{5.22}$$

and the flux is given by

$$J(x) = -\frac{\partial c}{\partial y}(x,0) = \frac{1}{\operatorname{arcsinh}(\Psi/R)}\frac{1}{\sqrt{R^2 - x^2}} \quad \text{for} \quad |x| < R. \tag{5.23}$$

In particular, the flux satisfies

$$J \sim \frac{1}{\sqrt{2R}\operatorname{arcsinh}(\Psi/R)}\frac{1}{\sqrt{R - x}} \quad \text{as} \quad x \to R^-, \tag{5.24}$$

and so it has the same (integrable) square-root singularity at the contact line $x = R$ as in the corresponding three-dimensional problem discussed in section 2.6.1.

5.2.4 Numerical validation

In order to validate the solution obtained in section 5.2.3 (i.e. in order to assess the accuracy of the solution and to quantify the effect of the non-circularity of the domain), we solved the problem in the semi-circular domain using COMSOL Multiphysics [1]. In figure 5.2 we compare these numerical solutions to the analytical solutions in the semi-elliptical domain given by (5.22) and (5.23).

Figures 5.2(a)–(c) show solutions for the vapour concentration along the x-axis, $c(x,0)$; (d)–(f) show solutions for the vapour concentration along the y-axis, $c(0,y)$; (g)–(i) show solutions for the flux, $J(x)$. The first column [(a), (d), (g)] shows results for $\Psi = 2$, the second column [(b), (e), (h)] shows results for $\Psi = 10$, and the third column [(c), (f), (i)] shows results for $\Psi = 100$. In all cases the solid lines denote the analytical solutions in the semi-elliptical domain, and the dashed lines denote the corresponding numerical solutions in the semi-circular domain. Figures 5.2(a)–(f) show

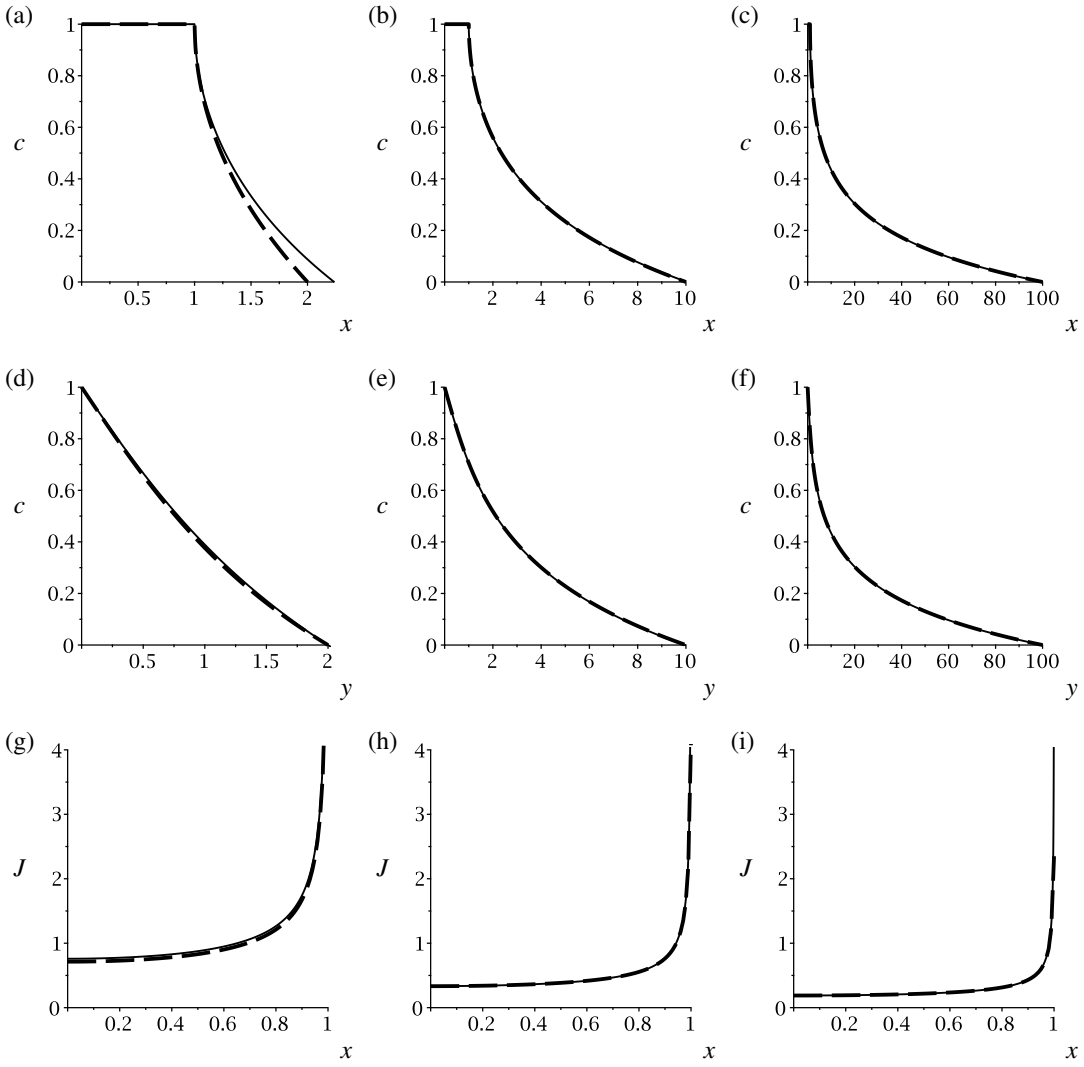

Figure 5.2: The vapour concentration and flux for the one-droplet problem for $R = 1$ and $\Psi = 2$ [(a), (d), (g)], $\Psi = 10$ [(b), (e), (h)], and $\Psi = 100$ [(c), (f), (i)]. (a)–(c) show solutions for the vapour concentration along the x-axis, $c(x, 0)$; (d)–(f) show solutions for the vapour concentration along the y-axis, $c(0, y)$; (g)–(i) show solutions for the flux, $J(x)$. Solid lines denote the analytical solutions in the semi-elliptical domain given by (5.22) and (5.23), and dashed lines denote the corresponding numerical solutions in the semi-circular domain.

that the vapour concentration c takes its saturation value $c = 1$ on the surface of the droplet and decreases monotonically to its ambient value $c = 0$ at the edge of the domain, and figures 5.2(g)–(i) show that the flux J increases monotonically with distance from a minimum value at the centre of the droplet and is singular at the contact line $x = R$. Figure 5.2 also shows that the analytical solutions accurately capture the behaviour of the numerical solutions provided that Ψ is sufficiently large, which is exactly as expected since it is for smaller domains that the semi-circular and semi-elliptical domains are most different.

5.2.5 Evolution and lifetime of the droplet

The rate of change of the cross-sectional area (5.2) is given by the flux (5.23) integrated over the surface of the droplet,

$$\frac{\mathrm{d}A}{\mathrm{d}t} = \frac{2}{3}\frac{\mathrm{d}}{\mathrm{d}t}\left[R^2(t)\theta(t)\right] = -\int_{-R}^{R} J(x)\,\mathrm{d}x = -\frac{\pi}{\operatorname{arcsinh}(\Psi/R)}. \tag{5.25}$$

In order to integrate (5.25) to determine the evolution and lifetime of the droplet, we require additional information about the behaviour of $R(t)$ and $\theta(t)$, i.e. we need to specify the mode in which the droplet is evaporating. Here we consider the two-dimensional analogues of three of these modes: the constant radius (CR) mode, the constant angle (CA) mode, and the stick–slide (SS) mode described in section 1.4. (Throughout, for consistency with the three-dimensional problem, we will refer to modes in which R is fixed as "constant-radius" modes, although strictly R is not the radius but the semi-width of the two-dimensional droplet.)

Constant radius (CR) mode

In the constant radius (CR) mode, $R(t) \equiv R_0 = 1$. Noting that $\theta(0) = \theta_0 = 1$, we may immediately integrate (5.25) to obtain

$$\theta(t) = 1 - \frac{3\pi}{2\operatorname{arcsinh}\Psi}t, \quad A(t) = \frac{2}{3}\left[1 - \frac{3\pi}{2\operatorname{arcsinh}\Psi}t\right]. \tag{5.26}$$

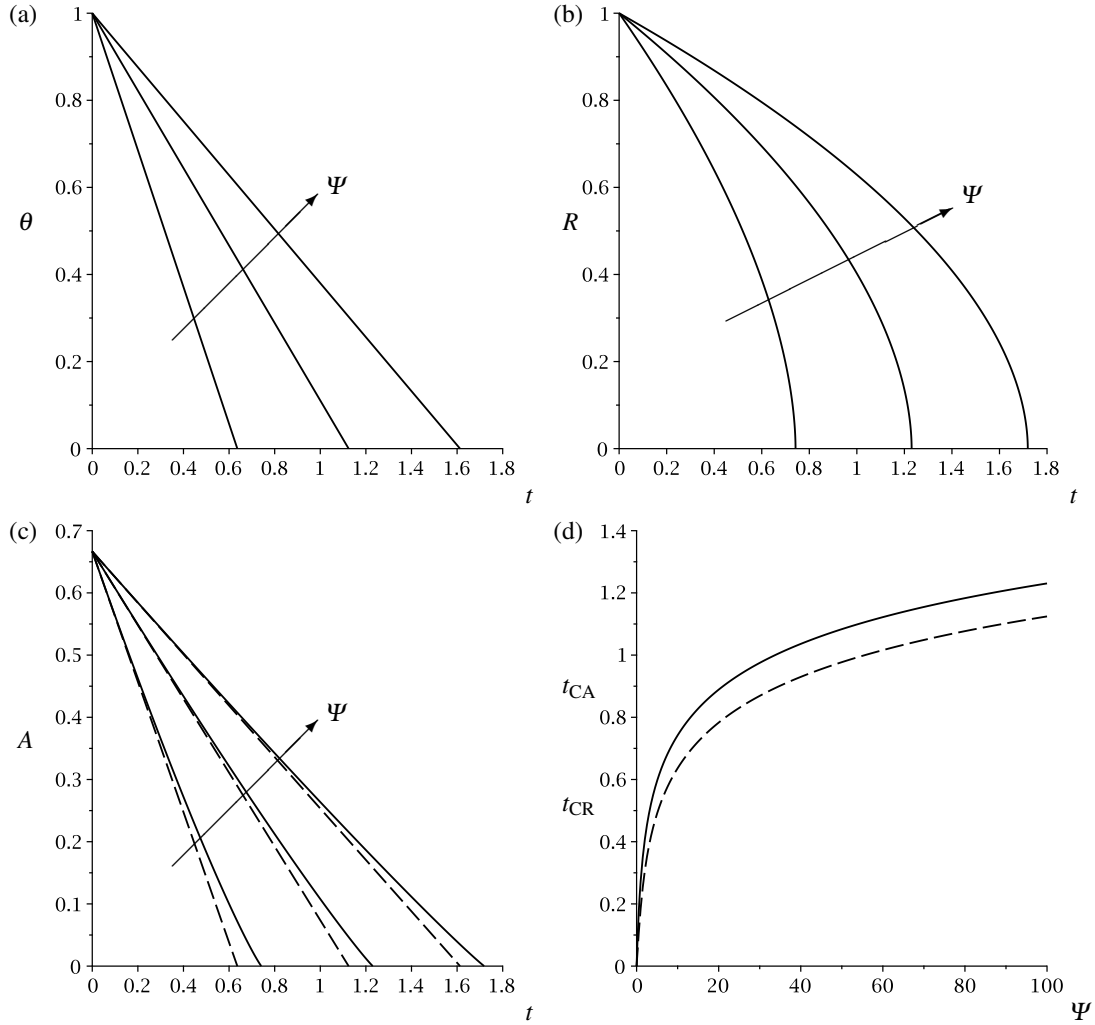

Figure 5.3: Evolution and lifetime of a single droplet evaporating in the CR and CA modes: (a) contact angle $\theta(t)$ in the CR mode given by (5.26), (b) semi-width $R(t)$ in the CA mode given by (5.28), and (c) areas $A(t)$ given by (5.26) and (5.28), plotted as functions of t for $\Psi = 10$, 100 and 1000 with the arrows indicating the direction of increasing Ψ; (d) lifetimes t_{CR} and t_{CA} given by (5.27) and (5.29) plotted as functions of Ψ. In (c) and (d) solid lines denote the CA mode and dashed lines denote the CR mode.

Hence the lifetime of a single droplet evaporating in the CR mode is

$$t_{\mathrm{CR}} = \frac{2}{3\pi} \operatorname{arcsinh} \Psi. \tag{5.27}$$

Figures 5.3(a,c,d) show the evolution and lifetime of a single droplet evaporating in the CR mode. The contact angle θ and the area A both decrease linearly with time t [figures 5.3(a,c)]. As the size of the domain Ψ increases, the contact angle θ and the area A decrease more slowly, and so the lifetime t_{CR} increases monotonically with Ψ [figure 5.3(d)]. This is because in two dimensions the distance to the outer boundary sets the distance over which the concentration decays to zero, and thus controls the concentration gradient close to the droplet, as seen in (5.23). This strong role of the outer boundary is a fundamental difference from the corresponding three-dimensional problem, in which the distance to the outer boundary becomes irrelevant for a sufficiently large domain, and so a far-field boundary condition can be safely imposed "at infinity".

Constant angle (CA) mode

In the constant angle (CA) mode, $\theta(t) \equiv \theta_0 = 1$. Noting that $R(0) = R_0 = 1$, we may integrate (5.25) implicitly to obtain

$$t = \frac{2}{3\pi} \left[\operatorname{arcsinh} \Psi - R^2(t) \operatorname{arcsinh} \left(\frac{\Psi}{R(t)} \right) + \Psi \left(\sqrt{\Psi^2 + 1} - \sqrt{\Psi^2 + R^2(t)} \right) \right],$$

$$A(t) = \frac{2R^2(t)}{3}. \tag{5.28}$$

Hence the lifetime of a single droplet evaporating in the CA mode is

$$t_{\mathrm{CA}} = \frac{2}{3\pi} \left[\operatorname{arcsinh} \Psi + \Psi \left(\sqrt{\Psi^2 + 1} - \Psi \right) \right], \tag{5.29}$$

which can be re-written as

$$t_{\mathrm{CA}} = t_{\mathrm{CR}} + \frac{2\Psi}{3\pi}\left(\sqrt{\Psi^2+1} - \Psi\right). \tag{5.30}$$

Figures 5.3(b,c,d) show the evolution and lifetime of a single droplet evaporating in the CA mode. In contrast to the CR mode, the semi-width R and the area A now both decrease nonlinearly with time t [figures 5.3(b,c)]. However, as in the CR mode, the lifetime t_{CA} increases monotonically with Ψ [figure 5.3(d)]. Figure 5.3(d) also illustrates, as (5.30) also shows, that due to its pinned contact lines, a droplet evaporating in the CR mode always has a larger surface area, and hence a larger total flux and thus a shorter lifetime, than the same droplet evaporating in the CA mode, i.e. $t_{\mathrm{CR}} \leq t_{\mathrm{CA}}$ for all Ψ.

Stick–slide (SS) mode

In the stick–slide (SS) mode, the contact line is initially pinned, while the contact angle decreases until it reaches its critical de-pinning (receding) value $\theta = \theta^\star$ ($0 \leq \theta^\star \leq 1$) at the de-pinning time $t = t^\star$. After de-pinning, the contact angle remains at its critical value, while the semi-width decreases until it reaches zero. Thus we have

$$\left.\begin{array}{lll} R(t) \equiv 1 & \text{for} & 0 < t < t^\star, \\ \theta(t) \equiv \theta^\star & \text{for} & t^\star < t < t_{\mathrm{SS}}. \end{array}\right\} \tag{5.31}$$

In the pinned (i.e. the CR) phase, $0 < t < t^\star$, the droplet evolves according to (5.26), so that

$$t^\star = \frac{2(1-\theta^\star)\,\operatorname{arcsinh}\Psi}{3\pi}, \tag{5.32}$$

while in the de-pinned (i.e. the CA) phase, $t^\star < t < t_{\rm SS}$, the droplet evolves according to

$$t = t^\star + \frac{2\theta^\star}{3\pi}\left[\operatorname{arcsinh}\Psi - R^2(t)\operatorname{arcsinh}\left(\frac{\Psi}{R(t)}\right) + \Psi\left(\sqrt{\Psi^2+1} - \sqrt{\Psi^2+R^2(t)}\right)\right]. \tag{5.33}$$

Combining (5.32) and (5.33), the lifetime of a single droplet evaporating in the SS mode is

$$t_{\rm SS} = \frac{2}{3\pi}\left[\operatorname{arcsinh}\Psi + \theta^\star\Psi\left(\sqrt{\Psi^2+1} - \Psi\right)\right], \tag{5.34}$$

which can be re-written as

$$t_{\rm SS} = t_{\rm CR} + \frac{2\theta^\star\Psi}{3\pi}\left(\sqrt{\Psi^2+1} - \Psi\right). \tag{5.35}$$

Figure 5.4 shows the evolution and lifetime of a single droplet evaporating in the SS mode. The de-pinning time $t^\star$ decreases linearly with $\theta^\star$, while the lifetime $t_{\rm SS}$ increases linearly with $\theta^\star$ [figure 5.4(d)]. Comparing (5.27), (5.30) and (5.35) shows that, as might have been anticipated, the lifetime of a droplet evaporating in the SS mode always lies between those of the same droplet in the CR and CA modes, i.e. $t_{\rm CR} \leq t_{\rm SS} \leq t_{\rm CA}$ for all Ψ and $\theta^\star$. In the limit $\theta^\star \to 1^-$ the SS mode approaches the CA mode and thus $t_{\rm SS} \to {t_{\rm CA}}^-$, while in the limit $\theta^\star \to 0^+$ the SS mode approaches the CR mode and thus $t_{\rm SS} \to {t_{\rm CR}}^+$.

We note that in figure 5.4(a) all of the curves for which $\theta^\star \neq 0$ intersect at $t = t_{\rm CR}$, and from (5.27), (5.32) and (5.33), the semi-width of the droplet at this time, $R(t_{\rm CR})$, satisfies

$$R^2(t_{\rm CR})\operatorname{arcsinh}\left(\frac{\Psi}{R(t_{\rm CR})}\right) = \Psi\left(\sqrt{\Psi^2+1} - \sqrt{\Psi^2+R^2(t_{\rm CR})}\right). \tag{5.36}$$

Note that $R(t_{\rm CR})$ is a monotonically decreasing function of Ψ which takes its maximum value $R(t_{\rm CR}) = 1/2$ in the limit $\Psi \to 0^+$ and satisfies $R(t_{\rm CR}) \to 0^+$ as $\Psi \to \infty$.

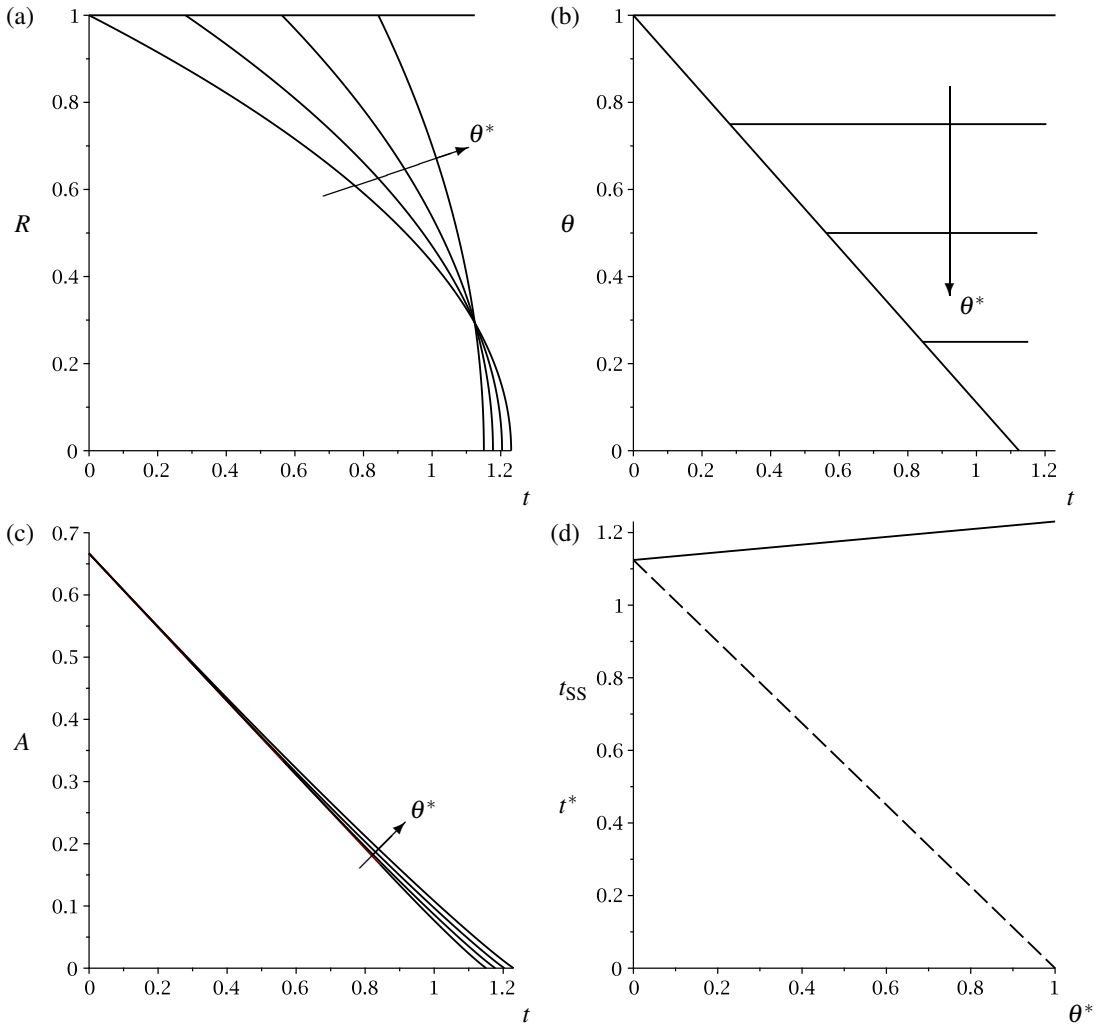

Figure 5.4: Evolution and lifetime of a single droplet evaporating in the SS mode: (a) semi-width $R(t)$, (b) contact angle $\theta(t)$, and (c) area $A(t)$ given by (5.31)–(5.33), plotted as functions of t for $\theta^\star = 0$, $\theta^\star = 1/4$, $\theta^\star = 1/2$, $\theta^\star = 3/4$ and $\theta^\star = 1$ with the arrows indicating the direction of increasing $\theta^\star$; (d) de-pinning time $t^\star$ given by (5.32) (dashed line) and lifetime $t_{\rm SS}$ given by (5.34) (solid line) plotted as functions of Ψ. In all cases $\Psi = 100$.

Asymptotic behaviour of the lifetimes in a large domain, $\Psi \gg R$

Consider the regime of most interest, $\Psi \gg R$, in which the domain is large and approximately semi-circular, and the condition at the outer boundary corresponds most closely to a far-field condition. From (5.27), (5.29) and (5.34) we obtain

$$t_{\mathrm{CR}} = \frac{2}{3\pi}\ln(2\Psi) + O\left(\frac{1}{\Psi^2}\right), \tag{5.37}$$

$$t_{\mathrm{CA}} = \frac{2}{3\pi}\ln(2\Psi) + \frac{1}{3\pi} + O\left(\frac{1}{\Psi^2}\right), \tag{5.38}$$

$$t_{\mathrm{SS}} = \frac{2}{3\pi}\ln(2\Psi) + \frac{\theta^\star}{3\pi} + O\left(\frac{1}{\Psi^2}\right), \tag{5.39}$$

respectively. Equations (5.37)–(5.39) show that the lifetimes of the droplets all depend logarithmically on the size of the domain, and differ by an amount of $O(1)$ which depends on the mode of evaporation. The corrections at $O(\Psi^{-2})$ are of the same order as the deviation of the domain from circularity.

5.3 Two-droplet problem

We now consider the analogous two-droplet problem in the ζ-plane, where $\zeta = \eta + \mathrm{i}\xi$. We assume that the droplets are identical, and use the initial semi-width of the droplets as the characteristic length scale in the non-dimensionalisation. The droplets are located so that they have inner contact lines at $\eta = \pm I$ and outer contact lines at $\eta = \pm\Omega$, where $\Omega > I$, as shown in Figure 5.5. The cross-sectional area of each droplet is then given by

$$A = \frac{(\Omega - I)^2\,\theta}{6}. \tag{5.40}$$

5.3.1 Solution in a finite domain via conformal mapping

Consider the conformal map

$$\zeta = \Gamma(z) = \sqrt{I^2 + z^2} \tag{5.41}$$

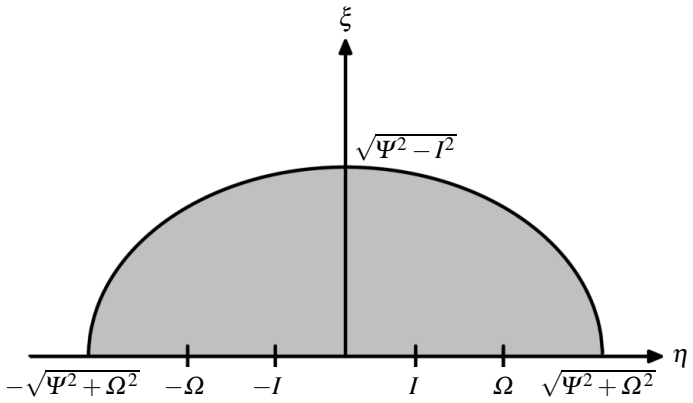

Figure 5.5: The quasi-semi-elliptical domain in the ζ-plane for the two-droplet problem.

from the z-plane to the ζ-plane. This maps the real interval $(0, R)$ in the z-plane to the real interval (I, Ω) where $\Omega = \sqrt{I^2 + R^2}$ in the ζ-plane, preserving the saturation condition on the droplet. It maps the real interval $(R, \sqrt{\Psi^2 + R^2})$ in the z-plane to the real interval $(\Omega, \sqrt{\Psi^2 + \Omega^2})$ in the ζ-plane, preserving the no-flux condition on the substrate. It maps the imaginary interval $(0, \mathrm{i}I)$ in the z-plane to the real interval $(0, I)$ in the ζ-plane: the symmetry condition on the imaginary axis in the z-plane now becomes a no-flux condition on the real interval $(0, I)$ in the ζ-plane. With a suitable choice of branch cut, the equivalent regions in the left half of the z-plane are mapped into corresponding regions in the left half of the ζ-plane. The outer boundary of the domain, given by the rectangle in the z-plane and the semi-ellipse (5.17) in the z-plane, is mapped to the quasi-semi-elliptical curve shown in figure 5.5 and given by

$$\zeta = \left[I^2 + \left(\sqrt{\Psi^2 + \Omega^2 - I^2}\, \cos(s) + \mathrm{i}\Psi \sin(s) \right)^2 \right]^{1/2} \quad \text{for} \quad 0 \leq s \leq \pi. \tag{5.42}$$

However, as in the one-droplet problem, in the regime of most interest, $\Psi \gg I$, in which the domain is large, equation (5.42) gives

$$\zeta = \Psi \mathrm{e}^{\mathrm{i}s} \left[1 + O(\Psi^{-2}) \right], \tag{5.43}$$

and so the domain is again semi-circular with radius Ψ and independent of I and Ω up to $O(\Psi^{-2}) \ll 1$.

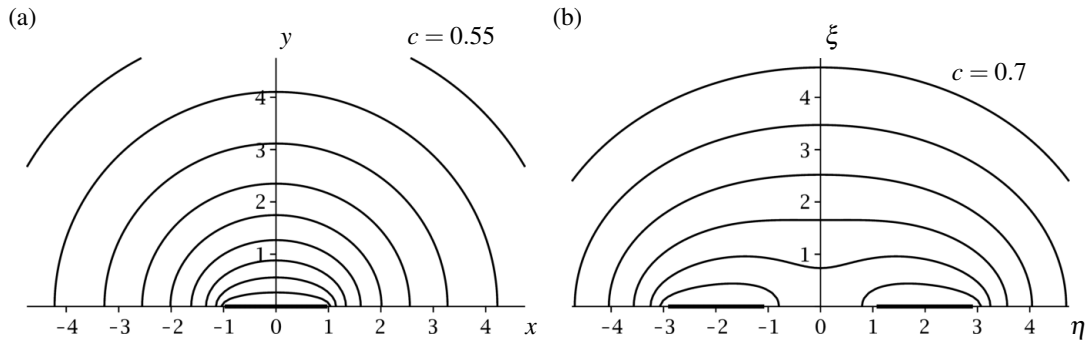

Figure 5.6: Contours of the vapour concentration (a) $c(x, y)$ for the one-droplet problem given by (5.22) when $R = 1$, and (b) $c(\eta, \xi)$ for the two-droplet problem given by (5.45) when $I = 1$ and $\Omega = 3$. In both cases $\Psi = 100$ and the contours are shown with increments of 0.05.

The solution in the quasi-semi-elliptical domain is given by

$$c(\eta, \xi) = c(\zeta) = c(w(z(\zeta))) \tag{5.44}$$

$$= 1 - \frac{1}{\operatorname{arcsinh}\left(\Psi/\sqrt{\Omega^2 - I^2}\right)} \Im\left[\arccos\left(-\sqrt{\frac{\zeta^2 - I^2}{\Omega^2 - I^2}}\right)\right]. \tag{5.45}$$

Figure 5.6 shows the contours of the vapour concentration $c(\eta, \xi)$ for the two-droplet problem given by (5.45) and the corresponding contours of $c(x, y)$ for the one-droplet problem given by (5.22). In both cases, far from the droplet(s) the contours approach the (semi-elliptical or quasi-semi-elliptical) shape of the outer boundary, and near to the droplet(s) the contours approach the flat shape(s) of the droplet(s). For the two-droplet problem the concentration in the region between the droplets is increased relative to that in the one-droplet problem, and near to the droplets the concentration falls away more gradually than it does in the one-droplet problem, and resulting in the shielding effect described in section 5.1.

The flux is given by

$$J(\eta) = -\frac{\partial c}{\partial \xi}(\eta, 0) = \frac{1}{\operatorname{arcsinh}\left(\Psi/\sqrt{\Omega^2 - I^2}\right)} \frac{\eta}{\sqrt{\Omega^2 - \eta^2}\sqrt{\eta^2 - I^2}}. \tag{5.46}$$

In particular, the flux satisfies

$$J \sim \frac{1}{\sqrt{2(\Omega^2 - I^2)}\,\operatorname{arcsinh}\left(\Psi/\sqrt{\Omega^2 - I^2}\right)} \times \begin{cases} \sqrt{\dfrac{I}{\eta - I}} & \text{as} \quad \eta \to I^+, \\ \sqrt{\dfrac{\Omega}{\Omega - \eta}} & \text{as} \quad \eta \to \Omega^-, \end{cases} \tag{5.47}$$

confirming that it again has square-root singularities at both contact lines.

5.3.2 Numerical validation

As we did in the one-droplet problem, in order to validate the solution obtained in Section 5.3.1, we solved the two-droplet problem in the semi-circular domain using COMSOL Multiphysics [1]. In figure 5.7 we compare these numerical solutions to the analytical solutions in the quasi-semi-elliptical domain given by (5.45) and (5.46).

Figures 5.7(a)–(c) show solutions for the vapour concentration along the η-axis, $c(\eta, 0)$; (d)–(f) show solutions for the vapour concentration along the ξ-axis, $c(0, \xi)$; (g)–(i) show solutions for the flux, $J(\eta)$. The first column [(a), (d), (g)] shows results for $\Psi = 4$, the second column [(b), (e), (h)] shows the corresponding results for $\Psi = 10$, and the final column [(c), (f), (i)] shows the corresponding results for $\Psi = 100$. In all cases the solid lines denote the analytical solutions in the quasi-semi-elliptical domain, and the dashed lines denote the corresponding numerical solutions in the semi-circular domain. As in the one-droplet problem, figure 5.7 shows that c takes its saturation value on the surface of the droplets and decreases monotonically to its ambient value at the edge of the domain, that J is singular at the contact lines $x = I$ and $x = \Omega$, and that the analytical solutions accurately capture the behaviour of the numerical solutions provided that Ψ is sufficiently large.

However, figures 5.7(a)–(f) also show that c decreases monotonically to an (unsaturated) minimum value between the droplets, and that this value is an increasing function of Ψ: this latter behaviour reflects the smaller concentration gradients, and thus the higher concentrations, which occur near to the droplets in larger domains. In ad-

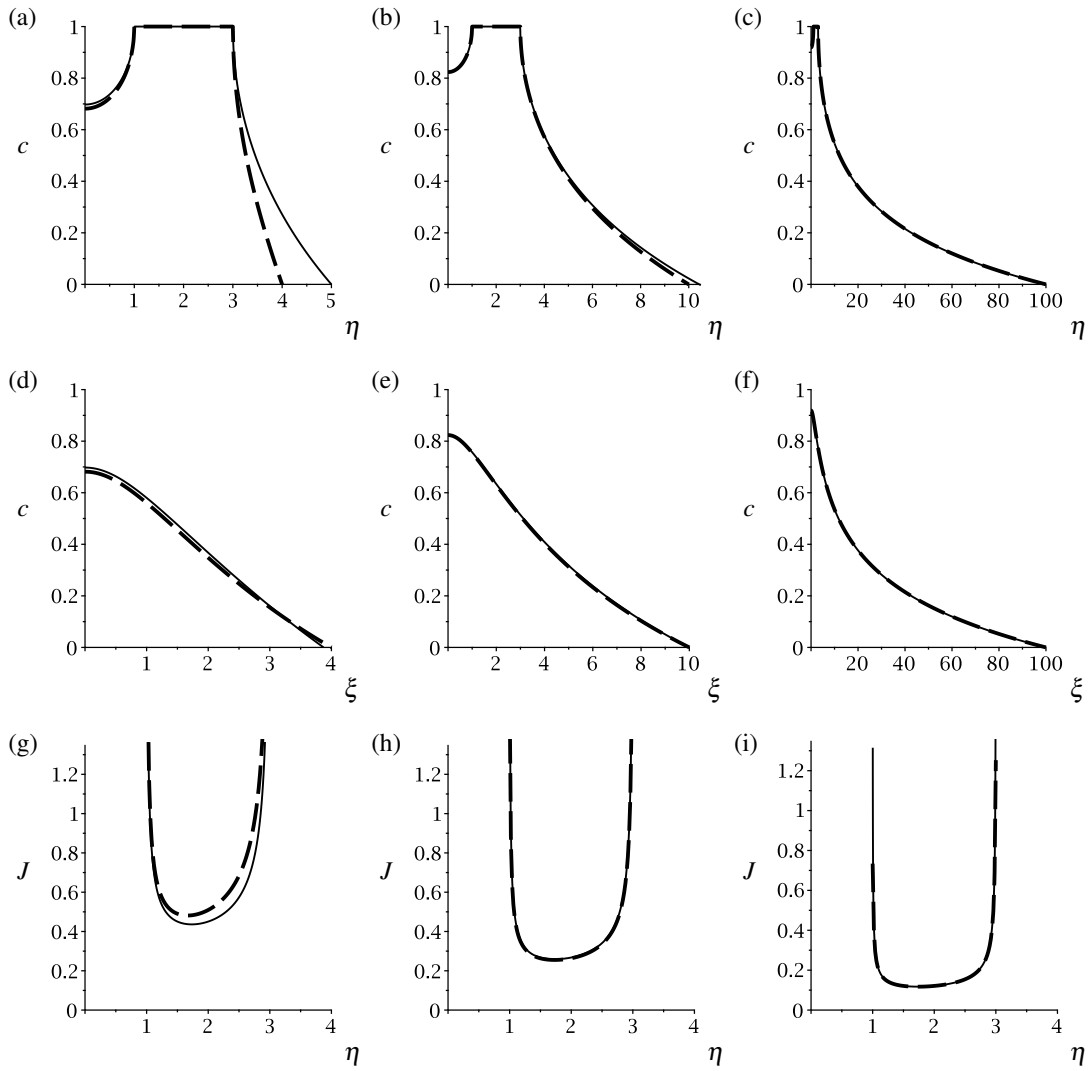

Figure 5.7: The vapour concentration and flux for the two-droplet problem for $I = 1$, $\Omega = 3$ and $\Psi = 4$ [(a), (d), (g)], $\Psi = 10$ [(b), (e), (h)], and $\Psi = 100$ [(c), (f), (i)]. (a)–(c) show solutions for the vapour concentration along the η-axis, $c(\eta, 0)$; (d)–(f) show solutions for the vapour concentration along the ξ-axis, $c(0, \xi)$; (g)–(i) show solutions for the flux, $J(\eta)$. Solid lines denote the analytical solutions in the quasi-semi-elliptical domain given by (5.45) and (5.46), and dashed lines denote the corresponding numerical solutions in the semi-circular domain.

dition, Figures 5.7(g)–(i) clearly illustrate the shielding effect that the droplets have on each other. In particular, as (5.47) shows, the flux near to the outer contact line is suppressed less by the presence of the other droplet, and so remains larger than the flux near to the inner contact line, resulting in the skewed flux profiles shown in figures 5.7(g)–(i). In particular, the minimum value of the flux no longer occurs at the centre of each droplet (as it does in the one-droplet problem).

5.3.3 Evolution and lifetime of the droplets

Using the solution for the flux given by (5.46), the evolution and lifetime of the droplets are determined by

$$\frac{\mathrm{d}A}{\mathrm{d}t} = \frac{1}{6}\frac{\mathrm{d}}{\mathrm{d}t}\left[(\Omega(t) - I(t))^2\,\theta(t)\right] = -\int_I^\Omega J(\eta)\,\mathrm{d}\eta = -\frac{\pi}{2\,\mathrm{arcsinh}\left(\Psi/\sqrt{\Omega^2 - I^2}\right)}. \quad (5.48)$$

In the one-droplet problem we investigated three modes of evaporation (namely the CR, CA and SS modes), but in the two-droplet problem there is a much richer variety of possible behaviours because any of the four contact lines may, in principle, move independently of the other three. In the present work, we consider four canonical behaviours, in each of which the droplets remain symmetric about the ξ-axis. Specifically, we consider the following modes of evaporation:

1. The constant inner and outer contact line (CIO) mode: the inner and outer contact lines of both droplets are pinned at $\eta = \pm I(0) = \pm I_0$ and $\eta = \pm\Omega(0) = \pm\Omega_0$ as the droplets evaporate.

2. The constant angle centred (CAC) mode: both droplets evaporate with constant contact angle and remain centred at $\eta = \pm(I + \Omega)/2 = \pm(I_0 + \Omega_0)/2$.

3. The constant angle and constant inner contact lines (CAI) mode: both droplets again evaporate with constant contact angle, but now their inner contact lines are pinned at $\eta = \pm I_0$.

4. The constant angle and constant outer contact line (CAO) mode: both droplets

again evaporate with constant contact angle, but now their outer contact lines are pinned at $\eta = \pm\Omega_0$.

Constant inner and outer contact line (CIO) mode

In the CIO mode, the inner and outer contact lines of both droplets are pinned, $I \equiv I_0$ and $\Omega \equiv \Omega_0 = I_0 + 2$. We may then immediately integrate (5.48) to obtain

$$\theta(t) = 1 - \frac{3\pi}{4\,\mathrm{arcsinh}\left(\Psi/\sqrt{\Omega_0^2 - I_0^2}\right)}t,$$

$$A = \frac{(\Omega_0 - I_0)^2}{6}\left[1 - \frac{3\pi}{4\,\mathrm{arcsinh}\left(\Psi/\sqrt{\Omega_0^2 - I_0^2}\right)}t\right]. \tag{5.49}$$

Hence the lifetime of a pair of droplets evaporating in the CIO mode is

$$t_{\mathrm{CIO}} = \frac{4\,\mathrm{arcsinh}\left(\Psi/\sqrt{\Omega_0^2 - I_0^2}\right)}{3\pi}. \tag{5.50}$$

Figure 5.8 shows the evolution and the lifetime of a pair of droplets evaporating in the CIO mode. As for a single droplet in the CR mode, the contact angle θ and the area A both decrease linearly with time t [figure 5.8(a,b)] and the lifetime t_{CIO} increases monotonically with Ψ [figure 5.8(c)]. In addition, since the shielding effect is weaker, and hence evaporation is faster, when the droplets are more widely separated, the lifetime t_{CIO} decreases monotonically with the separation between the droplets, $2I_0$ [figure 5.8(d)].

Constant angle (CAC, CAI, CAO) modes

In the CAC, CAI and CAO modes, the contact angle remains constant, $\theta(t) \equiv \theta_0 = 1$. The three modes are distinguished by the different behaviours of the contact lines.

In the constant angle centred (CAC) mode, the droplets remain centred at $\eta = \pm(I +$

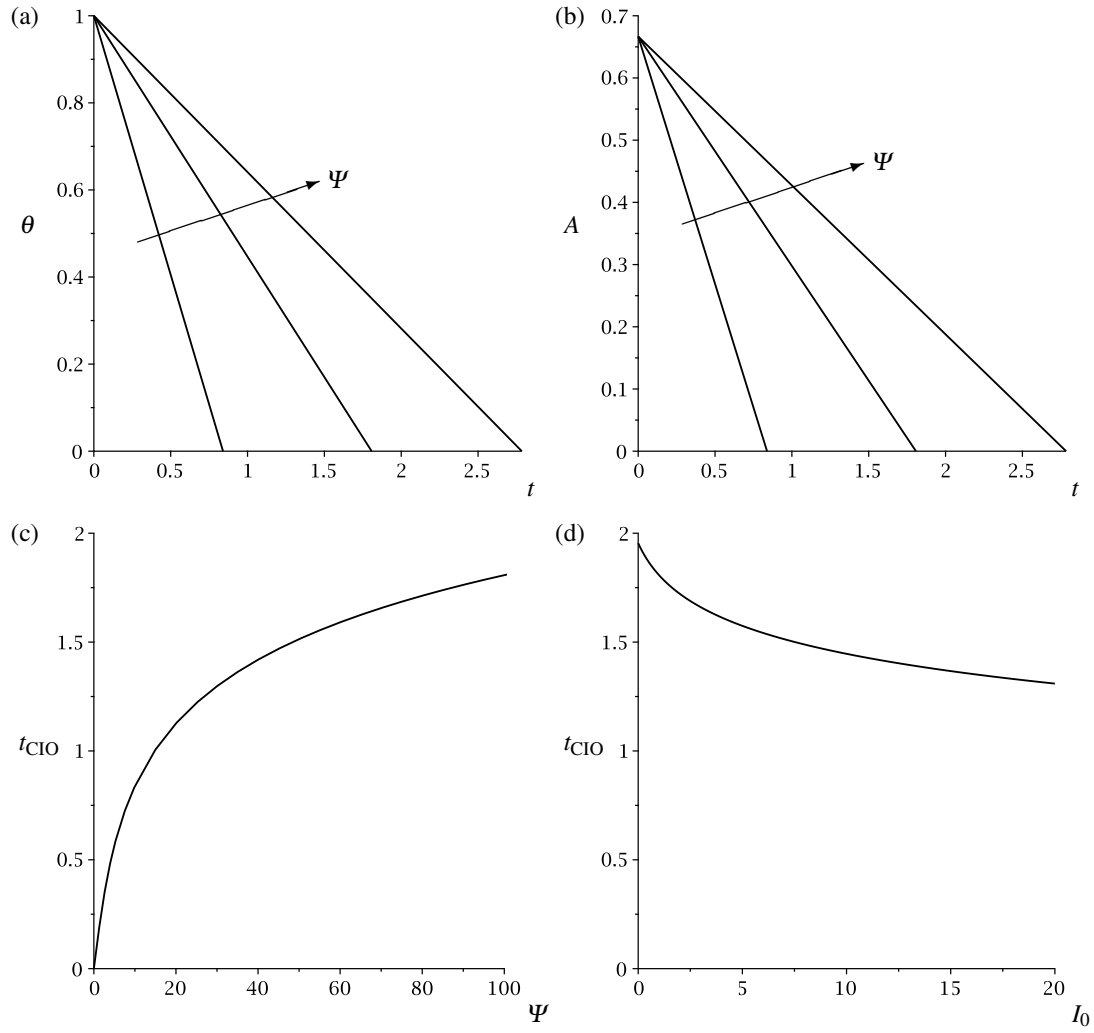

Figure 5.8: Evolution and the lifetime of a pair of droplets evaporating in the CIO mode: (a) contact angle $\theta(t)$ and (b) area $A(t)$ given by (5.49) plotted as functions of t for $\Psi = 10$, $\Psi = 100$ and $\Psi = 1000$ with the arrows indicating the direction of increasing Ψ; lifetime t_{CIO} given by (5.50) plotted (c) as a function of Ψ and (d) as a function of I_0 when $\Psi = 100$. In (a)–(c) all curves are for $I_0 = 1$ and $\Omega_0 = 3$.

$\Omega)/2 = \pm(I_0 + \Omega_0)/2$. It is therefore convenient to write

$$I(t) = \Gamma - \Delta(t), \quad \Omega(t) = \Gamma + \Delta(t) \tag{5.51}$$

where $\Gamma = (I_0+\Omega_0)/2$ is the position of the centre of the right-hand droplet and $\Delta(t) = (\Omega - I)/2$ is its semi-width. We may then integrate (5.48) implicitly to obtain

$$\begin{aligned} 18\pi\Gamma^2 t = {} & 24\Gamma^2 \left(\operatorname{arcsinh}\left(\frac{\Psi}{2\sqrt{\Gamma}}\right) - \Delta^2 \operatorname{arcsinh}\left(\frac{\Psi}{2\sqrt{\Gamma\Delta}}\right)\right) \\ & + \sqrt{4\Gamma\Delta + \Psi^2}\left(\Psi^2 - 2\Gamma\Delta\right)\Psi - \sqrt{4\Gamma + \Psi^2}\left(\Psi^2 - 2\Gamma\right)\Psi. \end{aligned} \tag{5.52}$$

Hence the lifetime of a pair of droplets evaporating in the CAC mode is

$$t_{\mathrm{CAC}} = \frac{1}{18\pi\Gamma^2}\left[24\Gamma^2 \operatorname{arcsinh}\left(\frac{\Psi}{2\sqrt{\Gamma}}\right) + \Psi^4 - \sqrt{4\Gamma + \Psi^2}\left(\Psi^2 - 2\Gamma\right)\Psi\right]. \tag{5.53}$$

In the constant angle and inner contact-line (CAI) mode, the inner contact line is pinned, $I \equiv I_0$. We may then integrate (5.48) implicitly to obtain

$$F_{\mathrm{CAI}}(\Omega) = F_{\mathrm{CAI}}(\Omega_0) + \frac{3\pi}{2}t, \tag{5.54}$$

where

$$\begin{aligned} F_{\mathrm{CAI}}(\Omega) = {} & \frac{I_0^2}{4}\left[3\operatorname{arctanh}\left(\frac{\Psi^2 - \Omega I_0 - I_0^2}{\Psi\sqrt{\Psi^2 + \Omega^2 - I_0^2}}\right) - \operatorname{arctanh}\left(\frac{\Psi^2 + \Omega I_0 - I_0^2}{\Psi\sqrt{\Psi^2 + \Omega^2 - I_0^2}}\right)\right] \\ & + \frac{\Omega}{2}\left(2I_0 - \Omega\right)\operatorname{arcsinh}\left(\frac{\Psi}{\sqrt{\Omega^2 - I_0^2}}\right) - \frac{\Psi}{2}\sqrt{\Psi^2 + \Omega^2 - I_0^2} \\ & + \Psi I_0 \ln\left(\Omega + \sqrt{\Psi^2 + \Omega^2 - I_0^2}\right). \end{aligned} \tag{5.55}$$

Hence the lifetime of a pair of droplets evaporating in the CAI mode is

$$t_{\mathrm{CAI}} = \frac{2}{3\pi}\left[F_{\mathrm{CAI}}(I_0) - F_{\mathrm{CAI}}(\Omega_0)\right]. \tag{5.56}$$

In the constant angle and outer contact line (CAO) mode, the outer contact line is

pinned, $\Omega \equiv \Omega_0$. We may then integrate (5.48) implicitly to obtain

$$F_{\mathrm{CAO}}(I) = F_{\mathrm{CAO}}(I_0) + \frac{3\pi}{2}t, \tag{5.57}$$

where[1]

$$\begin{aligned} F_{\mathrm{CAO}}(I) = \frac{\Omega_0^2}{4}\left[3\,\mathrm{arctanh}\left(\frac{\Psi^2+\Omega_0 I+\Omega_0^2}{\Psi\sqrt{\Psi^2+\Omega_0^2-I^2}}\right) - \mathrm{arctanh}\left(\frac{\Psi^2-\Omega_0 I+\Omega_0^2}{\Psi\sqrt{\Psi^2+\Omega_0^2-I^2}}\right)\right] \\ + \frac{I}{2}\left(2\Omega_0 - I\right)\mathrm{arcsinh}\left(\frac{\Psi}{\sqrt{\Omega_0^2-I^2}}\right) + \frac{\Psi}{2}\sqrt{\Psi^2+\Omega_0^2-I^2} \\ + \Psi\Omega_0\arctan\left(\frac{I}{\sqrt{\Psi^2+\Omega_0^2-I^2}}\right). \end{aligned} \tag{5.58}$$

Hence the lifetime of a pair of droplets evaporating in the CAO mode is

$$t_{\mathrm{CAO}} = \frac{2}{3\pi}\left[F_{\mathrm{CAO}}(\Omega_0) - F_{\mathrm{CAO}}(I_0)\right]. \tag{5.59}$$

Figure 5.9 shows the evolution and the lifetime of a pair of droplets evaporating in the three constant angle modes. The difference between the modes is most clearly seen in figure 5.9(a), which shows the inner and outer contact lines moving towards the centre of the droplet in the CAC mode, the outer contact line moving inward in the CAI mode, and the inner contact line moving outward in the CAO mode. Despite these differences, the evolution of the area A, which decreases nonlinearly with t, is similar for all three modes [figure 5.9(b)]. As in the CAI mode, the lifetimes t_{CAC}, t_{CAI} and t_{CAO} increase monotonically with Ψ [figure 5.9(c)] and decrease monotonically with the separation between the droplets, $2I_0$, [figure 5.9(d)].

As figures 5.9(c,d) show, the lifetimes of the three constant angle modes are very similar, and it is only when the separation between the droplets is small that the difference between them becomes important. Specifically, figure 5.9(d) shows that the difference between t_{CAC}, t_{CAI} and t_{CAO} becomes negligible when $I_0 \gtrsim 5$ (i.e. when the droplet

[1] Note that, as a check on the correctness of (5.55) and (5.58), we may (up to an unimportant additive constant) recover F_{CAO} from F_{CAI} by replacing Ω with I, I_0 with Ω_0 and Ψ with $\mathrm{i}\Psi$ in (5.55), and F_{CAI} from F_{CAO} by replacing I with Ω, Ω_0 with I_0 and Ψ with $\mathrm{i}\Psi$ in (5.58).

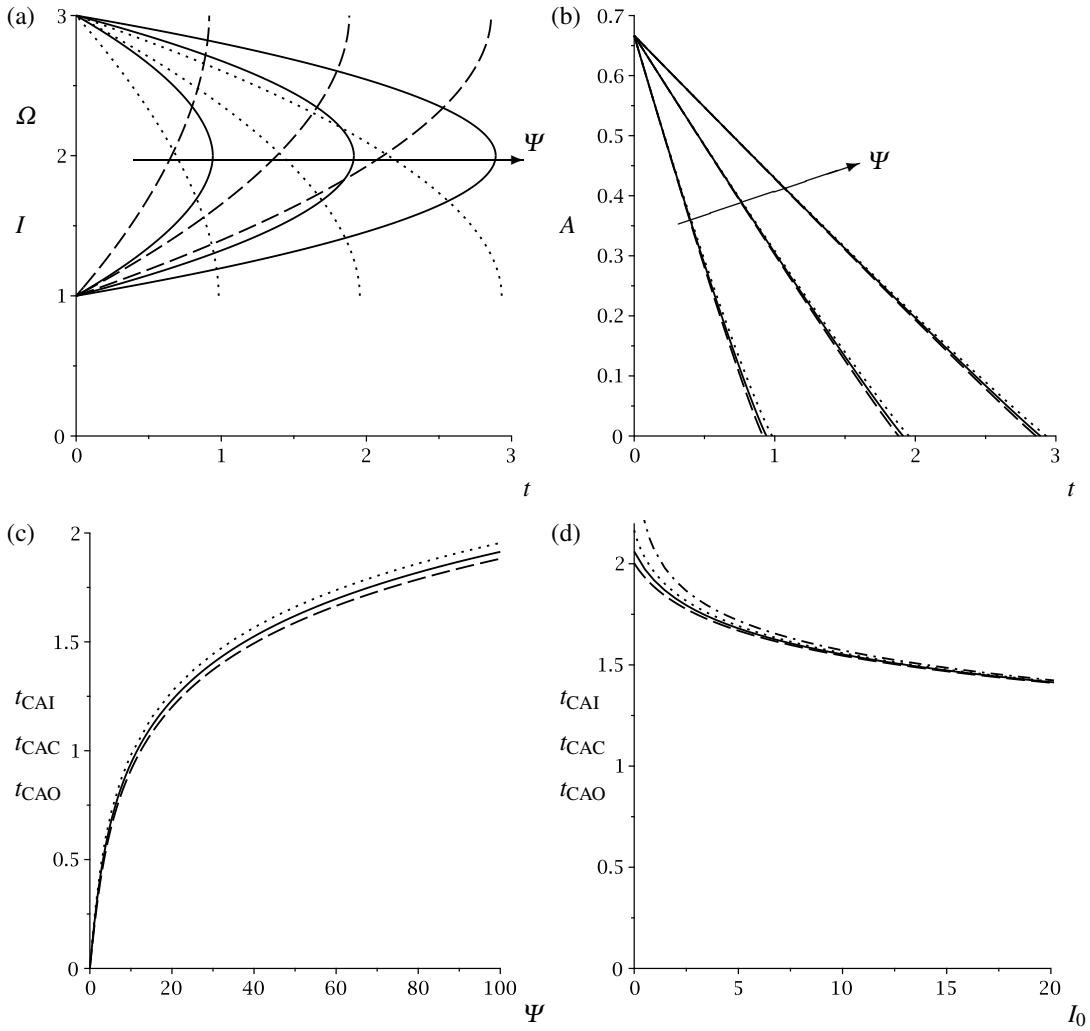

Figure 5.9: Evolution and lifetime of a pair of droplets evaporating in the CAC (solid lines), CAI (dotted lines), and CAO (dashed lines) modes: (a) contact line positions $I(t)$, $\Omega(t)$ and (b) area $A(t)$ given by (5.40), (5.52), (5.54) and (5.57) plotted as functions of t for $\Psi = 10$, $\Psi = 100$ and $\Psi = 1000$ with the arrows indicating the direction of increasing Ψ; lifetimes t_{CAC}, t_{CAI} and t_{CAO} given by (5.53), (5.56) and (5.59) plotted (c) as functions of Ψ and (d) as functions of I_0 for $\Psi = 100$. In (a)–(c) all curves are for $I_0 = 1$ and $\Omega_0 = 3$, while (d) also includes the leading-order behaviour in the asymptotic regime $1 \ll I_0 \ll \Psi$ given by $4/(3\pi)\ln(\Psi/\sqrt{I_0})$ (dot-dashed line).

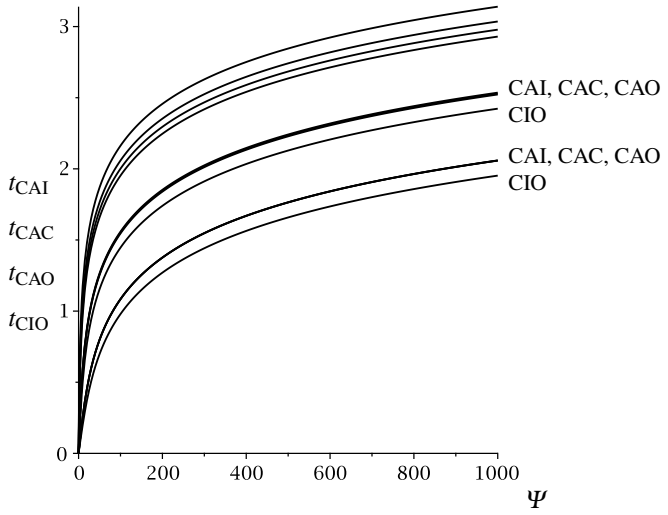

Figure 5.10: Lifetimes of a pair of droplets evaporating in the CAI (top curve in each set), CAC, CAO and CIO (bottom curve in each set) modes given by (5.50), (5.53), (5.56) and (5.59) plotted as functions of Ψ when $I_0 = 0$ (top set of curves), $I_0 = 10$ and $I_0 = 100$ (bottom set of curves).

separation is several times the width of the droplets). As the droplets evaporate, the droplet separation is smallest in the CAI mode and largest in the CAO mode, resulting in the slowest evaporation, and hence the longest lifetime, in the CAI mode and the fastest evaporation, and hence the shortest lifetime, in the CAO mode. This point is further illustrated by figure 5.10, which shows the lifetimes t_{CAI}, t_{CAC}, t_{CAO} and t_{CIO} plotted as functions of Ψ. In particular, figure 5.10 shows that as the droplet separation increases the lifetimes of the three constant angle modes (but not that of the CIO mode) become virtually indistinguishable. We will discuss the latter behaviour in more detail in section 5.3.3 below.

Asymptotic behaviour of the lifetimes in a large domain, $\Psi \gg I$

The results shown in figure 5.10 motivate us to derive asymptotic expressions for the lifetimes of the droplets when $\Psi \gg I$. Noting the difference between closely-spaced and widely-separated droplets, we consider the regimes $I_0 \ll 1$ and $I_0 \gg 1$ separately.

In the regime $I_0 \ll 1 \ll \Psi$, the initial droplet separation is much less than the initial

droplet semi-width. Equations (5.50), (5.53), (5.56) and (5.59) then yield

$$t_{\mathrm{CIO}} = \frac{4}{3\pi}\ln(\Psi) - \frac{2I_0}{3\pi} + O\left({I_0}^2, \frac{1}{\Psi^2}\right), \tag{5.60}$$

$$t_{\mathrm{CAC}} = \frac{4}{3\pi}\ln(\Psi) + \frac{1}{3\pi} - \frac{2I_0}{3\pi} + O\left({I_0}^2, \frac{1}{\Psi^2}\right), \tag{5.61}$$

$$t_{\mathrm{CAI}} = \frac{4}{3\pi}\ln(\Psi) + \frac{2}{3\pi} - \frac{4I_0}{3\pi} + O\left({I_0}^2\log I_0, \frac{1}{\Psi^2}\right), \tag{5.62}$$

$$t_{\mathrm{CAO}} = \frac{4}{3\pi}\ln(\Psi) + \frac{2}{\pi}\left(1 - \frac{4}{3}\ln 2\right) + \frac{4I_0}{3\pi}(1 - 2\ln 2) + O\left({I_0}^2, \frac{1}{\Psi^2}\right), \tag{5.63}$$

respectively.

On the other hand, in the regime $1 \ll I_0 \ll \Psi$, the initial droplet separation is much greater than the initial droplet semi-width. Equations (5.50), (5.53), (5.56) and (5.59) then yield

$$t_{\mathrm{CIO}} = \frac{4}{3\pi}\ln\left(\frac{\Psi}{\sqrt{I_0}}\right) - \frac{2}{3\pi I_0} + O\left(\frac{1}{I_0^2}, \frac{I_0}{\Psi^2}\right), \tag{5.64}$$

$$t_{\mathrm{CAC}} = \frac{4}{3\pi}\ln\left(\frac{\Psi}{\sqrt{I_0}}\right) + \frac{1}{3\pi} - \frac{2}{3\pi I_0} + O\left(\frac{1}{I_0^2}, \frac{I_0}{\Psi^2}\right), \tag{5.65}$$

$$t_{\mathrm{CAI}} = \frac{4}{3\pi}\ln\left(\frac{\Psi}{\sqrt{I_0}}\right) + \frac{1}{3\pi} - \frac{4}{9\pi I_0} + O\left(\frac{1}{I_0^2}, \frac{I_0}{\Psi^2}\right), \tag{5.66}$$

$$t_{\mathrm{CAO}} = \frac{4}{3\pi}\ln\left(\frac{\Psi}{\sqrt{I_0}}\right) + \frac{1}{3\pi} - \frac{8}{9\pi I_0} + O\left(\frac{1}{I_0^2}, \frac{I_0}{\Psi^2}\right), \tag{5.67}$$

respectively.

Equations (5.60)–(5.67) show that, as in the one-droplet problem, in the regime $\Psi \gg I$, the lifetimes of all four modes depend logarithmically on the size of the domain.

When $I_0 \ll 1$, equations (5.60)–(5.63) show that the lifetimes depend on the mode of evaporation at $O(1)$. The lifetime of the CIO mode is the shortest because, due to their pinned contact lines, the droplets in this mode have the largest surface area, and hence evaporate the fastest. Of the three constant angle modes, the CAO mode has the shortest lifetime and the CAI mode the longest lifetime. This is because when the inner contact lines are pinned the droplets remain closer together and hence evaporate more slowly than in the CAC mode due to a stronger shielding effect, whereas when

the outer contact lines are pinned the droplets move further apart and hence evaporate more quickly than in the CAC mode due to a weaker shielding effect.

On the other hand, when $I_0 \gg 1$, equations (5.64)–(5.67) show that the influence of the different behaviours of the contact lines on the three constant angle modes is very weak and at $O(1)$ the lifetimes of the CAC, CAI and CAO modes all coincide with each other, but differ from the lifetime of the CIO mode by $1/(3\pi)$.

5.4 Comparison between the lifetimes of a single droplet and a pair of droplets

To provide further insight into the shielding effect the droplets have on each other, we compare the lifetimes of a single droplet and a pair of droplets in dimensional terms. For simplicity, we consider only the leading-order behaviour of the lifetimes in the regime of most interest in which the domain is large and approximately semi-circular with radius $\hat{\Psi}$.

Our reference point is the lifetime of a single droplet with initial semi-width $\hat{R}_0$, which from (5.1), (5.37) and (5.38) is given by

$$\hat{t}_{\text{single}} \sim \frac{2}{3\pi} \ln\left(\frac{2\hat{\Psi}}{\hat{R}_0}\right) \hat{T}, \qquad \text{where} \qquad \hat{T} = \frac{\hat{\rho}\hat{\theta}_0 \hat{R}_0^2}{\hat{D}(\hat{c}_{\text{sat}} - \hat{c}_\infty)}. \tag{5.68}$$

A first natural comparison is with a pair of droplets, each with initial semi-width $\hat{R}_0/2$, which together have the same total surface area as the single droplet (i.e. their initial separation is $2\hat{I}_0 = 0$). In this case the vapour concentration and flux are identical in the two problems. However, the lifetimes are not the same, because the cross-sectional area of the single droplet is twice the total cross-sectional area of the two droplets. Specifically, from (5.60)–(5.63) we obtain

$$\hat{t}_{\text{area}} \sim \frac{4}{3\pi} \frac{\hat{\rho}\hat{\theta}_0 (\hat{R}_0/2)^2}{\hat{D}(\hat{c}_{\text{sat}} - \hat{c}_\infty)} \ln\left(\frac{\hat{\Psi}}{\hat{R}_0/2}\right) = \frac{1}{3\pi} \ln\left(\frac{2\hat{\Psi}}{\hat{R}_0}\right) \hat{T}, \tag{5.69}$$

so that, as expected, the lifetime of the pair of droplets is half that of the single droplet, i.e. $\hat{t}_{\text{area}} \sim \hat{t}_{\text{single}}/2$.

Alternatively, we can consider the same total cross-sectional area of fluid, arranged either as two closely-spaced or two widely-separated droplets. In both cases the droplets have initial semi-width $\hat{R}_0/\sqrt{2}$. If the droplets are closely spaced then from (5.60)–(5.63) we obtain

$$\hat{t}_{\text{close}} \sim \frac{4}{3\pi}\frac{\hat{\rho}\hat{\theta}_0(\hat{R}_0/\sqrt{2})^2}{\hat{D}(\hat{c}_{\text{sat}}-\hat{c}_\infty)}\ln\left(\frac{\hat{\Psi}}{\hat{R}_0/\sqrt{2}}\right) = \frac{2}{3\pi}\left[\ln\left(\frac{2\hat{\Psi}}{\hat{R}_0}\right)-\frac{1}{2}\ln 2\right]\hat{T}. \tag{5.70}$$

At leading order the lifetime of the pair of droplets is the same as that of the single droplet, but there is a negative $O(1)$ correction because the two droplets have a larger total surface area than the single droplet. On the other hand, if the droplets are widely separated then from (5.64)–(5.67) we obtain

$$\hat{t}_{\text{wide}} \sim \frac{4}{3\pi}\frac{\hat{\rho}\hat{\theta}_0(\hat{R}_0/\sqrt{2})^2}{\hat{D}(\hat{c}_{\text{sat}}-\hat{c}_\infty)}\ln\left(\frac{\hat{\Psi}}{\hat{R}_0/\sqrt{2}}\sqrt{\frac{\hat{R}_0/\sqrt{2}}{\hat{I}_0}}\right) = \frac{2}{3\pi}\left[\ln\left(\frac{2\hat{\Psi}}{\hat{R}_0}\right)-\frac{1}{2}\ln\left(2^{3/2}\frac{\hat{I}_0}{\hat{R}_0}\right)\right]\hat{T}. \tag{5.71}$$

At leading order the lifetime of the pair of droplets is again the same as that of the single droplet, but now there is a larger negative $O(\ln(\hat{I}_0/\hat{R}_0))$ correction due to a weaker shielding effect when the droplets are widely separated.

To illustrate these results we take the representative parameter values $\hat{\rho} = 998\,\text{kg}\,\text{m}^{-3}$, $\hat{D} = 2.44\times10^{-5}\,\text{m}^2\,\text{s}^{-1}$, $\hat{c}_{\text{sat}} = 1.94\times10^{-2}\,\text{kg}\,\text{m}^{-3}$ and $\hat{c}_\infty = 7.76\times10^{-3}\,\text{kg}\,\text{m}^{-3}$, corresponding to water at 295 K, evaporating into an environment with ambient vapour concentration $\hat{c}_\infty = 0.4\,\hat{c}_{\text{sat}}$ [51]. We further take $\hat{\Psi} = 1\,\text{m}$ together with $\hat{\theta}_0 = 0.1$ and $\hat{R}_0 = 1\,\text{mm}$, so that the droplet has a cross-sectional area of approximately $6.7\times10^{-8}\,\text{m}^2$.

With these parameter values, the timescale $\hat{T} \approx 351\,\text{s}$ and the lifetime of a single droplet is $\hat{t}_{\text{single}} \approx 567\,\text{s}$. The lifetime of a pair of droplets with the same total surface area as the single droplet is $\hat{t}_{\text{area}} \approx 283\,\text{s}$. The lifetime of two closely-spaced droplets with the same total cross-sectional area as the single droplet is $\hat{t}_{\text{close}} \approx 541\,\text{s}$, whereas the lifetime

of two widely-separated droplets with the same total cross-sectional area as the single droplet is $\hat{t}_{\text{wide}} \approx 442\,\text{s}$ if the droplets are separated by $2\hat{I}_0 = 2\,\text{cm}$, and $\hat{t}_{\text{wide}} \approx 356\,\text{s}$ if the droplets are separated by $2\hat{I}_0 = 20\,\text{cm}$.

5.5 Conclusions

In this chapter, we considered the diffusion-limited evaporation of thin two-dimensional sessile droplets either singly or in a pair. This two-dimensional problem is qualitatively different from the corresponding three-dimensional problem because, in contrast to in three dimensions, in two dimensions the size of the domain remains important even when it is much larger than the width of the droplets; it is therefore not possible to obtain a solution to the two-dimensional problem with a far-field boundary condition imposed "at infinity". We therefore formulated a slightly modified problem in which the far-field condition was replaced by a relaxed condition at a distant, but finite, boundary. We then showed how a conformal-mapping technique may be used to calculate the vapour concentrations, and hence obtain closed-form solutions for the evolution and the lifetimes of the droplets in various modes of evaporation. These solutions demonstrate that in large domains the lifetimes of the droplets depend logarithmically on the size of the domain, and more weakly on the mode of evaporation and the separation between the droplets. In particular, they allowed us to quantify the shielding effect that the droplets have on each other, and how it extends the lifetimes of the droplets.

Chapter 6

Conclusions and Further Work

6.1 Conclusions

In this thesis we have investigated the evaporation of both axisymmetric and 2D droplets. In particular, we have studied the influence of thermal properties and of neighbouring droplets on the evaporation rate, and hence lifetimes, of evaporating droplets.

In chapters 1 and 2 we discussed relevant work by previous authors, and formulated the diffusion-limited model of droplet evaporation.

In chapter 3 we considered the evaporation of an axisymmetric sessile droplet on a variety of substrates with different thermal conductivities, for the full range of initial contact angles. We used a finite element-based approach to obtain the vapour and temperature fields produced by an evaporating droplet, and thus obtained the evaporation rate, and hence the lifetime, of a droplet evaporating in the constant radius (CR) and constant angle (CA) modes of evaporation. In general, a warmer droplet will evaporate faster than a cooler one. Therefore, physical situations which reduce the magnitude of evaporative cooling, such as a higher thermal conductivity of the substrate, reduce the droplet lifetime.

We found that a droplet evaporating in the CR mode will evaporate faster than a

droplet evaporating in the CA mode, since the free-surface area is larger in the CR mode than in the CA mode. We also found that for droplets with large contact angles, the lifetime of the droplet depends far less on the thermal conductivity of the substrate than for droplets with a relatively larger droplet-substrate interface.

In chapter 4 we restricted our attention to thin droplets evaporating on thin substrates, allowing us to obtain analytical expressions for the vapour and temperature fields produced by an evaporating droplet. Hence we obtained the evaporation rate, and hence lifetime, of a droplet evaporating in the CR, CA, stick-slide (SS) and stick-jump (SJ) modes of evaporation. In particular, we identified two regimes when the influence of the thermal properties of the system are strong in which we could obtain closed-form asymptotic expressions for the droplet lifetime, namely, when the droplet is far more thermally conductive than the substrate, and when the saturation concentration of vapour is highly dependent on temperature. In both of these regimes we find that the droplet evaporates on a different timescale to that when the saturation concentration is independent of temperature. Furthermore, in all regimes we found that a thin droplet evaporating in the CA mode always lives longer than one evaporating in the SS or SJ modes, which in turn lives longer than one evaporating in the CR mode.

In chapter 5 we considered the evaporation of thin two-dimensional sessile droplets either singly or in a pair using the thermally-decoupled model. We used a conformal-mapping technique to obtain the vapour concentrations, and hence obtained closed-form solutions for the evolution and the lifetimes of the droplets in the CR, CA and SS modes of evaporation. We found that, in contrast to the axisymmetric case, the lifetime of a two-dimensional droplet depends logarithmically on the size of the atmosphere, and more weakly on the mode of evaporation and the separation between the droplets. In particular, we quantified the shielding effect that two neighbouring droplets have on each other, and how it extends the lifetime of the droplets.

6.2 Further Work

We are unaware of any previous physical experiments against which the present theoretical predictions can be validated, but hope that our work will inspire one or more of the many experimental groups with an interest in evaporating droplets to conduct such experiments in the future.

The work presented in this thesis suggests many possible opportunities for future research. Three specific examples include the evaporation of multiple droplets in three dimensions, further investigation of the evaporative flux near the contact line, and investigation into the coffee-stain effect produced by evaporation of multiple 2D droplets.

6.2.1 Evaporation of multiple droplets in three dimensions

One clear direction for future work is to extend the finite element analysis carried out in chapter 3 to include more than one evaporating droplet. As we discussed in section 1.5, the simultaneous evaporation of multiple droplets is of considerable industrial and academic interest. We have carried out preliminary work in this direction and have produced a proof-of-concept for a multi-droplet numerical implementation of the thermally-decoupled model, which allows for multiple droplets to evaporate in close proximity. The multi-droplet numerical model does not have the advantage of being axisymmetric, and therefore the entire 3D system has to be meshed and solved for. This means that the multi-droplet numerical model is more computationally demanding than the numerical model described in section 3. To reduce computational demands, we have so far only considered the evaporation of thin droplets $\hat{\theta} \ll 1$, which may be implemented as flat discs within the numerical model.

Figure 6.1 shows the numerically evaluated contour plots of the flux $\hat{J}$ for a pair of identical thin droplets. The droplets each have a contact radius $\hat{R} = 1$ mm and are 0.2 mm apart at their nearest points. The contour values are greatest on the contact line of the droplet. As observed by Wray *et al.* [161], and as shown in figures 5.7(g)–(i)

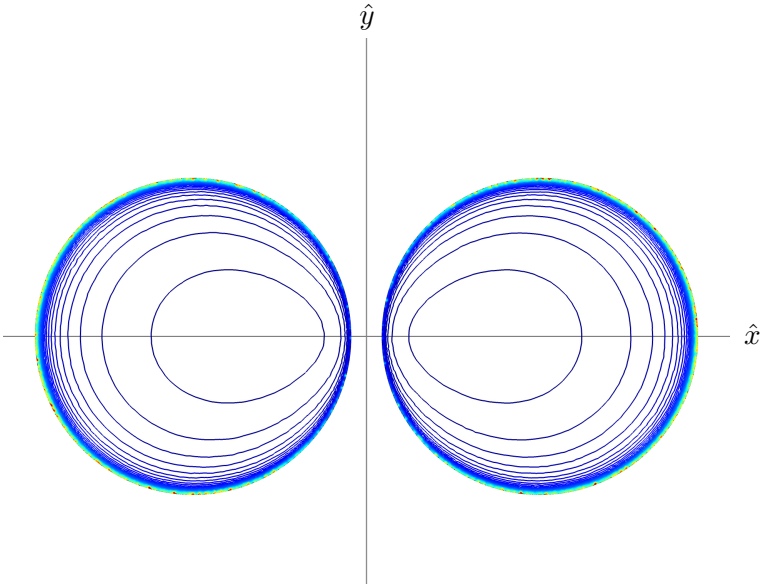

Figure 6.1: Top-down view of the numerically evaluated contour plots of the flux $\hat{J}$ for a pair of identical thin droplets. The droplets each have a contact radius $\hat{R} = 1$ mm and are 0.2 mm apart at their nearest points.

for the corresponding two dimensional problem, the location of the smallest flux is not at the centre of each droplet, as it is in the case of an isolated droplet, but is offset towards the neighbouring droplet. This is caused by the shielding effect we discussed in chapter 5.

The next step would be to extend the multi-droplet numerical model by coupling the thermal effects and the vapour distribution as we did in chapter 3, to obtain a thermally-coupled multi-droplet numerical model. Future work could investigate not only the interactions between neighbouring droplets through the atmospheric vapour concentration, but also the interactions between droplets through the atmospheric and substrate temperature fields.

6.2.2 Further investigation of the flux near to the contact line

Another direction for future work is a further investigation of the flux near to the contact line. Throughout this thesis we have seen that, in general, for low-wetting droplets $\hat{J} \to \infty$ at the contact line. However, for high-wetting droplets, particularly in situations where $\hat{c}_{\text{sat}}$ is nearly uniform on the free surface of the droplet, we find

$\hat{J} \to 0$, as discussed in section 3.4.1.

Using the thermally-decoupled model, Deegan *et al.* [38], and later Ristenpart *et al.* [112] have already analytically investigated the local thermally-decoupled problem for flux near to the contact line of a droplet. In polar coordinates $\hat{r}, \hat{\Theta}$ centred at the contact line, the thermally-decoupled problem for the vapour is given by

$$\hat{\nabla}^2 \hat{c} = 0 \qquad \text{in } \hat{\theta} < \hat{\Theta} < \pi, \tag{6.1}$$

subject to

$$\hat{c} = \hat{c}_{\text{sat}} \qquad \text{on } \hat{\theta} = \hat{\Theta}, \tag{6.2}$$

and

$$\frac{1}{\hat{r}} \frac{\partial \hat{c}}{\partial \hat{\Theta}} = 0 \qquad \text{on } \hat{\Theta} = \pi. \tag{6.3}$$

From equation (6.1) and conditions (6.2) and (6.3) Deegan *et al.* [38] found $\hat{J} \propto \hat{r}^{-\lambda}$, where $\lambda = (\pi - 2\hat{\theta})/(2\pi - 2\hat{\theta})$. Hu and Larson [65] later suggested an approximate expression for $\hat{J}$, namely

$$\hat{J} \approx \hat{J}_0 (2\hat{r} \cos\hat{\theta})^{-1/2+\hat{\theta}/\pi}, \tag{6.4}$$

which is valid for $0 < \hat{\theta} < \pi/2$. Note, an exact solution

$$\hat{J} = -\hat{D} \frac{1}{\hat{r}} \frac{\partial \hat{c}}{\partial \hat{\Theta}} = \frac{\hat{D} A^c \lambda \hat{r}^{\lambda - 1}}{\sin \lambda \hat{\Theta}}, \tag{6.5}$$

can be obtained.

Ristenpart *et al.* [112] used the approximate solution (6.4) and the evaporative cooling condition (2.48) on the free surface of the droplet to investigate how thermal gradients, and thus thermal Marangoni flow, can be reversed near the contact line of a droplet. A direction in which to further investigate the evaporative flux near to the contact line is

to carry out a similar analysis to Ristenpart *et al.* [112] using the exact solution (6.5) instead of the approximate solution (6.4).

Ristenpart *et al.* [112] assume that $\hat{k}^{\mathrm{a}} \ll \hat{k}^{\mathrm{s}}$ and $\hat{k}^{\mathrm{a}} \ll \hat{k}$, and therefore, as we have discussed in section 2.3.2, atmospheric temperature is decoupled from the temperature of the substrate and droplet. Following Ristenpart *et al.* [112], using the exact expression for λ, we have carried out preliminary work which shows that more general self-similar solutions for the temperature near to the contact line can be obtained with no assumptions on $\hat{k}$, $\hat{k}^{\mathrm{s}}$ or $\hat{k}^{\mathrm{a}}$.

The approximate solution quoted by Ristenpart *et al.* [112] and the exact solution discussed here both assume that $\hat{c}_{\mathrm{sat}}$ is constant on the free surface of the droplet. Thus, we have $\hat{J} \to 0$ for high-wetting droplets and $\hat{J} \to \infty$ for low-wetting droplets. Future work could also try to investigate the thermally-coupled corner problem, *i.e.* the equivalent corner problem for the thermally-coupled model described in chapter 2. Such an investigation could help explain the behaviour shown in figure 3.10(i), where we see both $\hat{J} \to 0$ and $\hat{J} \to \infty$ behaviours for a high-wetting droplet on two different substrates.

6.2.3 Study of the coffee-stain effect in 2D droplet evaporation

As noted in section 1.7, the work discussed in Chapter 5 concerns two-dimensional droplets. While truly two-dimensional droplets are, of course, only possible in theory, we can expect the results obtained to relate to physical experiments of quasi-two-dimensional liquid lines (see, for example, Dinh *et al.* [46]) provided that the "heads" and "tails" of the lines do not contribute significantly to the overall evaporation, *i.e.* provided that the lines are sufficiently long.

A potential study which could yield qualitatively similar results to those shown in Chapter 5 would be a study of the coffee-stain effect produced by two particle-laden liquid lines evaporating in close proximity. As, for example, Deegan *et al.* [38] have shown, the distribution of deposit left by an evaporating droplet depends strongly on

the evaporation rate at the contact line of the droplet. Given the results of the work in Chapter 5, we would expect a study of two particle-laden liquid lines evaporating in close proximity to produce larger deposits on the outer edges of each droplet footprint (where the evaporative flux is relatively high) than on the inner edges of each droplet footprint (where the evaporative flux is relatively low).

Appendix A

Toroidal coordinates

In section 3.2.3 we introduce the toroidal coordinate

$$\tau = \frac{1}{2} \ln \left(\frac{(\hat{r} + \hat{R})^2 + \hat{z}^2}{(\hat{r} - \hat{R})^2 + \hat{z}^2} \right) \geq 0, \tag{A.1}$$

which parameterises the free surface of a droplet with contact radius $\hat{R}$ and contact angle $\hat{\theta}$, and which is related to the cylindrical polar coordinates $(\hat{r}, \hat{z})$ by

$$\hat{r} = \hat{R} \frac{\sinh \tau}{\cosh \tau + \cos \hat{\theta}}, \tag{A.2}$$

$$\hat{z} = \hat{R} \frac{\sin \hat{\theta}}{\cosh \tau + \cos \hat{\theta}}, \tag{A.3}$$

where $\tau = 0$ gives the apex of the droplet $(0, \hat{R} \tan(\hat{\theta}/2))$ and $\tau = \infty$ gives the contact line $(\hat{R}, 0)$. Figure A.1 shows the free surface of a droplet with contact radius $\hat{R}$ and contact angle $\hat{\theta}$, described implicitly as a function of τ in equation (A.1).

Several authors, for example [39, 75, 95, 105], use toroidal coordinates to present the exact solution to the diffusion-limited evaporation problem for a perfectly spherical droplet. In the present work, we use toroidal coordinates to investigate contact line behaviour of our numerical model as shown in figure 3.2.

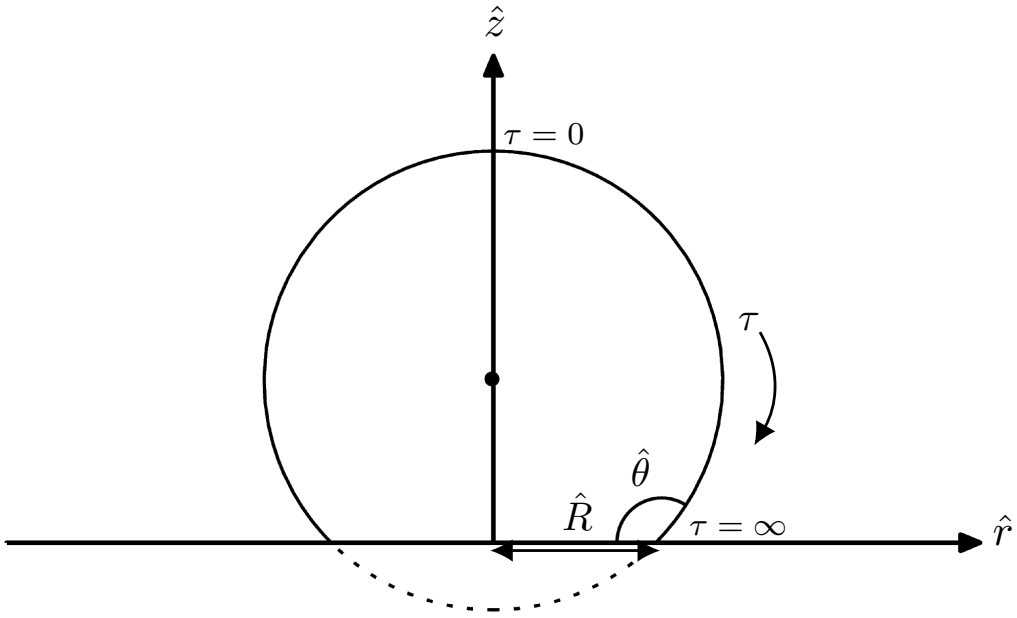

Figure A.1: The free surface of a droplet with contact radius $\hat{R}$ and contact angle $\hat{\theta}$, described implicitly as a function of τ in equation (A.1).

Bibliography

[1] COMSOL Multiphysics v. 5.4. `www.comsol.com`. COMSOL AB, Stockholm, Sweden.

[2] E. Adachi, A. S. Dimitrov, and K. Nagayama. Stripe patterns formed on a glass surface during droplet evaporation. *Langmuir*, 11(4):1057–1060, 1995. doi: 10.1021/la00004a003.

[3] M. Ait Saada, S. Chikh, and L. Tadrist. Numerical investigation of heat mass transfer of an evaporating sessile drop on a horizontal surface. *Physics of Fluids*, 22:112115, 2010. doi: 10.1063/1.3488676.

[4] M. Ait Saada, S. Chikh, and L. Tadrist. Effect of substrate thickness and thermal conductivity on an evaporating sessile drop. *Journal of Physics Conference Series*, 395:2140, 2012. doi: 10.1088/1742-6596/395/1/012140.

[5] M. Ait Saada, S. Chikh, and L. Tadrist. Evaporation of a sessile drop with pinned or receding contact line on a substrate with different thermophysical properties. *International Journal of Heat and Mass Transfer*, 58:197208, 2013. doi: 10.1016/j.ijheatmasstransfer.2012.11.026.

[6] M. Ait Saada, S. Chikh, and L. Tadrist. A numerical study of particle transport in an evaporating colloidal sessile droplet. *Interfacial Phenomena and Heat Transfer*, 4:217–233, 2017. doi: 10.1615/InterfacPhenomHeatTransfer.2017019419.

[7] V. S. Ajaev. Spreading of thin volatile liquid droplets on uniformly heated surfaces. *Journal of Fluid Mechanics*, 528:279–296, 2005. doi: 10.1017/S0022112005003320.

[8] V. S. Ajaev and G. Homsy. Steady vapor bubbles in rectangular microchannels. *Journal of Colloid and Interface Science*, 240(1):259–271, 2001. doi: 10.1006/jcis.2001.7562.

[9] V. S. Ajaev and G. Homsy. Modeling shapes and dynamics of confined bubbles. *Annual Review of Fluid Mechanics*, 38(1):277–307, 2006. doi: 10.1146/annurev.fluid.38.050304.092033.

[10] V. S. Ajaev and O. A. Kabov. Heat and mass transfer near contact lines on heated surfaces. *International Journal of Heat and Mass Transfer*, 108:918–932, 2017. doi: 10.1016/j.ijheatmasstransfer.2016.11.079.

[11] A. Amini and G. M. Homsy. Evaporation of liquid droplets on solid substrates. I. Flat substrate with pinned or moving contact line. *Physical Review Fluids*, 2:043603, 2017. doi: 10.1103/PhysRevFluids.2.043603.

[12] A. Amini and G. M. Homsy. Evaporation of liquid droplets on solid substrates. II. Periodic substrates with moving contact lines. *Physical Review Fluids*, 2:043604, 2017. doi: 10.1103/PhysRevFluids.2.043604.

[13] N. Anantharaju, M. Panchagnula, and S. Neti. Evaporating drops on patterned surfaces: Transition from pinned to moving triple line. *Journal of Colloid and Interface Science*, 337(1):176–182, 2009. doi: 10.1016/j.jcis.2009.04.095.

[14] I. Argatov and I. Sevostianov. On relations between geometries of microcontact clusters and their overall properties. *International Journal of Engineering Science*, 47(10):959–973, 2009. doi: j.ijengsci.2009.06.001.

[15] I. I. Argatov. Electrical contact resistance, thermal contact conductance and elastic incremental stiffness for a cluster of microcontacts: Asymptotic modelling. *The Quarterly Journal of Mechanics and Applied Mathematics*, 64(1):1–24, 2010. doi: 10.1093/qjmam/hbq018.

[16] I. I. Argatov. The contact problem for a periodic cluster of microcontacts. *Journal*

of Applied Mathematics and Mechanics, 76(5):604–610, 2012. doi: 10.1016/j.jappmathmech.2012.11.004.

[17] A. Askounis, D. Orejon, V. Koutsos, K. Sefiane, and M. E. R. Shanahan. Nanoparticle deposits near the contact line of pinned volatile droplets: size and shape revealed by atomic force microscopy. *Soft Matter*, 7:4152–4155, 2011. doi: 10.1039/C1SM05241A.

[18] A. Askounis, K. Sefiane, V. Koutsos, and M. E. R. Shanahan. Structural transitions in a ring stain created at the contact line of evaporating nanosuspension sessile drops. *Physical Review E*, 87:012301, 2013. doi: 10.1103/PhysRevE.87.012301.

[19] A. Askounis, K. Sefiane, V. Koutsos, and M. E. Shanahan. The effect of evaporation kinetics on nanoparticle structuring within contact line deposits of volatile drops. *Colloids and Surfaces A: Physicochemical and Engineering Aspects*, 441:855–866, 2014. doi: 10.1016/j.colsurfa.2012.10.017.

[20] D. Attinger, C. Moore, A. Donaldson, A. Jafari, and H. A. Stone. Fluid dynamics topics in bloodstain pattern analysis: Comparative review and research opportunities. *Forensic Science International*, 231(1):375–396, 2013. doi: 10.1016/j.forsciint.2013.04.018.

[21] A. M. Benselama, S. Harmand, and K. Sefiane. Thermocapillary effects on steadily evaporating contact line: A perturbative local analysis. *Physics of Fluids*, 24(7):072105, 2012. doi: 10.1063/1.4732151.

[22] R. Bhardwaj, X. Fang, and D. Attinger. Pattern formation during the evaporation of a colloidal nanoliter drop: a numerical and experimental study. *New Journal of Physics*, 11(7):075020, 2009. doi: 10.1088/1367-2630/11/7/075020.

[23] K. Birdi and D. Vu. Wettability and the evaporation rates of fluids from solid surfaces. *Journal of Adhesion Science and Technology*, 7(6):485–493, 1993. doi: 10.1163/156856193X00808.

[24] K. S. Birdi, D. T. Vu, and A. Winter. A study of the evaporation rates of small water drops placed on a solid surface. *The Journal of Physical Chemistry*, 93(9): 3702–3703, 1989. doi: 10.1021/j100346a065.

[25] E. Bormashenko, A. Musin, and M. Zinigrad. Evaporation of droplets on strongly and weakly pinning surfaces and dynamics of the triple line. *Colloids and Surfaces A: Physicochemical and Engineering Aspects*, 385(1):235–240, 2011. doi: 10.1016/j.colsurfa.2011.06.016.

[26] W. Bou Zeid and D. Brutin. Influence of relative humidity on spreading, pattern formation and adhesion of a drying drop of whole blood. *Colloids and Surfaces A: Physicochemical and Engineering Aspects*, 430:1–7, 2013. doi: 10.1016/j.colsurfa.2013.03.019.

[27] D. Brutin and V. Starov. Recent advances in droplet wetting and evaporation. *Chemical Society Reviews*, 47:558–585, 2018. doi: 10.1039/C6CS00902F.

[28] O. Carrier, N. Shahidzadeh-Bonn, R. Zargar, M. Aytouna, M. Habibi, J. Eggers, and D. Bonn. Evaporation of water: evaporation rate and collective effects. *Journal of Fluid Mechanics*, 798:774–786, 2016. doi: 10.1017/jfm.2016.356.

[29] G. Castanet, L. Perrin, O. Caballina, and F. Lemoine. Evaporation of closely-spaced interacting droplets arranged in a single row. *International Journal of Heat and Mass Transfer*, 93:788–802, 2016. doi: 10.1016/j.ijheatmasstransfer.2015.09.064.

[30] E. Cohen and L. Glicksman. Thermal properties of silica aerogel formula. *Journal of Heat Transfer*, 137(8), 2015. doi: 10.1115/1.4028901.

[31] R. W. Coutant and E. C. Penski. Experimental evaluation of mass transfer from sessile drops. *Industrial & Engineering Chemistry Fundamentals*, 21(3):250–254, 1982. doi: 10.1021/i100007a010.

[32] S. Dash and S. V. Garimella. Droplet evaporation dynamics on a superhydropho-

bic surface with negligible hysteresis. *Langmuir*, 29(34):10785–10795, 2013. doi: 10.1021/la402784c.

[33] S. Dash and S. V. Garimella. Droplet evaporation on heated hydrophobic and superhydrophobic surfaces. *Physical Review E*, 89:042402, 2014. doi: 10.1103/PhysRevE.89.042402.

[34] S. Dash, N. Kumari, and S. V. Garimella. Characterization of ultrahydrophobic hierarchical surfaces fabricated using a single-step fabrication methodology. *Journal of Micromechanics and Microengineering*, 21(10):105012, 2011. doi: 10.1088/0960-1317/21/10/105012.

[35] B.-J. de Gans and U. S. Schubert. Inkjet printing of well-defined polymer dots and arrays. *Langmuir*, 20(18):7789–7793, 2004. doi: 10.1021/la049469o.

[36] D. Debuisson, A. Merlen, V. Senez, and S. Arscott. Stick–jump (SJ) evaporation of strongly pinned nanoliter volume sessile water droplets on quick drying, micropatterned surfaces. *Langmuir*, 32(11):2679–2686, 2016. doi: 10.1021/acs.langmuir.6b00070.

[37] R. D. Deegan. Pattern formation in drying drops. *Physical Review E*, 61:475–485, 2000. doi: 10.1103/PhysRevE.61.475.

[38] R. D. Deegan, O. Bakajin, T. F. Dupont, G. Huber, S. R. Nagel, and T. A. Witten. Capillary flow as the cause of ring stains from dried liquid drops. *Nature*, 389:827–829, 1997. doi: 10.1038/39827.

[39] R. D. Deegan, O. Bakajin, T. F. Dupont, G. Huber, S. R. Nagel, and T. A. Witten. Contact line deposits in an evaporating drop. *Physical Review E*, 62:756–765, 2000. doi: 10.1103/PhysRevE.62.756.

[40] H. K. Dhavaleswarapu, C. P. Migliaccio, S. V. Garimella, and J. Y. Murthy. Experimental investigation of evaporation from low-contact-angle sessile droplets. *Langmuir*, 26(2):880–888, 2010. doi: 10.1021/la9023458.

[41] C. Diddens. Detailed finite element method modeling of evaporating multi-

component droplets. *Journal of Computational Physics*, 340:670–687, 2017. doi: 10.1016/j.jcp.2017.03.049.

[42] C. Diddens, J. G. M. Kuerten, C. W. M. van der Geld, and H. M. A. Wijshoff. Modeling the evaporation of sessile multi-component droplets. *Journal of Colloid and Interface Science*, 487:426–436, 2017. doi: 10.1016/j.jcis.2016.10.030.

[43] C. Diddens, H. Tan, P. Lv, M. Versluis, J. Kuerten, X. Zhang, and D. Lohse. Evaporating pure, binary and ternary droplets: thermal effects and axial symmetry breaking. *Journal of Fluid Mechanics*, 823:470–497, 2017. doi: 10.1017/jfm.2017.312.

[44] E. Dietrich, E. S. Kooij, X. Zhang, H. J. W. Zandvliet, and D. Lohse. Stick-jump mode in surface droplet dissolution. *Langmuir*, 31(16):4696–4703, 2015. doi: 10.1021/acs.langmuir.5b00653.

[45] E. Dietrich, S. Wildeman, C. W. Visser, K. Hofhuis, E. S. Kooij, H. J. W. Zandvliet, and D. Lohse. Role of natural convection in the dissolution of sessile droplets. *Journal of Fluid Mechanics*, 794:45–67, 2016. doi: 10.1017/jfm.2016.158.

[46] N. T. Dinh, E. Sowade, T. Blaudeck, S. Hermann, R. D. Rodriguez, D. R. Zahn, S. E. Schulz, R. R. Baumann, and O. Kanoun. High-resolution inkjet printing of conductive carbon nanotube twinlines utilizing evaporation-driven self-assembly. *Carbon*, 96:382–393, 2016. doi: 10.1016/j.carbon.2015.09.072.

[47] M. D. Doganci, B. U. Sesli, and H. Y. Erbil. Diffusion-controlled evaporation of sodium dodecyl sulfate solution drops placed on a hydrophobic substrate. *Journal of Colloid and Interface Science*, 362(2):524–531, 2011. doi: 10.1016/j.jcis.2011.06.060.

[48] B. Dollet and D. Lohse. Pinning stabilizes neighboring surface nanobubbles against Ostwald ripening. *Langmuir*, 32(43):11335–11339, 2016. doi: 10.1021/acs.langmuir.6b02136.

[49] D. G. Duffy. *Mixed Boundary Value Problems*. CRC Press, 2008.

[50] G. J. Dunn, S. K. Wilson, B. R. Duffy, S. David, and K. Sefiane. A mathematical model for the evaporation of a thin sessile liquid droplet: Comparison between experiment and theory. *Colloids and Surfaces A: Physicochemical and Engineering Aspects*, 323(1):50–55, 2008. doi: doi.org/10.1016/j.colsurfa.2007.09.031.

[51] G. J. Dunn, S. K. Wilson, B. R. Duffy, S. David, and K. Sefiane. The strong influence of substrate conductivity on droplet evaporation. *Journal of Fluid Mechanics*, 623:329351, 2009. doi: 10.1017/S0022112008005004.

[52] G. J. Dunn, S. K. Wilson, B. R. Duffy, and K. Sefiane. Evaporation of a thin droplet on a thin substrate with a high thermal resistance. *Physics of Fluids*, 21 (5):052101, 2009. doi: 10.1063/1.3121214.

[53] A. H. England. Mixed boundary-value problems in potential theory. *Proceedings of the Edinburgh Mathematical Society*, 22(2):91–98, 1979. doi: 10.1017/S0013091500016205.

[54] H. Y. Erbil, G. McHale, S. M. Rowan, and M. I. Newton. Determination of the receding contact angle of sessile drops on polymer surfaces by evaporation. *Langmuir*, 15(21):7378–7385, 1999. doi: 10.1021/la9900831.

[55] H. Y. Erbil, G. McHale, and M. I. Newton. Drop evaporation on solid surfaces: constant contact angle mode. *Langmuir*, 18(7):2636–2641, 2002. doi: 10.1021/la011470p.

[56] V. I. Fabrikant. On the potential flow through membranes. *Zeitschrift für angewandte Mathematik und Physik ZAMP*, 36(4):616–623, 1985. doi: 10.1007/BF00945301.

[57] X. Fang, B. Li, E. Petersen, Y. Ji, J. C. Sokolov, and M. H. Rafailovich. Factors controlling the drop evaporation constant. *The Journal of Physical Chemistry B*, 109(43):20554–20557, 2005. doi: 10.1021/jp053986d.

[58] J. Fukai, H. Ishizuka, Y. Sakai, M. Kaneda, M. Morita, and A. Takahara. Effects

of droplet size and solute concentration on drying process of polymer solution droplets deposited on homogeneous surfaces. *International Journal of Heat and Mass Transfer*, 49(19):3561–3567, 2006. doi: 10.1016/j.ijheatmasstransfer.2006.02.049.

[59] F. Giorgiutti-Dauphiné and L. Pauchard. Drying drops. *The European Physical Journal E*, 41(3):32, 2018. doi: 10.1140/epje/i2018-11639-2.

[60] G. M. L. Gladwell and V. I. Fabrikant. The interaction between a system of circular punches on an elastic half space. *Journal of Applied Mechanics*, 49(2):341–344, 1982. doi: 10.1115/1.3162091.

[61] J. A. Greenwood. Constriction resistance and the real area of contact. *British Journal of Applied Physics*, 17(12):1621–1632, 1966. doi: 10.1088/0508-3443/17/12/310.

[62] W. M. Grissom and F. Wierum. Liquid spray cooling of a heated surface. *International Journal of Heat and Mass Transfer*, 24(2):261–271, 1981. doi: 10.1016/0017-9310(81)90034-X.

[63] A. Hakonen, F. Wang, P. O. Andersson, H. Wingfors, T. Rindzevicius, M. S. Schmidt, V. R. Soma, S. Xu, Y. Li, A. Boisen, and H. Wu. Hand-held femtogram detection of hazardous picric acid with hydrophobic Ag nanopillar SERS substrates and mechanism of elasto-capillarity. *ACS Sensors*, 2(2):198–202, 2017. doi: 10.1021/acssensors.6b00749.

[64] S. Hatte, K. Pandey, K. Pandey, S. Chakraborty, and S. Basu. Universal evaporation dynamics of ordered arrays of sessile droplets. *Journal of Fluid Mechanics*, 866:61–81, 2019. doi: 10.1017/jfm.2019.105.

[65] H. Hu and R. G. Larson. Evaporation of a sessile droplet on a substrate. *The Journal of Physical Chemistry B*, 106:1334–1344, 2002. doi: 10.1021/jp0118322.

[66] H. Hu and R. G. Larson. Analysis of the effects of Marangoni stresses on the

microflow in an evaporating sessile droplet. *Langmuir*, 21(9):3972–3980, 2005. doi: 10.1021/la0475270.

[67] S. Hu, Y. Wang, X. Man, and M. Doi. Deposition patterns of two neighboring droplets: Onsager variational principle studies. *Langmuir*, 33(23):5965–5972, 2017. doi: 10.1021/acs.langmuir.7b01354.

[68] J. D. Jackson. *Classical Electrodynamics*. Wiley, 1999.

[69] T. Kajiya, C. Monteux, T. Narita, F. Lequeux, and M. Doi. Contact-line recession leaving a macroscopic polymer film in the drying droplets of waterpoly(n,n-dimethylacrylamide) (PDMA) solution. *Langmuir*, 25(12):6934–6939, 2009. doi: 10.1021/la900216k.

[70] S. Kulinich and M. Farzaneh. Effect of contact angle hysteresis on water droplet evaporation from super-hydrophobic surfaces. *Applied Surface Science*, 255(7): 4056–4060, 2009. doi: 10.1016/j.apsusc.2008.10.109.

[71] H. Kusumaatmaja and J. M. Yeomans. Modeling contact angle hysteresis on chemically patterned and superhydrophobic surfaces. *Langmuir*, 23(11):6019–6032, 2007. doi: 10.1021/la063218t.

[72] G. Laghezza, E. Dietrich, J. M. Yeomans, R. Ledesma-Aguilar, E. S. Kooij, H. J. W. Zandvliet, and D. Lohse. Collective and convective effects compete in patterns of dissolving surface droplets. *Soft Matter*, 12:5787–5796, 2016. doi: 10.1039/C6SM00767H.

[73] O. Laporte and R. G. Fowler. Resistance of a plasma slab between juxtaposed disk electrodes. *Physical Review*, 148:170–175, 1966. doi: 10.1103/PhysRev.148.170.

[74] R. G. Larson. Transport and deposition patterns in drying sessile droplets. *AIChE Journal*, 60(5):1538–1571, 2014. doi: 10.1002/aic.14338.

[75] N. N. Lebedev. *Special Functions and Their Applications*. Dover, New York, 1972.

[76] C. Y. Lee, B. J. Zhang, J. Park, and K. J. Kim. Water droplet evapora-

tion on cu-based hydrophobic surfaces with nano- and micro-structures. *International Journal of Heat and Mass Transfer*, 55(7):2151–2159, 2012. doi: 10.1016/j.ijheatmasstransfer.2011.12.019.

[77] G. Li, S. M. Flores, C. Vavilala, M. Schmittel, and K. Graf. Evaporation dynamics of microdroplets on self-assembled monolayers of dialkyl disulfides. *Langmuir*, 25 (23):13438–13447, 2009. doi: 10.1021/la901422v.

[78] H. Li, N. Fowler, C. Struck, and S. Sivasankar. Flow triggered by instabilities at the contact line of a drop containing nanoparticles. *Soft Matter*, 7:5116–5119, 2011. doi: 10.1039/C1SM05097D.

[79] Y. Li, P. Lv, C. Diddens, H. Tan, H. Wijshoff, M. Versluis, and D. Lohse. Evaporation-triggered segregation of sessile binary droplets. *Physical Review Letters*, 120:224501, 2018. doi: 10.1103/PhysRevLett.120.224501.

[80] T. Lim, J. Yang, S. Lee, J. Chung, and D. Hong. Deposit pattern of inkjet printed pico-liter droplet. *International Journal of Precision Engineering and Manufacturing*, 13(6):827–833, 2012. doi: 10.1007/s12541-012-0108-1.

[81] D. Lohse and X. Zhang. Surface nanobubbles and nanodroplets. *Reviews of Modern Physics*, 87:981–1035, 2015. doi: 10.1103/RevModPhys.87.981.

[82] D. Lohse and X. Zhang. Pinning and gas oversaturation imply stable single surface nanobubbles. *Physical Review E*, 91:031003, 2015. doi: 10.1103/PhysRevE.91.031003.

[83] M. C. Lopes, E. Bonaccurso, T. Gambaryan-Roisman, and P. Stephan. Influence of the substrate thermal properties on sessile droplet evaporation: Effect of transient heat transport. *Colloids and Surfaces A: Physicochemical and Engineering Aspects*, 432:64 – 70, 2013. doi: 10.1016/j.colsurfa.2013.04.017.

[84] S. Maheshwari, L. Zhang, Y. Zhu, and H.-C. Chang. Coupling between precipitation and contact-line dynamics: Multiring stains and stick-slip motion. *Physical Review Letters*, 100:044503, 2008. doi: 10.1103/PhysRevLett.100.044503.

[85] J. H. Mathews and R. W. Howell. *Complex Analysis for Mathematics and Engineering*. Jones & Bartlett Publishers, 2012.

[86] J. C. Maxwell. Diffusion. In *The Scientific Papers of James Clerk Maxwell*, volume 2. Cambridge University Press, 1890. Reprinted Dover, New York, 1952, pages 625–646.

[87] G. McHale, S. M. Rowan, M. I. Newton, and M. K. Banerjee. Evaporation and the wetting of a low-energy solid surface. *The Journal of Physical Chemistry B*, 102(11):1964–1967, 1998. doi: 10.1021/jp972552i.

[88] G. McHale, S. Aqil, N. J. Shirtcliffe, M. I. Newton, and H. Y. Erbil. Analysis of droplet evaporation on a superhydrophobic surface. *Langmuir*, 21(24):11053–11060, 2005. doi: 10.1021/la0518795.

[89] R. Mehta and T. Bose. Temperature distribution in a large circular plate heated by a disk heat source. *International Journal of Heat and Mass Transfer*, 26(7): 1093–1095, 1983. doi: 10.1016/S0017-9310(83)80136-7.

[90] S. Michelin, E. Guérin, and E. Lauga. Collective dissolution of microbubbles. *Physical Review Fluids*, 3:043601, 2018. doi: 10.1103/PhysRevFluids.3.043601.

[91] J. R. Moffat, K. Sefiane, and M. E. R. Shanahan. Effect of TiO2 nanoparticles on contact line stickslip behavior of volatile drops. *The Journal of Physical Chemistry B*, 113(26):8860–8866, 2009. doi: 10.1021/jp902062z.

[92] T. A. Nguyen, A. V. Nguyen, M. A. Hampton, Z. P. Xu, L. Huang, and V. Rudolph. Theoretical and experimental analysis of droplet evaporation on solid surfaces. *Chemical Engineering Science*, 69(1):522–529, 2012. doi: 10.1016/j.ces.2011.11.009.

[93] T. A. H. Nguyen and A. V. Nguyen. Increased evaporation kinetics of sessile droplets by using nanoparticles. *Langmuir*, 28(49):16725–16728, 2012. doi: 10.1021/la303293w.

[94] T. A. H. Nguyen and A. V. Nguyen. Reply to Comment on increased evaporation

kinetics of sessile droplets by using nanoparticles. *Langmuir*, 29(39):12330–12330, 2013. doi: 10.1021/la403151k.

[95] T. A. H. Nguyen, S. R. Biggs, and A. V. Nguyen. Analytical model for diffusive evaporation of sessile droplets coupled with interfacial cooling effect. *Langmuir*, 34(23):6955–6962, 2018. doi: 10.1021/acs.langmuir.7b03862.

[96] D. Orejon, K. Sefiane, and M. E. R. Shanahan. Stick–slip of evaporating droplets: Substrate hydrophobicity and nanoparticle concentration. *Langmuir*, 27(21): 12834–12843, 2011. doi: 10.1021/la2026736.

[97] F. Parisse and C. Allain. Drying of colloidal suspension droplets: experimental study and profile renormalization. *Langmuir*, 13(14):3598–3602, 1997. doi: 10.1021/la951521g.

[98] M. Parsa, S. Harmand, K. Sefiane, M. Bigerelle, and R. Deltombe. Effect of substrate temperature on pattern formation of nanoparticles from volatile drops. *Langmuir*, 31(11):3354–3367, 2015. doi: 10.1021/acs.langmuir.5b00362.

[99] A. J. Petsi and V. N. Burganos. Evaporation-induced flow in an inviscid liquid line at any contact angle. *Physical Review E*, 73:041201, 2006. doi: 10.1103/PhysRevE.73.041201.

[100] T. Pham and S. Kumar. Drying of droplets of colloidal suspensions on rough substrates. *Langmuir*, 33(38):10061–10076, 2017. doi: 10.1021/acs.langmuir.7b02341.

[101] T. Pham and S. Kumar. Imbibition and evaporation of droplets of colloidal suspensions on permeable substrates. *Physical Review Fluids*, 4:034004, 2019. doi: 10.1103/PhysRevFluids.4.034004.

[102] R. Picknett and R. Bexon. The evaporation of sessile or pendant drops in still air. *Journal of Colloid and Interface Science*, 61(2):336–350, 1977. doi: 10.1016/0021-9797(77)90396-4.

[103] P. G. Pittoni, C.-C. Chang, T.-S. Yu, and S.-Y. Lin. Evaporation of water drops

on polymer surfaces: Pinning, depinning and dynamics of the triple line. *Colloids and Surfaces A: Physicochemical and Engineering Aspects*, 432:89–98, 2013. doi: 10.1016/j.colsurfa.2013.04.045.

[104] P. G. Pittoni, C.-H. Lin, T.-S. Yu, and S.-Y. Lin. On the uniqueness of the receding contact angle: Effects of substrate roughness and humidity on evaporation of water drops. *Langmuir*, 30(31):9346–9354, 2014. doi: 10.1021/la501455d.

[105] Y. O. Popov. Evaporative deposition patterns: Spatial dimensions of the deposit. *Physical Review E*, 71:036313, 2005. doi: 10.1103/PhysRevE.71.036313.

[106] Y. O. Popov and T. A. Witten. Characteristic angles in the wetting of an angular region: Deposit growth. *Physical Review E*, 68:036306, 2003. doi: 10.1103/PhysRevE.68.036306.

[107] C. Poulard, O. Bnichou, and A. M. Cazabat. Freely receding evaporating droplets. *Langmuir*, 19(21):8828–8834, 2003. doi: 10.1021/la030162j.

[108] C. Pozrikidis. *Fluid Dynamics: Theory, Computation, and Numerical Simulation : Accompanied by the Software Library FDLIB*. Kluwer Academic Publishers, 2001.

[109] M. D. Protheroe, A. Al-Jumaily, and R. J. Nates. Prediction of droplet evaporation characteristics of nebuliser based humidification and drug delivery devices. *International Journal of Heat and Mass Transfer*, 60:772–780, 2013. doi: 10.1016/j.ijheatmasstransfer.2013.01.053.

[110] S. A. Putnam, A. M. Briones, L. W. Byrd, J. S. Ervin, M. S. Hanchak, A. White, and J. G. Jones. Microdroplet evaporation on superheated surfaces. *International Journal of Heat and Mass Transfer*, 55(21):5793–5807, 2012. doi: 10.1016/j.ijheatmasstransfer.2012.05.076.

[111] J. Qian, G. F. Arends, and X. Zhang. Surface nanodroplets: Formation, dissolution, and applications. *Langmuir*, 35(39):12583–12596, 2019. doi: 10.1021/acs.langmuir.9b01051.

[112] W. D. Ristenpart, P. G. Kim, C. Domingues, J. Wan, and H. A. Stone. Influence of substrate conductivity on circulation reversal in evaporating drops. *Physical Review Letters*, 99:234502, 2007. doi: 10.1103/PhysRevLett.99.234502.

[113] A. F. Routh. Drying of thin colloidal films. *Reports on Progress in Physics*, 76 (4):046603, 2013.

[114] S. S. Sazhin. Advanced models of fuel droplet heating and evaporation. *Progress in Energy and Combustion Science*, 32(2):162–214, 2006. doi: 10.1016/j.pecs.2005.11.001.

[115] C. Schäfle, C. Bechinger, B. Rinn, C. David, and P. Leiderer. Cooperative evaporation in ordered arrays of volatile droplets. *Physical Review Letters*, 83:5302–5305, 1999. doi: 10.1103/PhysRevLett.83.5302.

[116] F. G. H. Schofield, S. K. Wilson, D. Pritchard, and K. Sefiane. The strong influence of thermal effects on the lifetime of an evaporating droplet, extended abstract in the Proceedings of the 16th UK Heat Transfer Conference, 8th–9th September 2019, Nottingham.

[117] F. G. H. Schofield, S. K. Wilson, D. Pritchard, and K. Sefiane. The lifetimes of evaporating sessile droplets are significantly extended by strong thermal effects. *Journal of Fluid Mechanics*, 851:231244, 2018. doi: 10.1017/jfm.2018.496.

[118] F. G. H. Schofield, A. W. Wray, D. Pritchard, and S. K. Wilson. The shielding effect extends the lifetimes of two-dimensional sessile droplets. *Journal of Engineering Mathematics*, 120:89–110, 2020. doi: 10.1007/s10665-019-10033-7.

[119] R. W. Schrage. *A Theoretical Study of Interphase Mass Transfer*. Columbia University Press, 1953.

[120] K. Sefiane and R. Bennacer. An expression for droplet evaporation incorporating thermal effects. *Journal of Fluid Mechanics*, 667:260271, 2011. doi: 10.1017/S0022112010005446.

[121] K. Sefiane, S. K. Wilson, S. David, G. J. Dunn, and B. R. Duffy. On the effect of

the atmosphere on the evaporation of sessile droplets of water. *Physics of Fluids*, 21(6):062101, 2009. doi: 10.1063/1.3131062.

[122] S. Semenov, V. M. Starov, R. G. Rubio, H. Agogo, and M. G. Velarde. Evaporation of sessile water droplets: Universal behaviour in presence of contact angle hysteresis. *Colloids and Surfaces A: Physicochemical and Engineering Aspects*, 391(1):135–144, 2011. doi: 10.1016/j.colsurfa.2011.07.013.

[123] S. Semenov, V. M. Starov, M. G. Velarde, and R. G. Rubio. Droplets evaporation: Problems and solutions. *The European Physical Journal Special Topics*, 197(1): 265, 2011. doi: 10.1140/epjst/e2011-01468-1.

[124] S. Semenov, A. Trybala, H. Agogo, N. Kovalchuk, F. Ortega, R. G. Rubio, V. M. Starov, and M. G. Velarde. Evaporation of droplets of surfactant solutions. *Langmuir*, 29(32):10028–10036, 2013. doi: 10.1021/la401578v.

[125] S. Semenov, A. Trybala, R. G. Rubio, N. Kovalchuk, V. Starov, and M. G. Velarde. Simultaneous spreading and evaporation: Recent developments. *Advances in Colloid and Interface Science*, 206:382–398, 2014. doi: 10.1016/j.cis.2013.08.006.

[126] A. Shaikeea, S. Basu, S. Hatte, and L. Bansal. Insights into vapor-mediated interactions in a nanocolloidal droplet system: Evaporation dynamics and affects on self-assembly topologies on macro- to microscales. *Langmuir*, 32(40):10334–10343, 2016. doi: 10.1021/acs.langmuir.6b03024.

[127] A. J. D. Shaikeea and S. Basu. Evaporating sessile droplet pair: Insights into contact line motion, flow transitions and emergence of universal vaporisation pattern. *Applied Physics Letters*, 108(24):244102, 2016. doi: 10.1063/1.4953836.

[128] A. J. D. Shaikeea and S. Basu. Insight into the evaporation dynamics of a pair of sessile droplets on a hydrophobic substrate. *Langmuir*, 32(5):1309–1318, 2016. doi: 10.1021/acs.langmuir.5b04570.

[129] M. E. R. Shanahan, K. Sefiane, and J. R. Moffat. Dependence of volatile droplet

lifetime on the hydrophobicity of the substrate. *Langmuir*, 27(8):4572–4577, 2011. doi: 10.1021/la200437s.

[130] D. H. Shin, S. H. Lee, J.-Y. Jung, and J. Y. Yoo. Evaporating characteristics of sessile droplet on hydrophobic and hydrophilic surfaces. *Microelectronic Engineering*, 86(4):1350–1353, 2009. doi: 10.1016/j.mee.2009.01.026.

[131] D. H. Shin, S. H. Lee, C. K. Choi, and S. Retterer. The evaporation and wetting dynamics of sessile water droplets on submicron-scale patterned silicon hydrophobic surfaces. *Journal of Micromechanics and Microengineering*, 20(5):055021, 2010. doi: 10.1088/0960-1317/20/5/055021.

[132] L. Shmuylovich, A. Q. Shen, and H. A. Stone. Surface morphology of drying latex films: multiple ring formation. *Langmuir*, 18(9):3441–3445, 2002. doi: 10.1021/la011484v.

[133] S. K. Singh, M. Gogna, K. Muralidhar, and S. Khandekar. Combined effect of substrate wettability and thermal properties on evaporation dynamics of a sessile droplet. *Interfacial Phenomena and Heat Transfer*, 5(4):321–335, 2017.

[134] I. N. Sneddon. *Mixed Boundary Value Problems in Potential Theory*. North-Holland Publishing Company, 1966.

[135] B. Sobac and D. Brutin. Triple-line behavior and wettability controlled by nanocoated substrates: Influence on sessile drop evaporation. *Langmuir*, 27(24):14999–15007, 2011. doi: 10.1021/la203681j.

[136] B. Sobac and D. Brutin. Thermocapillary instabilities in an evaporating drop deposited onto a heated substrate. *Physics of Fluids*, 24(3):032103, 2012. doi: 10.1063/1.3692267.

[137] C. Sodtke, V. S. Ajaev, and P. Stephan. Evaporation of thin liquid droplets on heated surfaces. *Heat Mass Transfer*, 43:649–657, 2007. doi: 10.1007/s00231-006-0126-6.

[138] C. Sodtke, V. S. Ajaev, and P. Stephan. Dynamics of volatile liquid droplets

on heated surfaces: theory versus experiment. *Journal of Fluid Mechanics*, 610: 343–362, 2008. doi: 10.1017/S0022112008002759.

[139] M. Sokuler, G. K. Auernhammer, C. J. Liu, E. Bonaccurso, and H.-J. Butt. Dynamics of condensation and evaporation: Effect of inter-drop spacing. *Europhysics Letters*, 89(3):36004, 2010. doi: 10.1209/0295-5075/89/36004.

[140] H. Song, Y. Lee, S. Jin, H.-Y. Kim, and J. Y. Yoo. Prediction of sessile drop evaporation considering surface wettability. *Microelectronic Engineering*, 88(11): 3249–3255, 2011. doi: 10.1016/j.mee.2011.07.015.

[141] D. M. Soolaman and H.-Z. Yu. Water microdroplets on molecularly tailored surfaces: correlation between wetting hysteresis and evaporation mode switching. *The Journal of Physical Chemistry B*, 109(38):17967–17973, 2005. doi: 10.1021/jp051182s.

[142] J. M. Stauber. *On the Evaporation of Sessile Droplets*. PhD thesis, University of Strathclyde, 2015.

[143] J. M. Stauber, S. K. Wilson, B. R. Duffy, and K. Sefiane. On the lifetimes of evaporating droplets. *Journal of Fluid Mechanics*, 744:R2, 2014. doi: 10.1017/jfm.2014.94.

[144] J. M. Stauber, S. K. Wilson, B. R. Duffy, and K. Sefiane. Evaporation of droplets on strongly hydrophobic substrates. *Langmuir*, 31(12):3653–3660, 2015. doi: 10.1021/acs.langmuir.5b00286.

[145] J. M. Stauber, S. K. Wilson, B. R. Duffy, and K. Sefiane. On the lifetimes of evaporating droplets with related initial and receding contact angles. *Physics of Fluids*, 27(12):122101, 2015. doi: 10.1063/1.4935232.

[146] J. J. Stoker. Surface waves in water of variable depth. *Quarterly of Applied Mathematics*, 5(1):1–54, 1947.

[147] E. Sultan, A. Boudaoud, and M. Ben Amar. Evaporation of a thin film: Diffusion

of the vapour and Marangoni instabilities. *Journal of Fluid Mechanics*, 543:183–202, 2005. doi: 10.1017/S0022112005006348.

[148] P. J. Senz, A. W. Wray, Z. Che, O. K. Matar, P. Valluri, J. Kim, and K. Sefiane. Dynamics and universal scaling law in geometrically-controlled sessile drop evaporation. *Nature Communications*, 8:14783, 2018. doi: 10.1038/ncomms14783.

[149] E. L. Talbot, A. Berson, P. S. Brown, and C. D. Bain. Evaporation of picoliter droplets on surfaces with a range of wettabilities and thermal conductivities. *Physical Review E*, 85:061604, 2012. doi: 10.1103/PhysRevE.85.061604.

[150] H. Tan, C. Diddens, P. Lv, J. G. M. Kuerten, X. Zhang, and D. Lohse. Evaporation-triggered microdroplet nucleation and the four life phases of an evaporating ouzo drop. *Proceedings of the National Academy of Sciences*, 113 (31):8642–8647, 2016. doi: 10.1073/pnas.1602260113.

[151] H. Tan, C. Diddens, M. Versluis, H.-J. Butt, D. Lohse, and X. Zhang. Self-wrapping of an ouzo drop induced by evaporation on a superamphiphobic surface. *Soft Matter*, 13:2749–2759, 2017. doi: 10.1039/C6SM02860H.

[152] A. Trybala, A. Okoye, S. Semenov, H. Agogo, R. G. Rubio, F. Ortega, and V. M. Starov. Evaporation kinetics of sessile droplets of aqueous suspensions of inorganic nanoparticles. *Journal of Colloid and Interface Science*, 403:49–57, 2013. doi: 10.1016/j.jcis.2013.04.017.

[153] P. T. Tsilingiris. Thermophysical and transport properties of humid air at temperature range between 0 and 100°C. *Energy Conversion and Management*, 49 (5):1098–1110, 2008. doi: 10.1016/j.enconman.2007.09.015.

[154] K. Uno, K. Hayashi, T. Hayashi, K. Ito, and H. Kitano. Particle adsorption in evaporating droplets of polymer latex dispersions on hydrophilic and hydrophobic surfaces. *Colloid and Polymer Science*, 276(9):810–815, 1998. doi: 10.1007/s003960050314.

[155] Z. Wang, D. Orejon, K. Sefiane, and Y. Takata. Coupled thermal transport and

mass diffusion during vapor absorption into hygroscopic liquid desiccant droplets. *International Journal of Heat and Mass Transfer*, 134:1014–1023, 2019. doi: 10.1016/j.ijheatmasstransfer.2019.01.084.

[156] H. Weber. Ueber die Besselschen Functionen und ihre Anwendung auf die Theorie der elektrischen Ströme. *Journal für die reine und agewandte Mathematik*, pages 75–105, 1873. doi: 10.1515/crll.1873.75.75.

[157] G. Wei, Y. Liu, X. Du, and X. Zhang. Gaseous conductivity study on silica aerogel and its composite insulation materials. *Journal of Heat Transfer*, 134(4): 041301–041301–5, 2012. doi: 10.1115/1.4004170.

[158] J. R. Whiteman. Treatment of singularities in a harmonic mixed boundary value problem by dual series methods. *The Quarterly Journal of Mechanics and Applied Mathematics*, 21(1):41–50, 1968. doi: 10.1093/qjmam/21.1.41.

[159] S. K. Wilson, F. G. H. Schofield, D. Pritchard, and K. Sefiane. Anomalously long lifetimes of evaporating sessile droplets, extended abstract in the Proceedings of the 15th UK Heat Transfer Conference, 4th–5th September 2017, London.

[160] A. W. Wray, D. T. Papageorgiou, R. V. Craster, K. Sefiane, and O. K. Matar. Electrostatic suppression of the coffee stain effect. *Langmuir*, 30(20):5849–5858, 2014. doi: 10.1021/la500805d.

[161] A. W. Wray, B. R. Duffy, and S. K. Wilson. Competitive evaporation of multiple sessile droplets. *Journal of Fluid Mechanics*, 884:A45, 2020. doi: 10.1017/jfm.2019.919.

[162] Q. Xie and J. Harting. From dot to ring: The role of friction in the deposition pattern of a drying colloidal suspension droplet. *Langmuir*, 34(18):5303–5311, 2018. doi: 10.1021/acs.langmuir.8b00727.

[163] F. Yang and J. C. M. Li. Impression creep of a thin film by vacancy diffusion. I. Straight punch. *Journal of Applied Physics*, 74(7):4382–4389, 1993. doi: 10.1063/1.354406.

[164] F. Yang and J. C. M. Li. Impression creep of a thin film by vacancy diffusion. II. Cylindrical punch. *Journal of Applied Physics*, 74(7):4390–4397, 1993. doi: 10.1063/1.354407.

[165] F. Yang and R. Yao. The solution for mixed boundary value problems of two-dimensional potential theory. *Indian Journal of Pure and Applied Mathematics*, 27(3):313–322, 1996.

[166] A. L. Yarin, J. Szczech, C. M. Megaridis, J. Zhang, and D. R. Gamota. Lines of dense nanoparticle colloidal suspensions evaporating on a flat surface: Formation of non-uniform dried deposits. *Journal of Colloid and Interface Science*, 294: 343–354, 2006.

[167] T. Young. III. An essay on the cohesion of fluids. *Philosophical Transactions of the Royal Society of London*, 95:65–87, 1805. doi: 10.1098/rstl.1805.0005.

[168] H. Zhang, Y. Kita, D. Zhang, G. Nagayama, Y. Takata, K. Sefiane, and A. Askounis. Drop evaporation on rough hot-spots: Effect of wetting modes. *Heat Transfer Engineering*, 2019. doi: 10.1080/01457632.2019.1640458.

[169] J. Zhang, F. Müller-Plathe, and F. Leroy. Pinning of the contact line during evaporation on heterogeneous surfaces: Slowdown or temporary immobilization? Insights from a nanoscale study. *Langmuir*, 31(27):7544–7552, 2015. doi: 10.1021/acs.langmuir.5b01097.

[170] X. Zhang, H. Lhuissier, C. Sun, and D. Lohse. Surface nanobubbles nucleate microdroplets. *Physical Review Letters*, 112:144503, 2014. doi: 10.1103/PhysRevLett.112.144503.

[171] X. Zhang, J. Wang, L. Bao, E. Dietrich, R. C. A. van der Veen, S. Peng, J. Friend, H. J. W. Zandvliet, L. Yeo, and D. Lohse. Mixed mode of dissolving immersed nanodroplets at a solid–water interface. *Soft Matter*, 11:1889–1900, 2015. doi: 10.1039/C4SM02397H.